PERFORMANCE AND METHODOLOGICAL ASPECTS IN POSITRON EMISSION TOMOGRAPHY

by

Mika Teräs

From Turku PET Centre and Department of Clinical Physiology and Nuclear Medicine, University of Turku, Finland

Supervised by

Professor Juhani Knuuti, MD, PhD

Turku PET Centre and Department of Clinical Physiology and Nuclear Medicine

University of Turku

and

Chief Physicist Jarmo Kulmala, PhD

Department of Oncology

Turku University Central Hospital

Reviewed by

Professor Jyrki Kuikka

Department of Clinical Physiology and Nuclear Medicine

University of Kuopio

and

Docent Mikko Tenhunen

Department of Oncology

University Central Hospital of Helsinki

Dissertation opponent

Docent Matti Koskinen

Department of Hospital Physics

University Central Hospital of Tampere

To Anne, Petteri and Sofianna

ABSTRACT

Mika Teräs

PERFORMANCE AND METHODOLOGICAL ASPECTS IN POSITRON EMISSION TOMOGRAPHY

Keywords: Positron emission tomography, NEMA, Brain imaging, Partial volume effect, Cardiac imaging, Gating, Motion PET

Turku PET Centre and Department of Clinical Physiology and Nuclear Medicine, University of Turku

Performance standards for Positron emission tomography (PET) were developed to be able to compare systems from different generations and manufacturers. This resulted in the NEMA methodology in North America and the IEC in Europe. In practices, the NEMA NU 2- 2001 is the method of choice today. These standardized methods allow assessment of the physical performance of new commercial dedicated PET/CT tomographs.

The point spread in image formation is one of the factors that blur the image. The phenomenon is often called the partial volume effect. Several methods for correcting for partial volume are under research but no real agreement exists on how to solve it. The influence of the effect varies in different clinical settings and it is likely that new methods are needed to solve this problem.

Most of the clinical PET work is done in the field of oncology. The whole body PET combined with a CT is the standard investigation today in oncology. Despite the progress in PET imaging technique visualization, especially quantification of small lesions is a challenge. In addition to partial volume, the movement of the object is a significant source of error. The main causes of movement are respiratory and cardiac motions. Most of the new commercial scanners are in addition to cardiac gating, also capable of respiratory gating and this technique has been used in patients with cancer of the thoracic region and patients being studied for the planning of radiation therapy.

For routine cardiac applications such as assessment of viability and perfusion only cardiac gating has been used. However, the new targets such as plaque or molecular imaging of new therapies require better control of the cardiac motion also caused by respiratory motion. To overcome these problems in cardiac work, a dual gating approach has been proposed. In this study we investigated the physical performance of a new whole body PET/CT scanner with NEMA standard, compared methods for partial volume correction in PET studies of the brain and developed and tested a new robust method for dual cardiac-respiratory gated PET with phantom, animal and human data.

Results from performance measurements showed the feasibility of the new scanner design in 2D and 3D whole body studies. Partial volume was corrected, but there is no best method among those tested as the correction also depends on the radiotracer and its distribution. New methods need to be developed for proper correction. The dual gating algorithm generated is shown to handle dual-gated data, preserving quantification and clearly eliminating the majority of contraction and respiration movement.

TIIVISTELMÄ

Mika Teräs

SUORITUSKYVYN JA KUVAUSMENETELMIEN KEHITYS POSITRONIEMISSIOTOMOGRAFIASSA

Avainsanat: Positroniemissiotomografia, NEMA, Aivokuvantaminen, Osittaistilavuusefekti, Sydänkuvantaminen, Tahdistus, LiikePET

Valtakunnallinen PET keskus ja Kliininen fysiologia ja Isotooppilääketiede, Turun yliopisto

Annales Universitatis Turkuensis, 2008

Jotta eri laitevalmistajien sukupolvien positroniemissiotomografialaitteita voidaan verrata toisiinsa, tarvitaan suorituskykymittauksia. Pohjois-Amerikassa on kehitetty standardoituja NEMA mittauksia ja Euroopassa vastaavia IEC-mittauksia. NEMA NU 2-2001 standardi on yleisimmin käytössä oleva standardi.

Kuvan muodostuksessa tapahtuvan pisteen levenemisen aiheuttama osittaistilavuusilmiö on yksi kuvaa sumentava tekijä ja ilmiön korjaamista on tutkittu paljon. Kuitenkin korjausmenetelmien soveltuvuus on yhä epäselvää ja on ilmeistä, että tarvitaan vielä uusia menetelmiä ilmiön korjaamiseksi.

Kliiniset PET-tutkimukset liittyvät lähes aina syöpätauteihin. Kokokehon PET yhdistettynä TT-kuvaukseen on tämän päivän yleisin tutkimus. PET menetelmän kehityksestä huolimatta visualisointi ja etenkin pienten kohteiden kvantitointi ovat yhä haasteellisia. Osittaistilavuusilmiön lisäksi kuvauskohteen liike on suuri virhelähde. Pääasiassa liikkeen aiheuttavat hengitys ja sydämen syke. Useimmat laitteet kykenevät hengitystahdistukseen ja sitä on käytetty keuhkojen alueen kuvauksiin sädehoidon suunnittelun yhteydessä. Tiettyihin sydäntutkimuksiin kuten sydänlihaksen elinkyvyn ja perfuusion mittaamiseen on käytetty sydäntahdistusta, mutta pyrittäessä kuvantamaan valtimokovettumia tai hauraita plakkeja tarvitaan sydämen sykkeen ja hengitysliikkeen yhtäaikaista korjausta. Tähän eivät nykyiset laitteet kykene.

Tämä tutkimus määrittää uuden sukupolven PET/TT-laitteen fysikaaliset suoritusarvot NEMA-menetelmää käyttäen, vertaa nykyisiä osittaistilavuusilmiön korjausmenetelmiä aivotutkimuksissa ja testaa Turussa kehitettyä kaksoistahdistusmenetelmää ensimmäisillä eläin- ja humaanimittauksilla.

Suorituskykymittaukset osoittivat uuden sukupolven laitteen soveltuvan entistä paremmin kokokehon 2D ja 3D tutkimuksiin.

Osittaistilavuusilmiön korjausmenetelmiin ei saatu yksikäsitteistä vastausta ja onkin ilmeistä, että tutkimus niiden parissa jatkuu edelleen. Paras korjausmenetelmä riippui merkkiaineen jakautumisesta ja tutkimusasetelmasta.

Kehittämämme kaksoistahdistusmenetelmä osoitti toimivuutensa testikohde-, eläin- ja humaanimittauksissa säilyttäen kvantitaation ja poistaen suurimman osan hengityksen ja sydämen sykkeen aiheuttamasta liikkeestä.

TABLE OF CONTENTS

ABBREVIATIONS

2D	Two dimensional
3D	Three dimensional
AC	Attenuation correction
BGO	Bismuth germinate oxide
BP	Binding potential
CAD	Coronary artery disease
CCD camera	charge-couple device camera
CPS	Counts per second
CRC	Cold sphere contrast
CSF	Cerebrospinal fluid
CT	X-ray computerized tomography
CTA	CT angiography
CTAC	CT based attenuation correction
CV	Coefficient of variation
DT	Dead time
ECG	Electrocardiogram
ED	End diastole
ES	End systole
EW	Equivalent width
FBP	Filtered back projection reconstruction method
FOV	Field of view
FWHM	Full width at half maximum
FWTM	Full width at tenth maximum
GE	General Electric Inc
GM	Grey matter
HCR	Hot sphere contrast
HU	Hounsfield Unit
HRRT	High resolution research tool, PET scanner
ICC	Intra-class correlation coefficient
ID	Inner diameter
IEC	International Electrotechnical Commission
L/B	Lesion to background ratio
lld	Low level discriminator
LM	List Mode
LS	Line source
IQ	Image quality
LSO	Lutetium oxyorthosilicate

ABBREVIATIONS

LYSO	Yttrium doped Lutetium oxyorthosilicate
ML-OSEM	Iterative reconstruction method (Maximum likelihood with ordered-subset expectation maximisation)
MR	Magnetic resonance
MRI	Magnetic resonance imaging
NEC	Noise equivalent count rate
NEMA	National Electrical Manufacturing Association
NU 2-1994	NEMA standard 1994
NU 2-2001	NEMA standard 2001
NU 2-2007	New NEMA standard 2007
PET	Positron emission tomography
PET/CT	Combined PET and CT tomography
PSF	Point spread function
PV	Partial volue
PVC	Partial volume effect correction
PVE	Partial volume effect
PVEOut	Partial volume correction software package
QRS	QRS Complex of the heart beat
RDF	Raw data file
ROI	Region of interest
RSF	Radiation distribution function
RPM	Real time position management
RX	Discovery RX PET scanner
SD	Standard deviation
SF	Scatter fraction
SRTM	Simplified reference tissue model
SNM	Society of Nuclear Medicine
SNR	Signal to noise ratio
SPM	Statistical parametric mapping
ST	Discovery ST PET scanner
STE	Discovery STE PET scanner
SUV	Standardised uptake value
TOF	Time-of-Flight
VAR	Test-retest variability
VCT	Discovery VCT PET scanner
VOI	Volume of interest
WM	White matter

LIST OF ORIGINAL PUBLICATIONS

This dissertation is mainly based on the following original articles, which are referred to in the text by the corresponding Roman numerals I – IV. In addition unpublished data are presented.

I Teräs M, Tolvanen T, Johansson J, Williams J, Knuuti J: Performance of the new generation of whole-body PET/CT scanners: Discovery STE and Discovery VCT. *Eur J Nucl Med Mol Imaging*, 34:1683-1692, 2007.

II Merisaari H, Teräs M, Hirvonen J, Nevalainen O, Hietala J: Evaluation of partial volume effect correction methods for brain Positron Emission Tomography: Quantification and reproducibility**.** *J Med Phys*, 32:108-117, 2007.

III Kokki T, Teräs M, Sipilä H, Noponen T, Knuuti J: Dual gating method for eliminating Motion-Related inaccuracies in cardiac PET. 2007 IEEE Nuc Sci Symp Conf Rec: M19-231.

IV Teräs M, Kokki T, Durand-Schaefer N, Noponen T, Pietilä M, Kiss J, Sipilä HT, Knuuti, J: Dual-gated PET for robust correction of cardiac and respiratory motion – first clinical results (submitted to Eur J Nucl Med Mol I).

The original articles have been reprinted with the permission of the copyright holders.

1 INTRODUCTION

Even though the Positron emission tomography (PET) method was developed in the 50's and the first commercial tomographs were available from the mid 80's, the real breakthrough of the technology has occurred during the past ten years [Wagner et al. 1998; Budinger et al 1998]. A huge amount of development work has been done to achieve this and the close relationship between the few manufacturers and the first research centres has made it possible. There are several reasons why the method passed from research tool to a clinically appreciated diagnostic workhorse in healthcare.

The methodology is very computer intensive so the times for performing the developed algorithms needed to come down before the systems were ready for diagnostic use. Also performance measures had to be developed to compare systems from different generations and manufacturers. The work was done simultaneously in Europe and North America by representatives from manufacturers, standardising authorities and academic medical research centres. Several standards have been introduced, but as tomographs are developing and getting new features the standards also need to be revised. This has resulted also to the use of different standards for different tomographs such as whole body, brain and animal scanners.

Apart from the performance measures there are several factors that affect the image quality in PET. Partial volume effect (PVE) that is related to spatial resolution and the point spread function is one of the factors that blur the image. Several methods for correcting for partial volume are under research but no real agreement exists on how to solve it. These methods are used in brain studies and are based on anatomic information derived from MR images. Anatomic segments of grey matter, white matter and cerebrospinal fluid are fused with PET images and the convolution of activity intensities of pixels of different segments and the point spread function are calculated. One problem is the basic assumption that the activity distribution is homogenous inside each segment. As the activity accumulation in a lot of brain studies represents receptor densities the assumption is not necessarily true.

The introduction of a PET scanner combined with a CT scanner was a breakthrough in PET methodology becoming a clinical tool. Studies are reimbursed mostly in the fields of oncology and radiotherapy planning, where anatomic information from CT adds value in interpreting PET uptake. The CT scan is also used for attenuation correction of the PET study. In whole body studies with this more precise anatomic information more attention is drawn to the motion of the patient both between CT and PET studies and during them. The main reasons for movement in the thoracic region are respiratory and cardiac motions. Both motions are periodic and the period can be measured with auxiliary devices. In cardiac studies with gamma cameras gating using the signal from an electrocardiogram (EKG) has been routine for decades. The technique also has been available in PET, but there have not been real applications on it. Respiratory gating in small lesion detection of the thoracic region has become possible as the new scanners are equipped with both gating options, but the drawback is that only one gating option can be used at a time. With the introduction of list mode

(LM) acquisition where histogramming to sinograms can be performed retrospectively, it is possible to have triggering from both movements in the LM stream.

New imaging targets such as plaque or molecular imaging of new therapies require better control of the cardiac motion also caused by respiratory motion. To overcome these problems in cardiac work a dual gating approach has been proposed.

2 REVIEW OF THE LITERATURE

2.1. PET Performance standards

Most PET scanner performance tests are made for one of three reasons: (a) by the manufacturer to test and specify the equipment, (b) by the customer to test new equipment against the manufacturer´s claims, and (c) by the user as part of a periodic quality-control programme [Muehllehner et al. 1981].

In North America the National Electrical Manufacturing Association (NEMA) has a nuclear section and the aim of this organisation is to create standardized measurements of scanner performances and to include all designs of scintillation cameras within the scope of these standards. The first standard was published before the PET era for gamma cameras [Standards Publ. 1980]. It covered both single- and multiple-crystal scintillation cameras but when coincidence imaging with multiple head cameras and, finally, dedicated PET tomographs became commercially available, new standards for positron emission tomography were developed.

A task group from the Society of Nuclear Medicine (SNM) proposed a set of measurements that were published by Karp et al. [Karp et al. 1991]. After this, NEMA formed a committee with members from PET manufacturers and the SNM task group. The NEMA committee refined tests defined by SNM and proposed the standard NU 2-1994 [National elec. 1994].

Almost at the same time the European Economic Community made a concerted effort to develop measurements for PET scanners which resulted in the International Electrotechnical Commission standard IEC 61675 [International Elec. 1998]. IEC is a worldwide organisation for standardisation comprising all IEC national committees. The IEC and NEMA standards do overlap but differ in many specific details and therefore the results cannot be directly compared. Typically the measurements are done using only one of them. It is important to note, however, that some tests are complementary.

The task group for the first NEMA standard (NU 2-1994) claimed that three important tasks must be carried out to accomplish these measurements. The first is to establish a common methodological language that clearly defines the experimental measurements. The second is to develop tools for performance evaluation and to provide reliable tests that are usable for different types of scanners. The third is to structure the tests so that they can be used to understand and predict the accuracy of the data from realistic in-vivo studies [Karp et al. 1991].

The first NEMA standard included several systems such as brain and body scanners as well as time-of-flight and non-time-of-flight systems, discrete and continuous detector designs, single and multiple slice devices, multi-planar and volume imaging systems [National elec. 1994]. The rapid development of oncological whole body PET as a diagnostic tool led to a clear need to create the NU 2-2001 standard already a few

years later [National elec. 2001]. The new standard was compared with the old one by Daube-Witherspoon et al. [Daube-Witherspoon et al. 2002]. The growth of 3D acquisition required some clarifications to the old standards. But, as the NU 2-2001 concentrates on whole body imaging for oncology applications, it may not accurately represent the performance in brain applications.

The third NEMA standard has come out recently [National elec. 2007] and takes into account the fact that the newest crystals (LSO, LYSO) have intrinsic radioactivity and thus the randoms rate is never zero. In some old NEMA measurements the randoms rate should be less than 1% of the trues rate and this is not met with these crystals. This new standard will also recognise the new PET scanners with combined with X-ray computerized tomographs (CT). Currently, CT carries out the task of performing the attenuation correction for the PET and this issue will be revised in the new standard.

According to the standards the main performance parameters are divided into two groups [Karp et al. 1991]. The first group includes basic intrinsic measurements:

- spatial resolution in axial and transaxial directions
- true sensitivity
- count rate capabilities
- scatter fraction.

The second group includes measurements of the accuracy of corrections for physical effects, specifically:

- uniformity correction
- scatter correction
- attenuation correction
- count rate linearity correction

The tests require specific phantoms that either come with the purchase of the scanner as they are utilised later for quality assurance measurements or need to be borrowed or purchased for the acceptance testing period of the new scanner.

Today there are also other possible tests to be added to the list of acceptance or performance tests such as:

- noise equivalent count rate
- partial volume and spillover
- motion artefacts
- image quality test
- PET/CT image co-registration

Furthermore, it is required that all measurements are performed without altering any basic parameters of the system from the settings used in patient work. These include energy discrimination windows, coincidence timing window, pulse integration time, and reconstruction algorithm with associated parameters such as pixel size, slice thickness, axial acceptance angle and smoothing.

It is also stated that all tests should be performed with the same and the easiest accessible nuclide, ^{18}F, in a form that dilutes freely to water. Substitution to other nuclides such as [68]Ge or ^{68}Ga can lead to significantly different results due to differences in positron energy (and range) and activity calibration (branching ratio).

Some of the measurements give quantitative values and it is assumed that all other equipment such as dose calibrators and well counters used for these measurements are calibrated against or traceable to a reference source.

One limitation of the currently used standards (NU 2-1994 and NU 2-2001) is that they have been developed for whole body tomographs with a patient port larger than 260 mm (or 350 mm in NU 2-2001 IQ test). For dedicated brain or animal tomographs these tests apply only partially. For small animal PET a performance standard is in the draft phase [National elec. 2008]. However, with these special scanners the measured performance parameters are practically the same. The biggest differences are in phantom designs as the port and Field-of-view (FOV) are smaller. Another main difference is that animal scanners function only in 3D mode so there is no need (or possibility) to measure 2D performance.

2.1.1. Spatial resolution

There are a variety of ways to approach the subjective issue of our ability to resolve objects on an image. By definition, spatial resolution is "the ability to distinguish between two closely spaced objects on an image" [Sabins 1987] and it can be pointed out that spatial resolution is "not the size of the smallest object that can be seen" [Hoffman et al 1979]. The purpose of the measurement is to characterise the width of the point spread function (PSF) of a compact radioactive source in the reconstructed image. The results are measured by its full width at half-maximum (FWHM) and full width at tenth-maximum (FWTM) values. For accurate results the sampling must be adequate. The NEMA and IEC standards specify that the pixel size in all directions should be made no more than one-third of the expected FWHM [National elec. 2001]. This comes from the Nyquist theorem [Nyquist 1928] or Nyquist-Shannnon theorem [Shannon 1949] that states that sampling has to be at least double for the smallest feature to be modelled. Sampling is the process of converting a signal (for example, a function of continuous time or space) into a numeric sequence (a function of discrete time or space).

Spatial resolution is measured in the transverse slice (in plane) in two directions (tangentially and radially). In addition, the axial resolution is measured (Fig. 2-1).
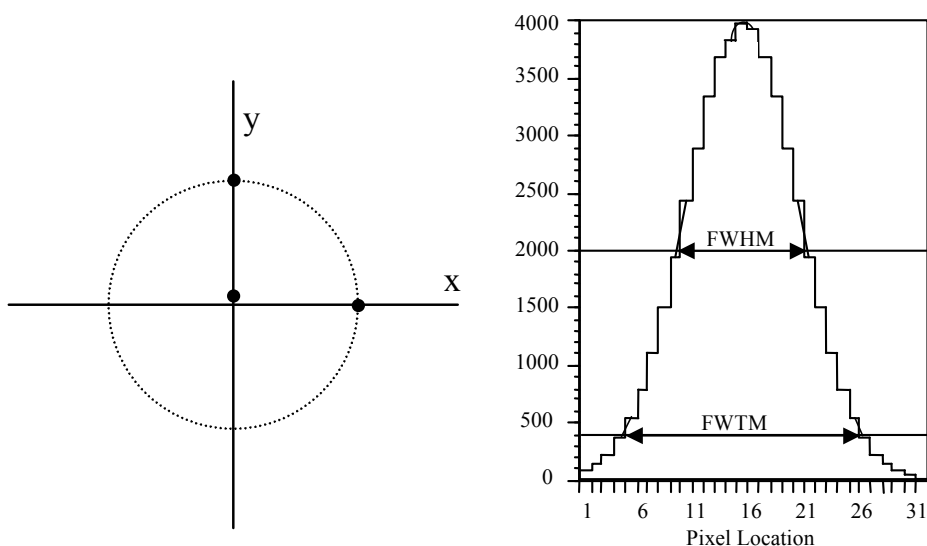
Figure 2-1. a) point source positioning to the distance of 10 cm from the origo in x- and y-direction and 1 cm outside the origo (to avoid the centre of FOV effect) b) calculation of resolution from a point source profile with FWHM [National elec. 2001].

Measurements are done with a small point or a line source. The dimension of the source in the direction measured should be less than 2 mm in NU 2-1994, less than 1 mm in NU 2-2001. The IEC defines that the source approximates the delta function. As the resolution improves the recommended size of the sample also needs to be smaller. In animal scanner recommendations (NU 2-2008) the diameter has diminished to 0.3 mm. The radioactivity levels of the ^{18}F sources should be less than that where dead-time losses exceed 5% or the random coincidence rate exceeds 5% of the total event rate. At least 50 000 counts in IEC and NU 2-1994 and 100 000 counts in NU 2-2001 should be acquired in each response function. Reconstruction of all resolution data is performed by the filtered backprojection method with no smoothing. No reconstruction is needed for the axial slice width data.

NU 2-1994 resolution

In NU 2-1994 the transverse resolution is done with a line source in air and the axial resolution with a point source in air if the axial sampling of the tomography is less than one-third of the FWHM.

The line source is positioned at the radial positions of (x,y) = (0,10), (0,50), (0, 100), (0,150), (0,200), (50,0), (100,0), (150,0), (200,0), where x and y are coordinates from the centre of the transverse field of view (FOV) in millimetres. The last points (0,200) and (200,0) need to be measured only if the FOV exceeds 310 mm.

The point source is measured at radial intervals of 50 mm starting from the centre of the transverse FOV and at axial intervals of 20 mm, starting at the centre and extending within 10 mm from the edge of the axial FOV.

NU 2-1994 Axial slice width

In NU 2-1994 also the response of the point source in air is measured. The point source is moved with small increments over the axial length of the tomography (Fig. 2-2). The increment should be one-tenth of the expected FWHM in the axial direction. The incremental measurement is done in 4 (or 5) positions (r = 0, 50, 100, 150, 200mm) depending on the FOV of the tomography.
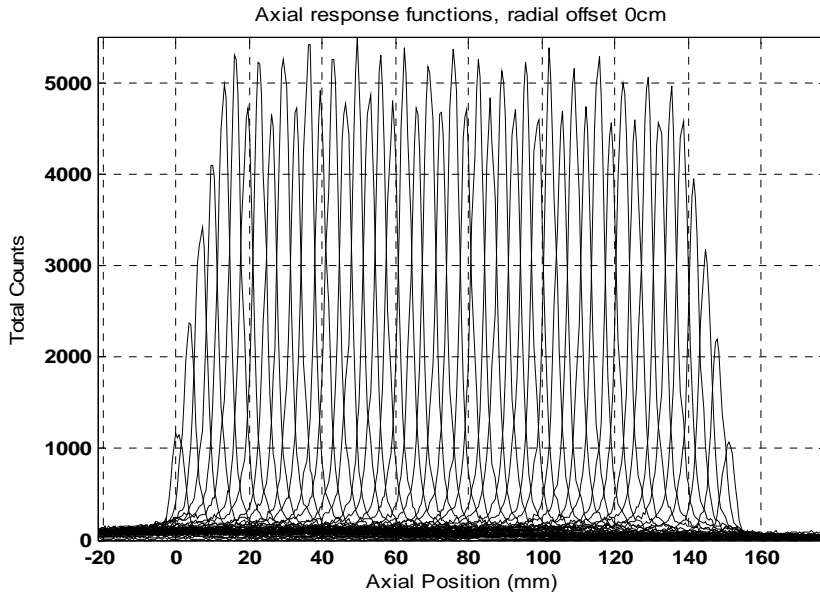
Figure 2-2. Axial slice width according to NU 2-1994. Intensity measured when the point source is moved across the axial FOV is shown. The peaks resemble the slice centres and slice width is the distance between peaks.

NU 2-2001 resolution

In NU 2-2001 both the transverse and axial resolutions are done with a point source. The number of measurements is much smaller than in NU 2-1994 and thus it does not represent the PSF to the same extent. The transaxial measurement points are (x,y) = (1,0), (10, 0) and (0,10) and axial positions at the centre of axial FOV and at ¼ of axial FOV. It should be noted that to get an acceptable axial resolution the slice width should be in the order of 1.5 mm to be able to measure FWHM values that are in the order of 4.5-5.0 mm. This is not the case with present tomographs with slice thicknesses in the order of 2.5 -4.0 mm.

IEC-1998 resolution

In IEC the transverse resolution is done with the same method as in NU 2-1994, but it also gives the possibility to use a point source for axial resolution if the axial sampling is adequate. The main difference is that the resolution or the width of the spread function is measured not only by the FWHM but also by the Equivalent width (EW). Equivalent width is the rectangle having the same area and the same height as the response function as defined in International Elec. page 12. [1998].

17

2.1.2. Sensitivity

Sensitivity is expressed as the rate in counts per second (CPS) at which true coincidence events are detected for a given source strength. For most tomographs the sensitivity varies with axial location and an axial sensitivity profile is also measured. Results are scatter corrected to obtain units of counts per second per MBq.

NU 2-1994 Sensitivity

The NEMA NU 2-1994 recommendations are split into two: the system sensitivity and the relative sensitivity.

The system sensitivity is measured with a cylinder (diameter 20cm and length 20 cm) filled with low activity concentration of ^{18}F with dead time losses and a random coincidence rate of less than 2%.

The relative sensitivity profile test measures the response of a point source in air. The source is moved in small increments along the entire axial length. The axial increment should be one tenth of the expected FWHM as measured with the axial response function test. Data from the axial slice width test may be used.

The slice sensitivity, S, for unscattered events is calculated as:

$$S = \frac{C_{TOT,120}}{T_{acq}} \frac{1 - SF}{a_{ave}}$$
(2-1),

where $C_{TOT,120}$ is the total counts in each slice within a radius of 120 mm, a_{ave} is the average activity in the phantom during the time of the measurement, T_{acq} is the duration of the acquisition, and SF is the scatter fraction of each plane. The total system sensitivity, S_{TOT} is the sum of S over all slices.

The relative sensitivity profile is calculated by summing the counts in each response function. The axial response function for each slice is normalised by dividing the counts collected at each step by the calculated relative point slice sensitivity. The normalised axial response function is plotted against distance in mm on a single graph. Peak and valley values for each pair of slices are recorded and peak to valley ratios calculated, as well as the average peak to valley ratio.

NU 2-2001

Since the emitted positrons annihilate and create a pair of gamma rays, a significant amount of surrounding material is needed to insure the annihilation. But this material attenuates the gamma rays prohibiting the measurements without interfering with the attenuation. A new measurement technique has been proposed by Bailey et al. [Bailey et al. 1991b]. In this technique successive measurements are made with a uniform line source surrounded by absorbers of different known thicknesses (Fig. 2-3). From these measurements the sensitivity with no absorbers is extrapolated. The measurement is done with a 70 cm long line source with known low activity concentration of ^{18}F. The line source is positioned along the centre of transaxial FOV and repeated at a 10 cm

radial offset from the centre of the transaxial FOV. Sensitivity for each of the radial offsets in counts/sec/MBq, as well as the axial sensitivity profile, is reported.
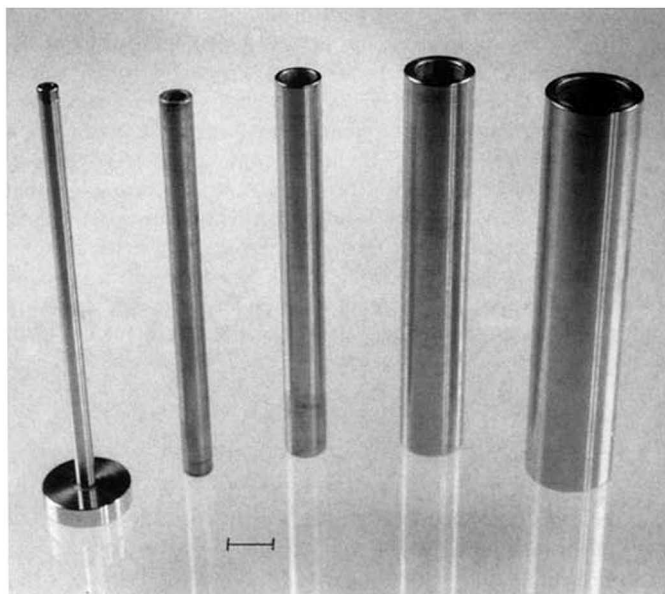
Figure 2-3. Source holder and aluminium sleeves (or tubes) for measuring absolute sensitivity (1 cm is indicated by the *marker)* with NU 2-2001 protocol [Bailey et al. 1991b].

IEC 1998

In the IEC 1998 the test is divided into two parts as in the NU 2-1994. The first part, **the system sensitivity test**, is identical to NU 2-1994.

In **The relative sensitivity profile test**, the normalised slice sensitivity nS for each slice is calculated from:

$$nS = S / EW_a \tag{2-2},$$

where S is the slice sensitivity for unscattered events as described in (2-1) and EW_a is the axial slice width from the IEC 1998 measurement.

2.1.3. Count losses and randoms measurement

This measurement expresses the ability of a tomography to measure highly radioactive sources with accuracy. This is done by measuring the system dead time and the generation of random events at different radioactivity levels (Fig. 2-4). This is achieved by placing a relatively high activity of ^{18}F in the field of view of the tomography. As the activity of the source decays, the system efficiency for detecting coincidence events improves and, at low levels count losses are negligible. This is used to calibrate the response of the system for estimating count losses at higher activities. In 3D mode, higher true coincidence count rates are achieved with lower activities than in 2D mode. Also trues, randoms and scatter rates differ in 2D and 3D. Because of difficulties to assess the advantages of 3D over 2D mode, a new concept of noise equivalent count

rate (NEC) was proposed by Strother et al. [Strother et al. 1990]. In the new NU 2-2001, NEC is one of the performance standards and is used to evaluate the real improvement due to 3D [Bailey et al., 1991a].
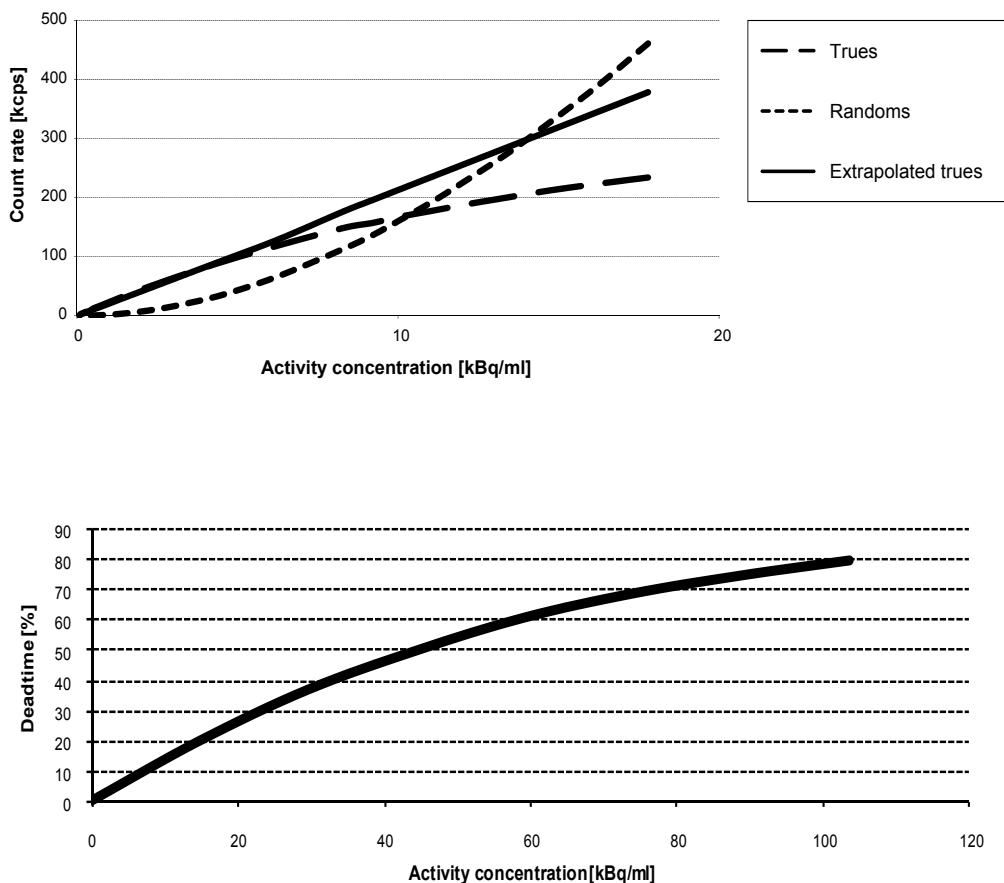
Figure 2-4. Count loss graph in NU 2-1994 with Trues, Randoms and extrapolated trues rates with different activity concentrations (top) and related dead time percentages (bottom). Phantom (length 20cm, diam 20cm) is measured in 2D-mode

NU 2-1994

In NEMA NU 2-1994 a cylindrical phantom (diameter 20 cm and length 20 cm) is filled with an even distribution of ^{18}F and the measurement lasts until the count loss rate of true events is less than 1% of the total and the random rate is less than 1% of the true counts. To collect enough counts for statistical purposes, the manufacturer should recommend a protocol including starting activity concentration, acquisition times and the duration. Raw data sinograms are used in the analysis. Single event rates or a delayed event circuit can be used to estimate random coincidences during acquisition. The total (trues + scatter + random), R_{t+s+r}, count rate and the random coincidence rates (R_r) are measured. Trues + scatter (R_{t+s}) count rate is calculated from $R_{t+s+r} - R_r$ and plotted as a function of the radioactivity decay. As a result a linear interpretation,

T_{extrap}, from the last measured points, where random and dead time (DT) is negligible, is used to determine the activity concentration at which the dead time loss is 50 %.

$$DT\% = 100 - 100 \frac{T_{t+s}}{T_{extrap}},$$ (2-3),

where DT% is the dead time percentage, T_{t+s} is the calculated function of trues+scatter count rate and T_{extrap} is the extrapolated trues+scatter countrate. The trues rate, T_t, was determined by subtracting the scatter fraction (SF) result from section 2.1.4. As a result a linear interpolation is used to calculate the rate and activity concentration where the system trues rate equals the system randoms rate.

NU 2-2001

The same phantom and data are used as in the NEMA NU 2-2001 scatter fraction measurement (see p. 24). The acquisition has the same restrictions as NU 2-1994 and is recommended by the manufacturer. The test is done both in 2D and 3D mode. The total counts rate within the 24 cm transverse FOV was determined as a function of the radioactivity decay. The trues rate, T , was determined by subtracting the random, R, and previously defined scatter, S, rates from the total prompts event rate. The NEC rate was calculated as:

$$NEC = \frac{T^2}{T + S + kR}$$ (2-4),

where the factor of k=2 is used if the direct randoms subtraction is used, otherwise k=1 should be used. An example of system plots are shown in Figure 2-5.
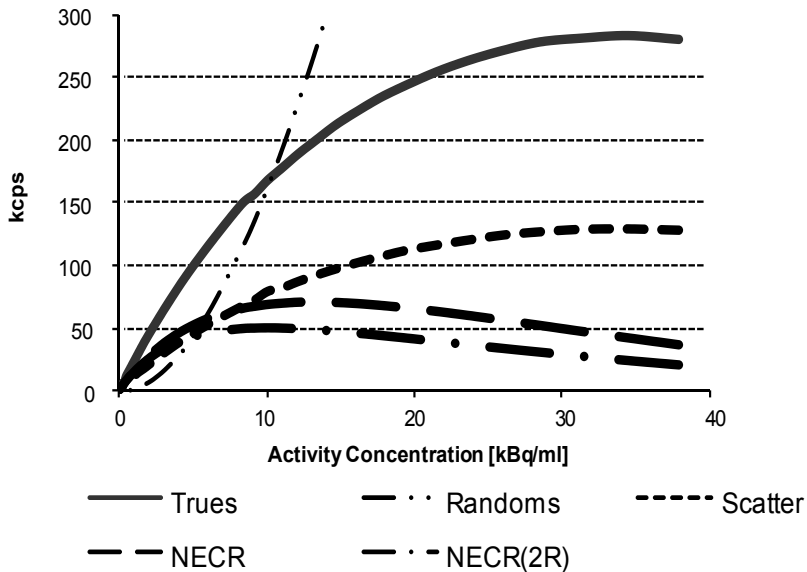
Figure 2-5. Count rate curves of NU 2-2001 also presenting scatter and noise equivalent count rate curves. The measurement represented here is done in 3D mode

IEC 1998

In the IEC count rates characteristics are measured in three different set-ups corresponding to various scatter conditions (Head, heart and abdominal conditions). In the head condition, the cylindrical phantom is measured comparably to NU 2-1994. In the cardiac condition, a water filled body phantom with arms is used. The head phantom inside the body is filled with air and a rod source (21 mm inside diameter, 130 mm length) containing activity is inside the head phantom as shown in Figure 2-6. In the abdominal condition also the head phantom inside the body is filled with water as this mimics the worst case scattering condition.

The results for each condition are plotted as in NU 2-1994, and the activity levels at which the measured true coincidence count rate (including scatter) reaches 20% and 50% count loss for each slice are evaluated.

For 2D systems an additional test is performed in IEC 1998. This tests the address pile-up which is one of the courses of axial variations at high count rates [International Elec. 1998]. This is done by calculating the ratio of ROI counts per slice at each count rate, normalised to the corresponding value at the lowest rate.

$$R_{i,j} = \frac{C_{i,j}}{C_{i,low}}$$ (2-5),

where $R_{i,j}$ is the ratio of ROI counts for slice i and time frame j, $C_{i,j}$ is the ROI count for slice i and frame j, and $C_{i,low}$ is the average ROI count for slice i and the three lowest activity time frames.

Using the above division all normalising factors with respect to different efficiencies per slice are cancelled and the plot of this ratio versus slice number (for each frame) shows the address pile-up as the deviation from a line. The activity level for 5% deviation (if detected) for any slice is determined.
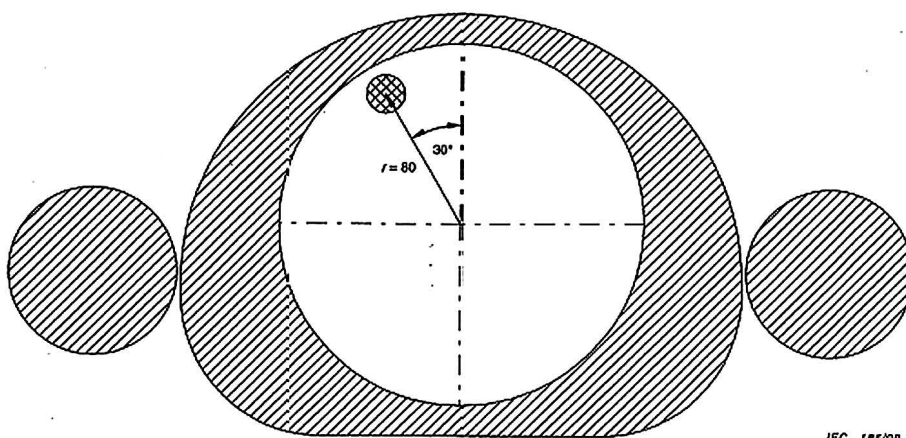
Figure 2-6. Cross section of the phantom in the IEC count rate measurement in the heart condition. Radioactive source is placed in the small cylinder (marked with crosses) inside the air filled head phantom (white area), The body and arm are filled with non-active water [International elec. 1998].

2.1.4. Scatter fraction measurement

The scattering of gamma rays emitted by the annihilation of positron results in incorrectly located coincidence events. In the first 2D only PET tomographs, the scatter fraction was in the order of 10% to 15% when measured with a line source of activity in a 20 cm diameter uniform water cylinder [Townsend et al. 1998]. This amount of scatter was not corrected at all. When 3D imaging was launched the amount of scatter increased to 30 % to 40 % in all tomographs as shown in Townsend et al. 1998. The scatter fraction with present scanners is measured and corrected individually for each scan or even for each frame.

The purpose for NEMA and IEC procedures is to measure the relative system sensitivity to scattered radiation. Scatter is expressed by the scatter fraction (SF) for the entire tomograph. In NU 2-1994, the values for SF in each slice are also calculated.
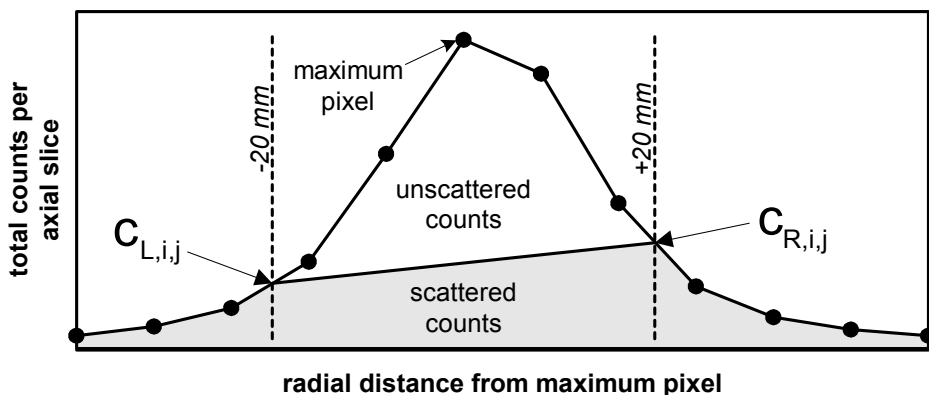
NU 2-1994 and IEC 1998 scatter

The scatter fraction measurements in NU 2-1994 and IEC 1998 are practically the same. The measurement is performed by imaging a single radioactive line source at three radial positions within a non-radioactive water filled test phantom. The nuclide is ^{18}F and the activity level should be less than that where dead-time losses exceed 5% or the random coincidence rate exceeds 5% of the total event rate. The line source is placed parallel to the axis of the cylinder in three steps, at the radii of 0, 45 and 90 mm in the axially and transaxially centred cylinder phantom (length and diameter 20 cm). At least 200000 counts per slice are acquired and same acquisition time should be used for each acquisition. Data is corrected for dead-time losses and random coincidences but not for scatter or attenuation. Unscattered events are estimated slice by slice by placing all angular profiles over each of the three measured points at sinogram level. It is assumed that only a few unscattered events lie more than 20mm from the peak (Fig. 2-7a) and a background line is drawn between the points, $C_{L,i,j}$ and $C_{R,i,j}$, where the profile is 20 mm from the peak. The summed pixel values under the background line and the contribution from outside the strip equals the estimated scattered event counts. For all positions, the projection profiles were summed over angles to generate a single average projection profile.

It is assumed that the SF in a uniform source has a slowly varying radial dependence so that the three positions and the averaged scatter component for each point are linked together (Fig. 2-7b), and a scatter factor can be calculated for each slice from the equation:

$$ SF = \frac{S}{S+T} = \frac{R_s(0) + 8R_s(45) + 10{,}75R_s(90)}{R_{tot}(0) + 8R_{tot}(45) + 10{,}75R_{tot}(90)} \qquad (2\text{-}6), $$

where R_s is the counts of scattered events (at 0, 45 and 90 mm) and R_{tot} is the total (trues+scatter) counts for each number of slices. Values 1, 8 and 10,75 are weighing factors as the annular areas of each point are in the ratios 1:8:10,75, respectively. The average of the slice SF values represents the system scatter fraction.

a)
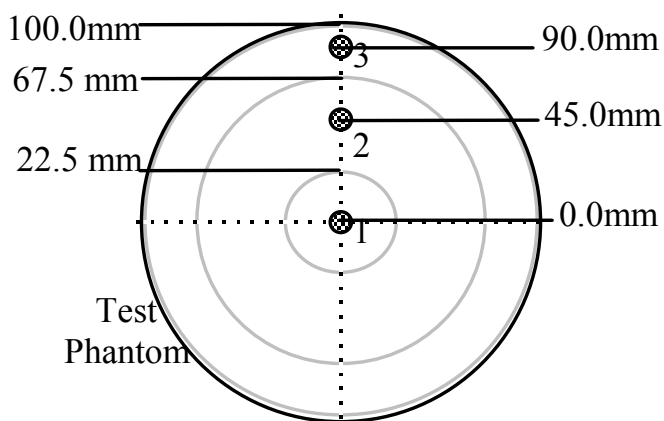
b)

Figure 2-7. a) Line source profile with the line between intercept points, $C_{L,i,j}$ and $C_{R,i,j}$, that define scattered and unscatterd events b) In NU 2-1994 and IEC, scatter is calculated from 3 points (0 mm, 45 mm, 90 mm from the centre) for the scatter fraction evaluation. Drawings from [International elec. 1998].

NU 2-2001 scatter

In NU 2-2001, Scatter is calculated from the same measurement as count losses and randoms measurement (see 2.1.3). The phantom is a 70 cm long polyethylene cylinder with a diameter of 20cm and a specific gravity of 0.96. A 6.4 mm hole is drilled parallel to the central axis of the cylinder, at a radial distance of 45 mm (Fig. 2-8). The acquisition is started with a high radioactivity concentration level of ^{18}F but only the latest frames when the randoms level are in the order of 1% are used for the scatter evaluation. The SF evaluation it self is analogical with the NU 2-1994, the only difference being that only one point is used for each slice and no weighing of the radial position is used.
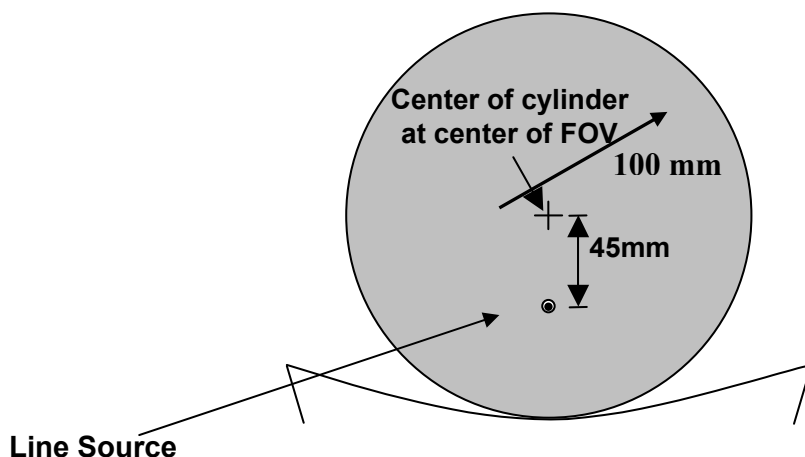
Figure 2-8. Phantom design for NU 2-2001 scatter measurement. Radioactive line source is 45 mm off-centred in the cylinder with 100 mm radius [National elec. 2001].

2.1.5. Uniformity test

Uniformity is a measure of the deviation of the tomograph from a uniform response by considering the reconstructed image of a uniform cylinder. The uniformity describes the ability to measure the same activity independent of its location within the field-of-view.

NU 2-1994

The cylinder phantom is filled with a moderate amount of ^{18}F activity so that neither the dead time losses nor the random coincidence rate exceed 20%. The phantom is centred axially in the FOV but displaced vertically 25 mm off axis. The data are reconstructed with all corrections, standard matrix and pixel size and ramp filter with cutoff at nyquist frequency. The reconstructed images are analysed by determining the number of counts in an array of contiguous 1 cm x 1 cm ROIs inscribed within a circe 175 mm in diameter centred in the phantom image. The negative and positive non-uniformities, NU- and NU+, respectively, are estimated for each slice according to the equations [Karp et al. 1991]:

$$NU+ = +(C_{max} - C_{avg}) / C_{avg} \qquad (2-7),$$

$$NU- = -(C_{avg} - C_{min}) / C_{avg} \qquad (2-8),$$

where C_{max} and C_{min} are the maximum and minimum number of counts within any square ROI in a slice and C_{avg} is the average number of counts over all regions within the same slice. The same method can be applied for the volume non-uniformity. Also standard deviation (SD) and coefficient of variation (CV) can be calculated.

NU 2-2001

Uniformity is handled in the Image Quality chapter

IEC 1998

No test has been specified in IEC 1998 for uniformity as it declares that all known methods so far mostly reflect the noise in the image.

2.1.6. Scatter, attenuation and count rate linearity corrections

To achieve quantitative source distributions under widely varying conditions each tomography as its compensation algorithms for scatter, attenuation and count rate losses. The accuracy of these corrections is also tested with the performance tests. Some of the tests can be performed from the same data used to calculate these losses but in some tests new acquisitions and new phantoms are used.

NU 2-1994 accuracy of corrections

Scatter correction

A cylindrical test phantom filled with a measured amount of radioactivity mixed with water is axially centred in the FOV is off-centred radially by 25 mm. A hollow 50 mm insert filled with non-radioactive water is placed 60 mm from the axis inside the cylindrical phantom. The phantom is scanned and reconstructed with standard matrix, corrected for attenuation and pixel size, and ramp filter with cutoff at nyquist frequency. Region of Interest (ROI) analysis is performed by defining 12 ROIs, each 30 mm in diameter. One of the ROIs is centred over the non-radioactive insert. For each slice the remnant scatter fraction after scatter correction is calculated by comparing the activity of the ROI of the cold insert to the average of the other ROIs.

Attenuation correction

The accuracy of attenuation correction for areas of different densities is tested by a cylindrical ^{18}F filled water phantom with three non-radioactive inserts. The three 50 mm diameter cylinder inserts are placed 60 mm from the axis of the phantom. One hollow insert is filled with water, another with air and the third with known material like Teflon. The emission data is reconstructed with all corrections, standard matrix and pixel size and ramp filter with cutoff at Nyquist frequency. Three circular ROIs 30 mm in diameter are centred in the air, solid and water insert images and nine similar ROIs in the uniform activity area. Each insert is compared with the average of the nine uniform ROIs for each slice.

Count rate correction

The test phantom data for measuring count rate losses is used by reconstructing the data with all corrections, standard matrix and pixel size and ramp filter with cutoff at nyquist frequency. The comparison is done between 180 mm diameter ROIs centred in all slices and the extrapolated count rate from the low count rate data. For each slice the relative count rate error is tabulated.

NU 2-2001 accuracy of corrections

Scatter and attenuation correction

Accuracy of attenuation and scatter correction is handled in the Image Quality chapter.

Count rate correction (same than in NU 2-1994)

The test phantom data for measuring count rate losses is used by reconstructing the data with all corrections, standard matrix and pixel size and ramp filter with cutoff at nyquist frequency. The comparison is done between 180 mm diameter ROIs centred in all slices and the extrapolated count rate from the low count rate data. For each slice the relative count rate error is tabulated.

IEC 1998 Accuracy of corrections

Scatter correction

Not done in IEC 1998 recommendations.

Attenuation correction

Accuracy of the attenuation is done with the same method as in the NU 2-1994.

Count rate correction

The images are reconstructed images as with NU 2-1994. The maximum deviation from linearity up to the saturation point and the corresponding activity for any slice for the three scatter conditions are reported.

### 2.1.7. Image quality test (only in NU 2-2001)

Because of the complex interplay of different aspects of the system performance, it is desirable to compare image quality in a situation that simulates clinical imaging conditions. Due to variations in patient sizes and shapes the phantom study is only indicative. In the NU 2-2001 a total body imaging study with both hot and cold lesions (spheres) of different diameters is simulated (Fig. 2-9) [Adam et al. 2001].

The IEC NEMA body phantom set is used for these tests and can be found from (http://www.spect.com/pub/NEMA_IEC_Body_Phantom_Set.pdf). A cylindrical non-active lung insert is placed axially in the middle of the phantom. The hot lesions and the background are filled with known activities and the test is done with different lesion to background radioactivity concentration ratios both in 2D and 3D modes. The body phantom is positioned axially in the scanner so that the centres of the spheres are in the middle slice of the scanner. The scatter phantom used for the NU 2-2001 scatter fraction measurement with the line source filled with ^{18}F radioactivity is placed at the head end of the body phantom in order to approximate the clinical situation of having activity that extends beyond the scanner (activity outside the FOV). All slices are reconstructed with all available corrections applied to the data and using the standard parameters for whole body studies.

Circular ROIs are drawn in the transverse image centred on the cold and hot spheres. All ROIs should have a diameter as close as the sphere and similar size on the background ROIs is used for the contrast calculations.

Percentages of the calculated true activity detected in hot lesions of different diameters represent the system recovery resembling the recovery coefficient measurement of the IEC 1998 standard (see next paragraph). Evaluating the cold lesion

and lung insert spillover activities as well as background activities are used for determining the accuracy of the scatter and attenuation corrections, respectively.
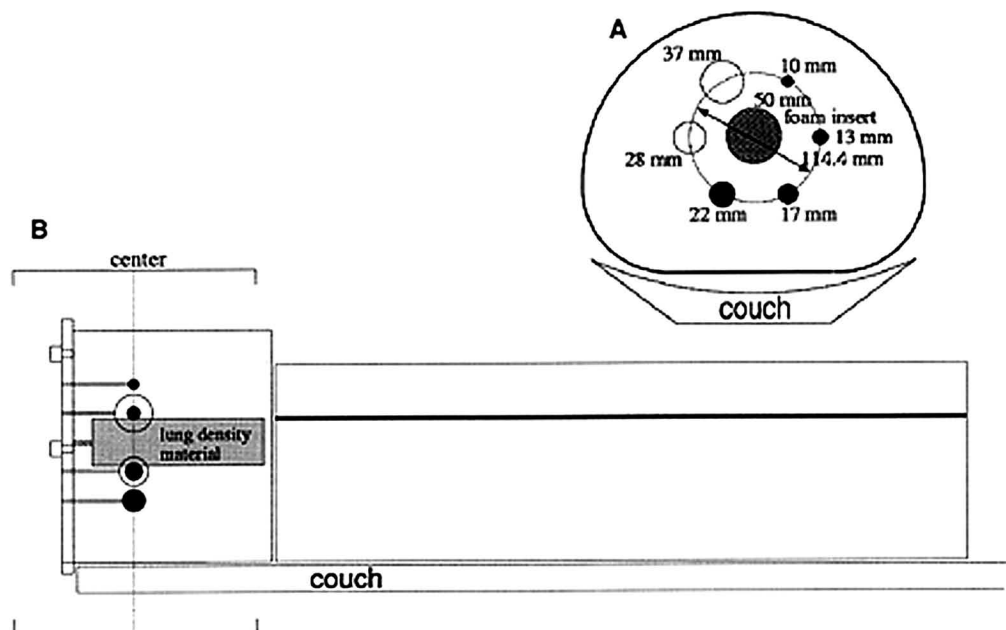
Figure 2-9. Transaxial (A) and axial (B) views of phantom setup for image-quality measurement. Four smallest spheres are hot, and 2 largest spheres are cold. Foam insert has density of 0.3 g/ml [Adam et al. 2001].

2.1.8. IEC Recovery coefficient (only in IEC 1998)

Recovery coefficient is determined only in the IEC 1998 standard. But this test resembles in some extend parts of the image quality test in NU 2-2001. But as image quality test mimics a clinical situation the recovery coefficient test is a physical performance test as all other tests in all recommendations apart from just the image quality test.

The finite resolution of a tomography leads to a spreading of image counts beyond the geometrical boundaries of the object as seen in resolution tests. This effect becomes more important as the object size decreases below approximately 4 times the FWHM. The recovery coefficient provides an assessment of the ability to quantify the activity concentration as a function of the object size. This effect is related to the partial volume effect assessed in the next chapter.

In IEC 1998 it is stated that recovery coefficient should be measured at different ring positions (direct and cross planes in 2D mode) and also at halfway between slices in order to see the worst case of the tomogram.

A number of hollow spheres are filled with a known radioactivity concentration of ^{18}F from a stock solution and placed in the water filled head phantom. The head phantom is placed in the centre of the transverse FOV without introducing additional attenuating material.

Reconstruction is performed using a ramp filter with a cut-off at Nyquist frequency and with all corrections applied. A circular ROI with a diameter as close as possible to the earlier measured FWHM is placed centrally on each sphere. A graph of recovery coefficient for each axial position is reported.

2.1.9. PET/CT image co-registration

With the introduction of PET/CT tomographs also the co-registration of PET and CT images has become part of the performance testing. In past anatomical information was imaged on a separate session with CT or MR. The images were compared visually by the observer or fused with software developed for the purpose. Latest commercial software has shown to work relatively well in brain area as the correction can be regarded linear [Hawkes et al. 2003]. In other parts of the body where movement is nonlinear affine transformations or warping have been used and show that software fusion can achieve an accuracy of half a pixel, or 2-3 mm, in some applications [Hutton et al. 2003], but is not particularly encouraging for ex. in applications such as recurrent colorectal cancer [Kim et al. 2005]. In the hardware approach the anatomic and metabolic information is scanned during the same session although not necessarily simultaneously. In PET/CT scanners the time difference of up to 20 minutes between the less than 1-minute CT attenuation correction scan (CTAC) with anatomic information and the whole body PET scan can induce movements by the patient. Also the bed design has to take in to account that it is moved 70-80 cm between the CT and PET acquisitions. The alignment of bed position has to be controlled during the installation by the manufacturer. Alignment is not yet included in standards.

Although image co-registration is mostly solved by PET/CT technique it is not solving the problem of periodic movements during the study. These movements are addressed in chapter 2.3.

2.2. Partial volume effect

Positron emission tomography is designed to provide in vivo quantitative estimates of metabolism, blood flow, or neuroreceptor concentration. The limited resolution results in errors in radioactivity concentration in small structures. This is evident in heart studies with varying myocardium thickness, in small lesion studies of unknown size in oncology and in the brain studies with complex anatomy. This problem has been shown typically in brain studies where cerebrospinal fluid (CSF) spaces produce significant underestimation to radioactivity concentrations of other adjacent small structures. Brain study results are also affected from brain atrophy resulting to problems with normal value comparisons both within disease and age.

This phenomenon is called the partial volume effect (PVE) which is actually related to two distinct phenomena the point spread function (PSF) and thus to the spatial resolution or full width of half maximum (FWHM) and to image sampling (or pixel size). Because of limited spatial resolution, the accurate interpretation of PET data is obscured by PVE [Hoffman et al. 1979, Mazziotta et al. 1981]. In general, one-dimensional object like a line with a constant activity the two-dimensional image

perpendicular to the line is supposed to be a point and the profile across the point represents the activity concentration highlighting the point. In reality the point is spread out according to the spatial resolution of the imaging device. It has a Gaussian shape and the value of FWHM represents the resolution. The spatial resolution in turn is limited by the detector design and the reconstruction process [Moses et al. 1993] The area under curve is the same than the area under the curve in ideal case (Fig. 2-10). This results to the fact that the smaller the object (ie. point of activity) the higher radioactivity concentration is needed to differentiate it from the background and noise and, furthermore, the quantification and the size of the object is wrong.

Image sampling is done with a voxel grid where the contour of the object does not match with it. This results to the mix of different types of tissues in the edge pixels averaging pixel values. This phenomenon is called the tissue fraction effect and can be partly overcome by decreasing the voxel size with the cost of increasing the noise as each voxel has fewer counts.
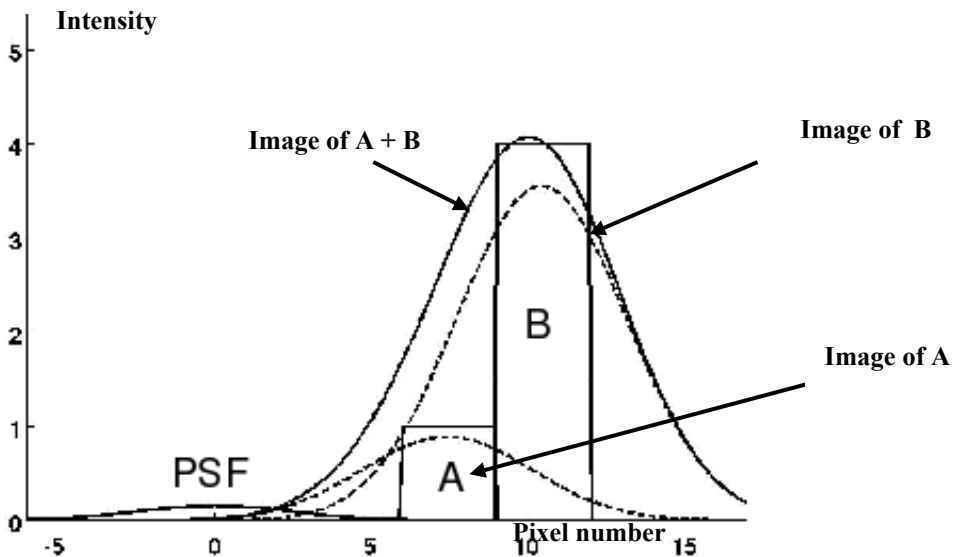
Figure 2-10. The effect of PSF on activity distribution. Activities A and B are summed and the distribution becomes blurred. Activities A and B are not separable.

The PSF relates to PVE in the case when we instead of a point think of a volume consisting of hundreds of points with homogenous radioactivity concentration. In the image of the volumetric object the inner part of the volume spreads out but the spillover from the outer part of the volume compensates for this resulting to a small portion of the volume to reach the real activity concentration of the object.

The percentage relation of object and image activity in function of object size is called recovery. Recovery function has been used for correcting the myocardium

activity in heart studies. Recovery percentage can be measured with phantom experiments (see paragraph 2.1.8).

When evaluating the influence of spatially heterogeneous background activity on "hot object" quantification in brain emission hot objects are significantly influenced by both "spill-out" and "spill-in." Qualitative and quantitative analyses of such objects must explicitly consider both spill-out and spill-in; this implies a correction scheme that goes beyond simple division of the observed value by a conventional recovery coefficient [Links et al. 1996].

Assessment of PVE was first reported to require knowledge of the size and shape of the structures of interest, of their relative position in the scanner gantry, and of the presence of surrounding high or low activity [Hoffman et al. 1979, Mazziotta et al. 1981, Müller-Gärtner et al. 1992], which all differ individually and can not be modelled with simple phantom studies. Methods using X-ray CT to correct mainly the effect of atrophy was described by Herscovitch et al. and Chawluk et al. [1986, 1987].

When fusion of PET images with structural MR images came possible methods of defining borders of different structures such as white matter (WM), grey matter (GM) and cerebrospinal fluid (CSF) and assuming that the activity is homogenously spread in each compartment became available for correcting for the PVE.

2.2.1. Corrections for partial volume effect

Various methods for partial volume effect correction (PVC) have been proposed. The simplest way is to use the recovery coefficient (RC) presented in chapter 2.1.8. The RC can be calculated as a function of tumour size and sphere to background ratios as a function of spatial resolution values [Hoffman et al. 1979, Kessler et al. 1984]. This approach has been used in several PET studies [Avril et al. 1997, Geworski et al. 2000, Hickeson et al. 2002]. The major drawback of this approach is that the tumour is mostly assumed to be spherical with a homogenous uptake in a homogenous background.

Method reported by Meltzer et al. [1990] corrects the radioactivity values of the conjunction of the brain white matter (WM) and grey matter (GM) regions. The methods of Müller-Gärtner et al. [1992] and Alfano et al. [2004] process the WM and GM regions separately and use an estimate of the true WM mean radioactivity when correcting the radioactivity values of the GM region. Method proposed by Rousset et al. [1998a] corrects the mean values of regions of interest (ROI). Most methods have been further refined [Reilhac et al. 2000, Aston at al. 2005] and the robustness of PVC methods against errors in their processing steps such as MRI-PET co-registration and MRI segmentation has been considered in several studies [Frouin et a. 2002, Labbé et al. 1996, Meltzer et al. 1999, Quarantelli et al. 2004]. The method of Meltzer et al. has been reported to be robust to errors in pre-processing and in homogeneities in the PET image [1999].

It is notable that the methods amplify the existing noise [Aston et al. 2002]. An increase of variance in the time-activity curves has been reported when using the

method by Rousset el al. [2000]. The usefulness of recovering the regional mean radioactivity decreases with noise amplification. Further, when dispersion in image voxels is high, it is difficult to conclude whether small differences in images or regions originate from real differences, or if they are caused by the data-collecting and reconstruction processes [Zaidi et al. 2004].

The PVE is generally modelled as a convolution of the real activity values with the Point Spread Function (PSF), and some additional noise:

$$I_{PET,obs} = I_{PET,true} \otimes I_{PSF} + noise \,. \tag{2-9}$$

where $I_{PET,obs}$ stands for the activity values of the acquired image after the PVE, $I_{PET,true}$ is the true radioactivity of the object and I_{PSF} is a PSF kernel. The PSF values are measured by taking a PET image of a point-shaped radioactivity source in air to derive the distribution of the signal in the transaxial and axial directions. The width at the half of the curves height (referred to as FWHM) is used as an estimate of the PSF. Another interpretation of FWHM is that it gives the smallest distance between two resolved points such that they can still be distinguished from each other.

The formula (2-9) cannot be solved with deconvolution methods directly, because of the contribution of the noise. However, several solutions have been proposed for this problem. Methods that are applied to reconstructed images are divided into region-based methods that calculate the corrected mean radioactivity values of certain ROIs and voxel-based correction methods that produce corrected image data. The region-based methods [Labbé et al. 1998, Rousset et al. 1998a] (R-PVC) divides the image into segments, for which the corrected mean values are calculated by solving a system of linear equations. The voxel-based methods by Meltzer et al. [Meltzer et al. 1999], Müller-Gärtner et al. [Müller-Gärtner at al. 1992] and Alfano et al. [Alfano et al. 2004] (M-PVC, MG-PVS and A-PVC) create a simulated image of the activity distribution after the modelled PVE. The image is then used as a divisor for the voxel values of the region to be corrected. The effect of the PVC on the reproducibility of PET imaging has been so far evaluated for the M-PVC and MG-PVC methods. There, the less sophisticated M-PVC appeared to give better results [Slifstein et al. 2001]. In some recent studies deconvolution based iterative reconstruction methods without anatomic information have been proposed [Panin et al. 2006, Alessio et al. 2006, Tohka et al. 2008]. These methods require the knowledge of the local spatial resolution within ~1mm [Soret et al. 2007]. A lot of work is done to incorporate the spatial response function in to the image reconstruction phase [Panin et al. 2006].

2.2.1.1. Region based method (R-PVC)

In the method proposed by Rousset et al. [1998a], the mean radioactivity values I_j (j = 1, …, N) for the selected ROIs are modelled by a set of linear equations

$$\begin{bmatrix} \int_{ROI\,1} \mathrm{RSF}_1(r)\,\boldsymbol{dr}\,,\ldots\,,\int_{ROI\,1} \mathrm{RSF}_N(r)\,\boldsymbol{dr} \\ \int_{ROI\,2} \mathrm{RSF}_1(r)\,\boldsymbol{dr}\,,\ldots\,,\int_{ROI\,2} \mathrm{RSF}_N(r)\,\boldsymbol{dr} \\ \\ \int_{ROI\,N} \mathrm{RSF}_1(r)\,\boldsymbol{dr}\,,\ldots\,,\int_{ROI\,N} \mathrm{RSF}_N(r)\,\boldsymbol{dr} \end{bmatrix} \begin{bmatrix} I_1 \\ I_2 \\ \cdot \\ \cdot \\ \cdot \\ I_N \end{bmatrix} = \begin{bmatrix} I_{PET\,obs,ROI\,1} \\ I_{PET\,obs,ROI\,2} \\ \cdot \\ \cdot \\ \cdot \\ I_{PET\,obs,ROI\,N} \end{bmatrix}$$

$$(2\text{-}10),$$

where $I_{PET\,obs,ROI\,N}$ is the observed mean activity of the N:th ROI. This radioactivity is described as a sum which includes the true mean values of all ROIs multiplied by the radioactivity distribution functions RSF. The distribution functions are defined as ROI binary mask images convoluted by the PSF of a particular tomograph ($X_{ROI,N} \otimes I_{PSF}$). The observed mean radioactivity concentration in the ROIs is therefore obtained as a sum of the contributions of all defined ROIs to the current ROI area. In the above set of equations, all *RSF*s and the observed values are known, which makes it possible to calculate the true mean radioactivity values I_N. Furthermore the values are assumed to be homogenous inside selected ROIs.

2.2.1.2. Voxel based methods (M-PVC, MG-PVC, A-PVC)

The voxel-based methods that are evaluated are based upon a set of assumptions about the PET image. In M-PVC [Meltzer et al. 1999], the observed PET image radioactivity concentration $I_{PET\,obs}$ is formulated as:

$$I_{PET\,obs} = I_{PET\,act,GM+WM} \times (X_{GM+WM} \otimes I_{PSF}) \qquad (2\text{-}11),$$

where X_{GM+WM} refers to a binary mask of the WM and GM segments as determined from an MRI image. The segments are convoluted by the tomograph point spread function I_{PSF}. Finally the true radioactivity concentration at the conjunction of GM and WM regions $I_{PET\,act,GM+WM}$ is multiplied by the convolution mask to produce the observed PET image. In this method, considerable amount of the radioactivity in the observed PET image is assumed to originate only from GM and WM regions. Therefore, the equation can be rewritten as:

$$I_{PET\,act,GM+WM} = I_{PET\,obs,GM+WM} / (X_{GM+WM} \otimes I_{PSF}) \qquad (2\text{-}12),$$

This method produces a PVE corrected image containing the composition of GM and WM, with the assumption that the radioactivity concentration is uniformly distributed in these areas.

When ROIs lie mainly within the GM region, it is possible to apply the correction method to that area, assuming that radioactivity is uniformly distributed in the GM and WM regions and that the mean radioactivity of the WM is known. In MG-PVC, the observed radioactivity distribution $I_{PET,obs}$ is modelled as a sum of the true GM and WM radioactivity distributions:

$$I_{PET\,obs} = I_{PET\,act,GM} \times (X_{GM} \otimes \mathrm{I}_{PSF}) + C_{WM} \times (X_{WM} \otimes \mathrm{I}_{PSF}) \qquad (2\text{-}13),$$

$$I_{PET\,act,GM} = [I_{PET\,obs} - C_{WM} \times (X_{WM} \otimes \mathrm{I}_{PSF})]/(X_{GM} \otimes \mathrm{I}_{PSF}) \qquad (2\text{-}14),$$

where C_{WM} is here the estimated mean of the WM radioactivity concentration, X_{WM} and X_{GM} are binary masks of the WM and GM segments acquired from the corresponding MRI image and I_{PSF} is the tomograph PSF. In this method, the correction specialises to the GM area and the corrected mean WM radioactivity concentration is used as a starting point for the algorithm.

The A-PVC method [Alfano et al. 2004] models the observed intensity $\mathrm{I}_{PET\,obs}$ (p) of point p by the formula:

$$I_{PET\,obs}(p) = \int_{volume} C(s) \times g(p,s)\, ds + noise \qquad (2\text{-}15).$$

The integration is performed over the affecting region (volume) to p; $C(s)$ is the true radioactivity concentration at point s and $g(p,s)$ is the probability that s contributes to the radioactivity of p. Here $g(p,s)$ can be acquired from the tomograph PSF as M-PVC and MG-PVC. For points in the GM area, the formula becomes:

$$I_{PET\,act,GM}(p) = \int_{volume} I_{PET\,obs,GM}(s) \times g'(p,s)\, ds + noise \qquad (2\text{-}16),$$

where:

$$g'(p,s) = X_{GM}(s) \times g(p,s) \, / \int_{volume} X_{GM}(s) \times g(p,s)\, ds \qquad (2\text{-}17),$$

which gives the probability that the activity at point p originates from point s. In (2-16) the observed GM radioactivity is obtained by first subtracting WM radioactivity from the PET image as in MG-PVC. An essential difference from MG-PVC is that the corrected value from the affecting region (see 2-16 and 2-17) and not only from a single point as in MG-PVC (see 2-17).

2.2.1.3. Summary of correction methods

The above mentioned assumptions made for the correction methods should approximately correct for obtaining reliable results inside the GM and WM regions in real applications. Inhomogeneities inside the GM and WM mean that PVE exists also inside them. This does not affect the mean radioactivity concentration, but it changes the values for smaller ROIs inside them. The A-PVC method can be seen as a compromise between region-based and voxel-based methods; and it is assumed to be more accurate than the other voxel-based methods reviewed here, but it is still based upon the same assumptions about the PET images.

2.2.1.4. Principles of WM estimation

The mean activity concentration of the WM affects the MG-PVC and A-PVC methods, and therefore it should be estimated as well as possible. An increase in the WM mean value produces decreased values of the PVE-corrected radioactivity concentrations. In the central slices (CS) method for WM estimation, some transaxial slices from the central area of the brain are selected and the WM segments are then eroded in slices to identify the part of the WM region that is not affected by spillover from the GM. Another way of

doing the estimation is to use the method of Rousset et al. (R-WME) [1998] to calculate the PVE corrected mean activity of the WM. Third, in the method proposed by Alfano et al. [2004] (A-WME), an image calculated from convoluted mask images with the formula $(X_{GM} \otimes I_{PSF})/((X_{GM} \otimes I_{PSF})+(X_{WM} \otimes I_{PSF})$ is used. In the locations where the values of the image are high, the PET radioactivity values contain little of the true radioactivity from the WM region. Conversely, low values in the image indicate that PET radioactivity values in these locations consist mainly of the true radioactivity from the WM region. In A-WME, the PET radioactivity values are projected against the convoluted mask image. A regression line is then fitted to characterise PET radioactivity values and the probabilities that the radioactivity value originates from the WM region. Finally, the WM estimation is made from an interception of this line.

2.3. Gating (for motion correction during a PET study)

PET images are acquired over time periods (time frames) that can vary from a few seconds to tens of minutes. To follow-up tracer kinetics typically several time-periods are combined to form a dynamic study. E.g. in a whole body study a single period of time per bed position is around 1-3 minutes, in studies of the abdomen or heart from a few seconds to 20 minutes. In dynamic studies of the brain the whole scan can last up to 90 minutes consisting of 20-30 separate time frames. Therefore, it is obvious that during such time periods various motions may have significant effects on the PET images. Typically all attempts are done to avoid involuntary motion of the study subject inside the gantry. However, physiological motion due to respiration and cardiac contraction is not a negligible source of error.

The extent of motion depends upon different factors such as organ location, patient height and weight, anatomical and physiological circumstances etc. [Dawood et al. 2006]. In a study with MR it was found that the diaphragm moves about 15-20 mm due to respiration [Schwartz et al. 2000]. Due to this in 30% of lung tumours the motion was in the range of 6-23 mm depending upon the location of the tumour. Respiratory induced motion of heart and coronaries has been reported to be mostly in cranial-caudal direction [Wang et al. 1995, Danias et al. 1999, Livieratos et al. 2006, Martinez-Möller et al. 2007] and the displacement is between 4.8 and 13.1 mm. Contraction activity of heart has been reported to induce 13 mm epi- and endocardial motion [Slomka et al. 2004] and 9 mm superior-inferior motion for left coronary artery [Wang et al. 1999]. So it is obvious that both respiratory and contraction induced heart motions have major effect on PET imaging of cardiac and thoracic regions.

When the motion can be regarded as periodic during investigation it can be corrected with gating. An unfortunate side-effect of the gating is that the statistical quality of each gated image suffers as the total number of PET events is distributed over a number of different images [Klein et al. 1997].
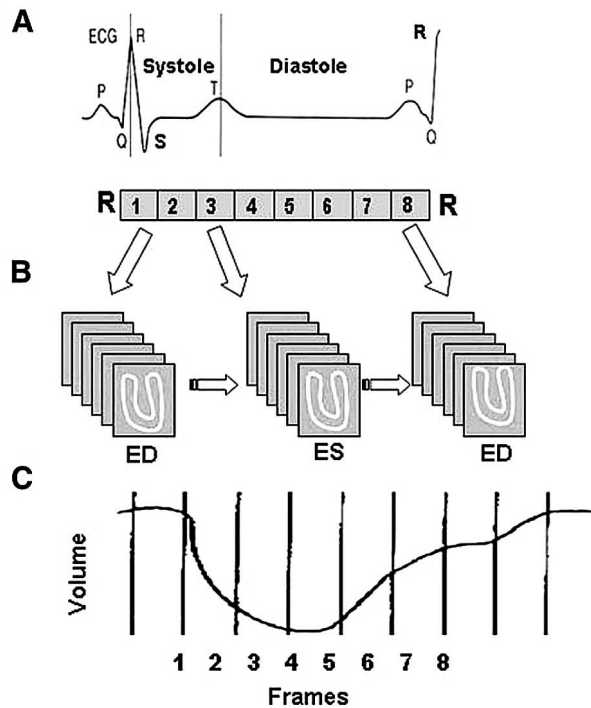
Figure 2-11. Principle of ECG-gated acquisition. R–R interval on ECG, representing 1 cardiac cycle, is typically divided into 8 frames of equal duration (A). Image data from each frame are acquired over multiple cardiac cycles and stored separately in specific locations ("bin") of computer memory (B). When all data in a bin are added together, image represents a specific phase of cardiac cycle. Typically, a volume curve is obtained, which represents endocardial volume for each of 8 frames (C). ED is end-diastole and ES is end-systole [Paul et al. 2004].

Cardiac gating has been used in conventional nuclear medicine already for decades. More recently, respiratory gating has been used to correct for the breathing motion e.g. when looking for presence of small lung nodules in patient with cancer. This has become feasible because of improved resolution and sensitivity. Generally, gating requires a special apparatus to detect the motion and also a mean to transfer the knowledge of the motion to the imaging device. This is normally done by measuring a physiological function of the subject and transferring trigger pulses from a certain phase of the physiological signal. The most common way to do this is ECG monitoring and triggering from each QRS complex (Fig 2-11) [Paul et al.2004].

Attenuation correction with ^{68}Ge/^{68}Ga or ^{137}Cs transmission sources require up to 20 min acquisition time in thoracic region. This had to be done with free breathing and thus it was automatically averaged together with the PET emission data which is also done during free breathing.

For new PET/CT devices it takes only a few seconds with 16-slice or 64-slice CT to obtain the attenuation map measurement. Furthermore it is possible to gate also the transmission scan to obtain gated attenuation correction maps [Kinahan et al. 1998, Burger et al. 2002 and Nakamoto et al. 2002]. The major drawback with the gatedCT

(cineCT) is the increased dose and therefore CT is normally performed in breath-hold and without gating. This however leads to misregistration between CT and PET data [Chin et al. 2000, Erdi et al. 2004]. There are some recent studies aiming to reduce the dose using lower CT tube current and averaging the cine data [Pan et al. 2006] to overcome the dose problem and justify gated AC or deep inspiration breath-hold for both PET and CT [Nehmeh et al. 2007].

In the present PET/CT devices the gating system is a standard option and it is also possible to choose the function to be gated. In oncological studies respiratory gating is important in thoracic region but also in cardiac studies it may play an essential role.

2.3.1. Cardiac gating

Myocardial perfusion PET imaging is accomplished using short-lived flow tracers such as Oxygen-15 labelled water (T½=123 s), Nitrogen-13 labelled ammonia (T½=10 min) or Rubidium-82 (T½=75s). The short half life makes it possible to study perfusion at rest and during pharmacological stress [Bacharach et al. 2003, Schelbert et al. 2003]. Diagnostic errors due to misregistration of CT attenuation and emission PET in cardiac PET has also been reported [Gould et al. 2007].
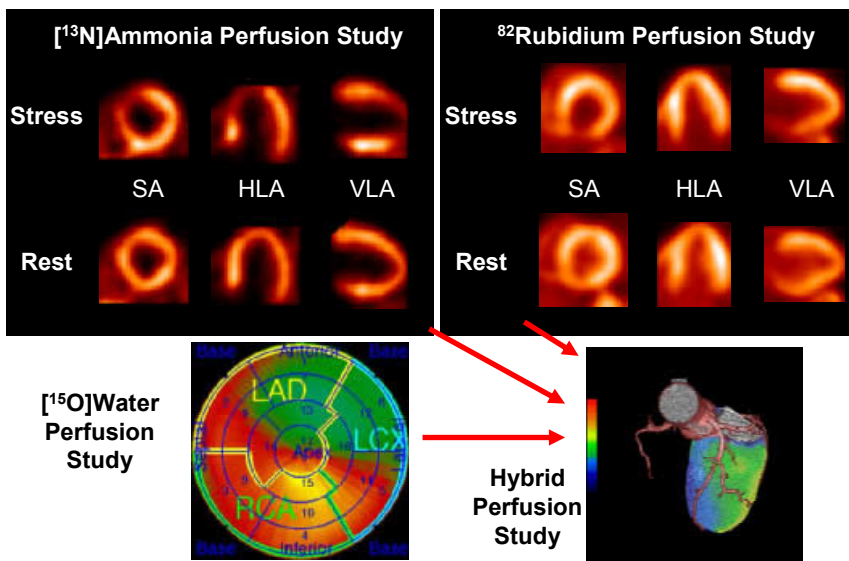

Figure 2-12. Fusion software for integrated analysis of PET and CTA. Representative short- (SA) and horizontal and vertical long-axis (HLA and VLA) slices in different patients, using nitrogen-13 ammonia (top left) and rubidium-82 (top right) tracers. Bulls-eye representation of oxugen-15 water study (bottom left) and a hybrid perfusion representation of one prfusion study [Courtecy of Turku PET Centre].

The list mode (LM) data recording of the new PET/CT systems allows for simultaneous creation of static images for qualitative perfusion analysis, dynamic data sets for kinetic modelling and gated data sets for analysis of left ventricular function (Fig. 2-13) [Bengel et al. 2008]. When performing CT coronary angiography (CTA)

and PET perfusion it is possible also to combine the two image sets for more comprehensive analysis.
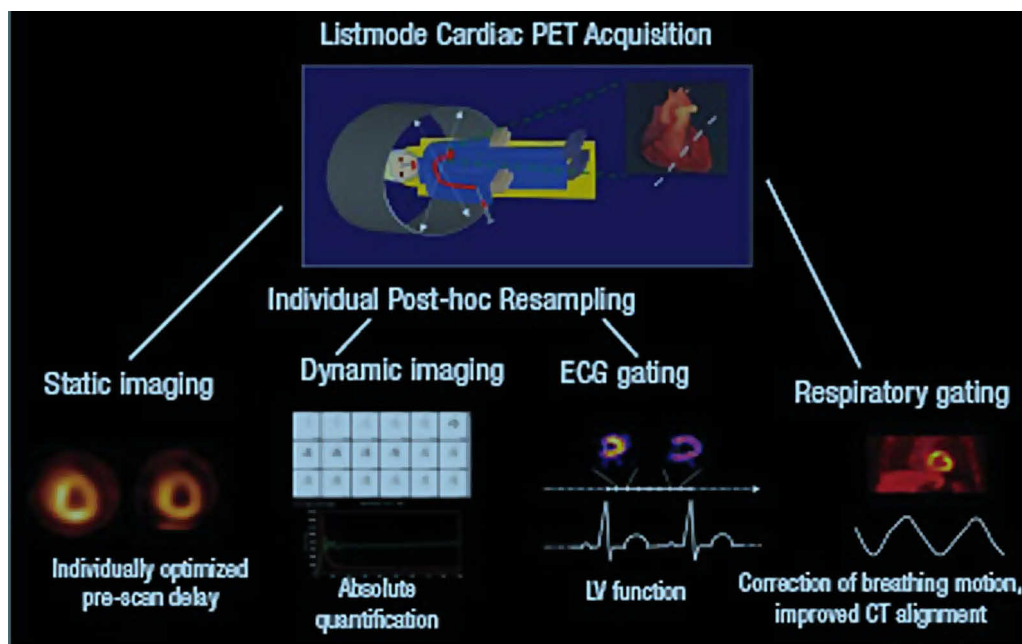
Figure 2-13. A schematic illustration of different image resampling options after cardiac PET data acquired in list mode [Bengel et al. 2008].

2.3.2. Respiratory gating

The large respiratory motion leads to two sources of artefacts, wrong attenuation correction and image blurring. As the CT images used for attenuation correction (CTAC) are acquired in seconds and mostly with the breath hold technique, they represent a snapshot of the breathing cycle in contrast to the PET which is acquired over several minutes. Therefore a part of the PET data will be wrongly attenuated as activity from the heart is attenuated with the lung density. The effect of this in the diaphragmatic area is nicely demonstrated in Figure 2-14 [Visvikis et al. 2006]. One way to overcome this is to perform CTAC with a low dose average CT technique [Pan et al. 2006]. A comprehensive review of current respiratory motion compensation techniques in PET imaging for oncology applications is found in Visvikis et al. [2006]. One essential element in order to be able to synchronize the emission acquisition with the respiratory motion is the ability to measure the respiratory motion. The studies carried out to date have investigated a large number of different respiration monitoring systems, including a transducer or an impedance ECG monitor measuring changes in abdominal or thoracic circumference [Nehmeh et al. 2003], a thermistor measuring the temperature of circulating air during patient respiration [Boucher a al. 2004], a spirometer measuring respiratory flow [Guivarc'h et al. 2004], Varian Real Time position management (RPM, Varian Medical Systems, Palo Alto, CA) [Nehmeh et al. 2002b], or the Polaris system tracking the displacement of infrared reflective markers in the patient chest (NDI, Canada).
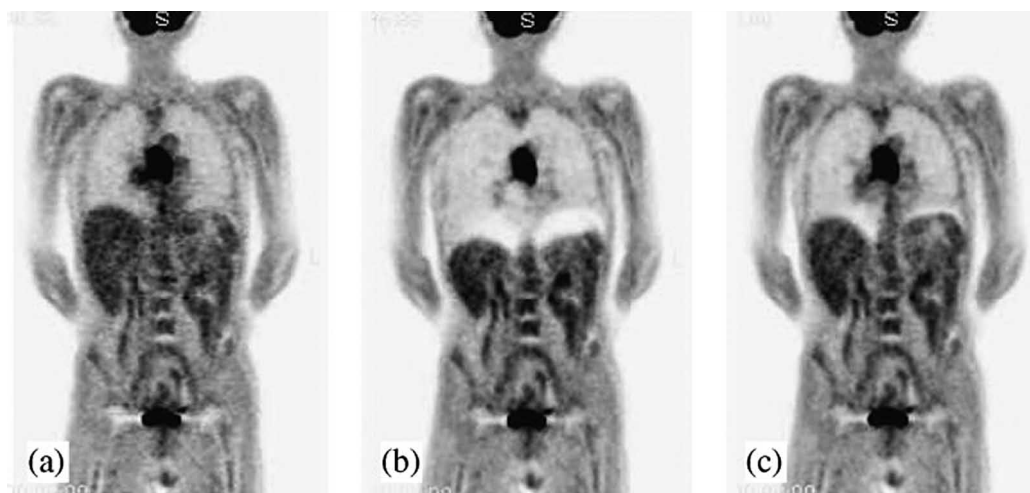
Figure. 2-14. Whole body PET images demonstrating artifacts at the level of the diaphragm as a result of respiratory motion differences between emission and transmission maps used for attenuation correction; use of (a) 68Ge/68Ga rod sources, (b) CT acquired at breath-hold (end inspiration),(c) CT acquired at breath-hold (end expiration) [Visvikis et al. 2006].

With the exception of the spirometer and the thermistor, the majority of these systems provide a respiratory signal through the measurement of the displacement at a particular zone of the thoracic cage. Despite the proposition and evaluation of different detector systems, the majority of them lead to reasonable accurate and reproducible respiratory signal [Guivarc'h et al 2004]. Although it could be argued that the spirometer reflects the lung movement better due to respiratory motion, it has been generally less well tolerated by patients than the other systems considering the long duration of the emission acquisitions.

Respiratory motion reduces image quality also by reducing the target-to-background ratio (contrast), resulting in image blurring. It results also in overestimation of the lesion size. The consequence of these effects is a possible misidentification of the lesion. The number of counts acquired during a time t, whether the lesion is static or moving is the same. Therefore, any increase in the apparent lesion size due to motion will decrease the activity concentration per pixel within the lesion [Nehmeh et al. 2002a], thereby reducing the lesion contrast. Consequently, the measured SUVs will underestimate the tracer uptake within the tumours. Measurements of the lesions' volumes in the gated mode showed a reduction of up to 34% compared with that of the nongated measurement. This reduction in the lesion volume has been accompanied by an increase in the intensity in the ^{18}F-FDG signal per voxel [Nehmeh et al 2002b]. Several methods for correcting the lung tumour blurring have been introduced based either using affine transformation of list mode data [Lamare et al. 2007] or sorting of the image data [Wang et al. 2007].

2.3.3. Dual gating

The need for a dual gating technique in cardiac PET imaging was first asserted in an article by Ter-Pogossian and al.[1982]. Their study on dogs indicates that the true

tracer distribution was significantly degraded in cardiac PET imaging by both intrinsic cardiac and respiratory motions. However, the feasibility of the dual gating technique was first demonstrated by Klein al. [Klein et al 1997, Klein et al. 1998]. Dual gating protocol was introduced for online histogramming of PET data with the help of signal processing software. Real-time dual gating method utilizes prospectively constant gate lengths which cannot be modified retrospectively. The method is vulnerable for heart and respiratory rate irregularities which makes it inappropriate to many patient studies. Simultaneous cardiac and respiratory gating was with microPET II small animal scanner on mice was tested by Yang et al [2005]. They did not see any contraction motion and also the respiratory motion was less than 1 mm and they stated that correction for it might not be necessary on mice. Martinez-Möller et al. [2007] reported that it is feasible to carry out dual gated cardiac PET studies using LM acquisition with ^{13}N-ammonia and ^{18}F-FDG. They used pressure sensor respiratory gating device (Anzai Medical Co., Tokyo, Japan), with additional signal processing to determine respiratory gates with fixed gate duration. Respiratory gating with equitemporal length and constant statistics was reported to be more suitable than intensity-based gating algorithm. ECG gating was done by dividing each ECG cycle to *n* frames of the same duration. Finally "diastolic gates" were summed together. Average respiratory motion was reported to be 4.8 mm in cranial-caudal direction between inspiration and expiration in diastolic images. Motion induced by heart contraction was not reported in the work by Martinez-Möller et al. Also Lang et al [2006] have reported that image quality can be enhanced using double gated list-mode acquisition. The fast non gated CT introduced artefacts in moving organs in their study and give errors in quantification. Description of how the quantification was handled in the studies of Martinez-Möller et al [2007] or Lang [2006] was not described.

3. THE PURPOSE AND AIM OF THE STUDY

1. To investigate the physical performance of a new whole body PET/CT scanner with NEMA standard (I).

2. To compare methods for partial volume correction in PET studies of the brain (II).

3. To develop and test a new robust method for dual cardiac-respiratory gated PET (III-IV).

4. METHODS

4.1. Physical Performance of DVCT PET/CT scanner (I)

4.1.1. The scanner

Physical performance was measured with a new Discovery VCT (VCT) scanner (General Electric Medical Systems, Milwaukee, WI, USA). The VCT combines a helical multislice CT scanner and a newly designed BGO (Bishmut Germanate Oxide) block PET tomograph with a large 70 cm patient port. In STE the CT scanner has 16 slices covering 20 mm with a thinner slice thickness of 1.25 mm. The VCT covers 40 mm with a thinner slice thickness of 0.625 mm. The CT technical characteristics of the Discovery VCT are given in Table 4-1.

Table 4-1. CT characteristics of the Discovery VCT

Scan mode	Helical, axial, scout
Aperture (cm)	70
Transverse scan field of view(cm)	25 for adult head; 25, 50 for the body
Maximum CTAC field of view (cm)	70
Maximum number of CT slices	64
Nominal slice thickness (mm)	*0.626, 1.25, 2.50, 3.75, 5, 7.5, 10.0*
Tube voltage (kV)	80, 100, 120, 140
Tube current (mA)	10 to 800, 5 mA increments
Detector material	(Y,Gd) ^{203}Eu ceramic
Number of detectors	*21288*
Number of detectors per row	888
Total effective length of rotator array (mm)	20
Maximum cradle travel (mm)	2000
Rotation time (s)	0.35, 0.375, 0.4, 0.425, 0.45, 0.475, 0.5, 0.6, 0.7, 0.8, 0.9, 1.0, 2.0
Pitch factor	*0.5625:1, 0.9375:1, 1.375:1, 1.75:1*
Maximum single acquisition scan time	60 s
Maximum multiple acquisition scan time	*2881 s*
Heat capacity	Anode: 8.0 MHU Housing: 3.2 MHU
Maximum power (kW)	100.2

The PET scanner in both systems is a multi-ring BGO block detector system. The newly designed BGO crystals are arranged in 24 rings. Axial (6.3 mm) and radial (30 mm) crystal dimensions have remained the same as in the Discovery ST (ST) model [Bettinardi et al. 2004; Mawlawi et al. 2004], while the transaxial dimension has been reduced from 6.3 mm to 4.7 mm. The result of this is better plane sampling. This new design increases the number of crystals from 10 080 to 13 440. In addition to the new crystal design the front end electronics and reconstruction algorithms have been renewed as compared to ST. This enables the change of energy window in 3D mode from (375–650) keV to (425-650) keV. Also, a shorter coincidence time window of 9.3 ns is possible for 3D mode acquisition. Technical specifications for PET are shown in

Table 4-2. GE has also developed a LYSO crystal-based PET scanner GE Discovery RX (RX) [Kemp et al. 2006] which has a crystal dimension of 4.2 x 6.3 x 30 mm^3, a coincidence window of 6.5 ns, and an energy window of (425-650) keV. The new crystal material results in better count rate capabilities.

Table 4-2. PET characteristics of the Discovery STE and the Discovery VCT

Detector ring diameter (cm)	88.6
Patient port and transaxial FOV (cm)	70
Axial FOV (cm)	15.7
Number of individual crystals	13440
Number of crystals per ring	560
Number of rings	24
Number of image planes	47
Crystal size (mm)	4.7 transaxial, 6.3 axial, 30 radial
Crystal array per block	8 x 6
Number of detector blocks	280
Axial sampling interval (mm)	3.27
Coincidence window width (ns)	2D – 11.7 3D – 9.3
Lower energy threshold (keV)	2D – 375 3D – 425
Maximum axial coverage (cm)	160

4.1.2. Performance measurements

The NEMA NU 2-2001 standard was chosen to be used for most of the measurements as it has been developed for whole body tomographs.

Spatial resolution

Spatial resolution was measured with ^{18}F point sources made by capillary tubes with inner diameters of 1.0 mm. Point sources were positioned as described in 2.1.1 (NU 2-2001 resolution)

Axial resolution in 2D was also tested according to the NEMA NU 2-1994 standard as this measure has better axial sampling than the corresponding the NEMA NU 2-2001. According to this standard axial resolution is determined by forming a one-dimensional point source response function along profiles through the volume image in the axial direction, through the peak of the distribution in the slice nearest to the source. The ^{18}F point source was moved stepwise across the FOV starting axially 2.15 mm before the beginning of the axial FOV and stopping 2.15 mm after the end of the axial FOV. The step was 0.5 mm and acquisition time 2 seconds per step. In the NEMA NU 2-1994 standard, it is recommended that the step should be close to one-tenth of the expected FWHM.

Scatter fraction, count rate and randoms test

A line source (LS) with ID of 2.3 mm was prepared by accurately filling the 70 cm long part of the line with about 2500 MBq or 900 MBq of ^{18}F water solutions for 2D and 3D scans, respectively. The LS was inserted into a hole parallel to the long axis but radially 4.5 cm off centre of the 20 cm diameter solid polyethylene cylinder phantom

METHODS

with an overall length of 70 cm. In both scans the centre of the phantom was positioned at x=0 cm and y=0 cm and axially in the centre of the scanner FOV. Radioactivity concentration was calculated by dividing the radioactivity in the LS with the total volume (22 litres) of the phantom.

Acquisition protocol in scatter fraction and count rate tests for the 2D and 3D modes are almost identical. For the 2D mode, 4 consecutive 15 minute frames were followed by 14 frames of 25 minutes with a time delay of 25 minutes between each frame. The total exposure time is 12 hours 15 minutes. In the 3D study, 8 consecutive 15 minute frames were followed by 14 frames of 25 minutes with a time delay of 25 minutes between each frame with a total acquisition time of 13 hours 15 minutes.

Scatter fraction and count rate test analysis is performed in 2D on the uncorrected data sinograms, while in 3D, sinograms were rebinned with single slice-rebinning method before analysis. The GE software package prints results of radioactivity concentration, true, prompt and random count rates, as well as the noise equivalent count rate (NEC rate). Data are plotted against the radioactivity concentration and peak rates are recorded. System scatter fraction was calculated with GE software as the ratio between scatter component and total events at a low radioactivity level, where count loss rate and random count rate are negligible.

Accuracy of count losses and randoms corrections

The accuracy of count losses and randoms corrections is measured by comparing the trues rate calculated using count losses and randoms corrections with trues rate extrapolated from measurements with negligible count losses and randoms.

Sensitivity

The NEMA NU 2-2001 Sensitivity phantom (Data Spectrum Corp., NC, USA) was used for measuring the sensitivity. A 70 cm polyethylene line source with the inner diameter (ID) of 1 mm and an outer diameter (OD) of 3 mm was filled with a radioactivity concentration of 1.7 MBq/ml of ^{18}F. Five surrounding aluminium sleeves (or tubes) were used as known absorbers to attenuate positrons and create photons during measurements. The diameters of the sleeves are:

- 1st sleeve: ID 3.9 mm, OD 6.4 mm

- 2nd sleeve: ID 7.0 mm, OD 9.5 mm

- 3rd sleeve: ID 10.2 mm, OD 12.7 mm

- 4th sleeve: ID 13.4 mm, OD 15.9 mm

- 5th sleeve: ID 16.6 mm, OD 19.1 mm

Sensitivity measurement consists of five acquisitions where one sleeve at a time was added around the source, so that in the last acquisition all five sleeves were present. Two sets of scans were performed in the centre along the z-axis (R0) and 10 cm radially off-centre from the z-axis (R10). Sensitivity in 2D mode and 3D mode was measured in both locations. Scanning time for each absorber was 60 sec. Sensitivity Analysis was performed based on the method introduced by Bailey et al. [1991b].

Whole body image quality test

The main purpose of the image quality test is to simulate the PET performance during a standard whole body acquisition protocol. A body-shaped phantom as described in IEC 61675-1 PET performance standard and the 70 cm long cylinder phantom used for scatter fraction and count rate in NEMA NU-2 2001 were used to simulate a patient. Inside the body-shaped cylinder, the IEC phantom has six fillable spheres with diameters of 10, 13, 17, 22, 28 and 37 mm, and one central cylinder with diameter of 50 mm, filled with low atomic number material to simulate the lungs. The body volume (as background) and the four smallest spheres (as lesions) were filled with a ^{18}F solution, while two of the largest spheres were filled with water that remained non-radioactive. The SF & CR line source (volume = 5.6 ml) in 70 cm long cylinder phantom was filled with a radioactivity of 200 MBq to simulate the rest of the body radioactivity outside the scanner FOV.

The image quality test was performed with different lesion to background (L/B) ratios. In the first 2D measurement the radioactivity concentration in the hot spheres was 21.0 kBq/ml and in the background 2.6 kBq/ml to stimulate a lesion to background ratio (L/B) of 8/1. Corresponding values for 3D measurements were 17.7 kBq/ml in hot spheres and 2.4 kBq/ml in the background. In the second measurement, the decay of radioactivity in hot spheres was considered and the radioactivity concentration of the background was increased to 4.6 kBq/ml in order to obtain a (L/B) ratio of 4/1 for both 2D and 3D mode acquisitions.

The image quality test includes a CT-based attenuation correction. For both (L/B) ratios six interleaved (2D and 3D) acquisition frames were performed. The frame length for 2D was 8 min 20 s and for 3D 7 min 19 s as proposed by the manufacturer to simulate a 100 cm axial whole body study.

An ML-OSEM reconstruction with two iterations and 20 subsets was used for the 2D data and a full 3D ML-OSEM reconstruction (16) with two iterations and 28 subsets for the 3D data. Reconstruction matrix is 128x128 resulting in a pixel size of 5.47 mm. Although this is our clinical setting, further analysis with four iterations and a 256x256 matrix were reconstructed from the same measurements.

To evaluate the contrast, circular regions of interest (ROIs) with a diameter equal to each sphere size and the inter-lung cylinder were positioned on the PET image plane where the spheres were located. Twelve ROIs 37 mm in diameter were drawn on the background area. From these ROI values, the following parameters proposed by the NEMA NU-2 standard were calculated:

1.   The hot sphere contrast recovery coefficient (HRC)

$$\text{HRC} = \frac{\left(C_{hot} \middle/ C_{bg} - 1 \right)}{\left(a_{hot} \middle/ a_{bg} - 1 \right)} \qquad (4\text{-}1),$$

where C_{hot} and C_{bg} are the average counts measured in hot sphere ROIs and background ROIs, while a_{hot}/a_{bg} is the radioactivity ratio in hot spheres and in the background, equal to the L/B ratio.

2.   The cold sphere contrast (CRC)

$$\text{CRC} = 1 - \left(\frac{C_{cold}}{C_{bg}} \right) \quad\quad (4\text{-}2),$$

where = C_{cold} is the average counts measured in the cold sphere ROIs.

3.   The accuracy of attenuation and scatter correction as the residual error (%) in the lung region

$$\text{AC}_{lung} = 100 \left(\frac{C_{lung}}{C_{bg}} \right) \quad\quad (4\text{-}3),$$

where C_{lung} is the average counts measured in the lung insert ROI.

4.   The background % variability

$$\text{BV}_j = 100 \left(\frac{SD_j}{C_{bgj}} \right) \qu\quad (4\text{-}4),$$

where SD_j is the standard deviation of the background ROI counts for sphere j.

4.2. PVC (II)

In the present study, testing with a phantom object was done using three different tomographs to reveal differences in the noise amplification between the PVC methods proposed by Alfano et al. [2004], Rousset et al. [1998a], Müller-Gärtner et al. [1992], and Meltzer et al. [1984]. In total, eight methods were evaluated as three different WM radioactivity estimation methods proposed by Alfano et al., Rousset et al. and Müller-Gärtner et al. were combined with the methods by Alfano et al. and Müller-Gärtner et al. In addition, the binding potential [Mintun et al. 1984] values with eight patients scanned on two separate occasions with the dopamine D2 receptor ligand [11C]raclopride were analyzed with four of the methods in order to reveal the reproducibility and reliability characteristics of the evaluated PVC methods. Real differences between scans are assumed to be minimal in this test-retest material.

4.2.1. Instrumentation

The GE Advance (GE, Milwaukee, WI), PET/CT (DSTE, GE, Millwaukee, WI) and HRRT (CPS Inc, Knoxville, TN) PET tomographs were used for the phantom tests. All three tomographs were operated in the 3D acquisition mode and the images reconstructed with the iterative reconstruction method (OSEM or its variant). All data were dead-time, decay, scatter and attenuation corrected with scanner-specific procedures. The PET input images for the test-retest tests were scanned with the GE Advance PET tomograph. The corresponding FWHM values in the transaxial and axial directions were 5.0mm and 6.5mm for the GE Advance, 5.0mm and 5.8mm for the

PET/CT, and 2.5mm and 2.5mm for the HRRT tomograph. All FWHM values were acquired according to the Nema NU 2-2001 standard [National elec. 2001]. Although FWHM degrades when moving out from the centre of the field view, in this work it was assumed that the PSF is constant. This comes at the expense of accuracy loss, but saves computation resources [Assie et al. 2004]. The same approach is used for all PVC methods under evaluation and, therefore, it is not expected to cause bias in any of the methods. All scanners were cross-calibrated with a dose calibrator (VDC-404, Veenstra Instrumenten, The Netherlands).

4.2.2. Phantom data

The accuracy of the quantification was tested using a Hoffman brain phantom (model JB003) that resembles a human brain with respect to the distribution of volumes identified as WM, GM and cerebrospinal fluid (CSF). The phantom was filled with ^{18}F-labelled FDG liquid to follow the 4:1 relation between the GM and WM activities. Image dimensions for the GE Advance, PET-CT and HRRT PET tomographs were 256x256x35, 256x256x47 and 256x256x207 voxels, respectively. The use of CT from the PET/CT instead of MR for segmentation was not expected to produce differences in results for these phantom studies The resulting CT segment images were already in alignment with the PET/CT PET image, so it was only necessary to reslice them into the PET image voxel dimensions to give a structural definition of the WM and GM regions. The phantom images of the GE Advance and HRRT tomographs were coregistered to the PET/CT orientation in order to preserve the segmentation accuracy, which has been reported to be one of the main error factors in PVC with the methods under evaluation [Quarantelli et al. 2004].

4.2.3. Test-retest data

To assess the impact of different PVC approaches on the radioactivity estimates and reproducibility and reliability of [^{11}C]raclopride binding in the human brain, we re-analyzed a previously published dataset [Hirvonen et al. 2003]. In brief, eight healthy volunteers had undergone two successive scans with a GE Advance PET tomograph during the same day, at least two hours apart. All subjects had also undergone 1.5 T MR imaging. The image dimensions were 128x128x35 voxels for the PET and 256x256x100 voxels for the MRI. Voxel sizes for the PET and the MRI were 2.34x2.34x4.25mm and 1.09x1.09x1.00mm, respectively. The MR images were segmented by using the SPM2 software package [SPM2] which uses a priori probability maps of the GM and WM regions in order to assign voxels in brain space to these segments. The PET images were realigned with SPM2 routines. The ROIs were manually delineated on MR images co-registered to summated PET images using the normalized mutual information method as implemented in SPM2. ROIs were drawn on axial slices on caudate, putamen, lateral and medial thalamus, and the cerebellum. All ROIs were created using the Imadeus software (version 1.2., Forima Inc., Turku, Finland). The Simplified Reference Tissue Model (SRTM) [Lammertsma et al. 1996] using the cerebellum as a reference region was applied to the regional time-radioactivity curves to yield binding potential (BP) values in the ROIs, indicating the capacities of receptors to bind the used ligand [^{11}C]raclopride. The cerebellum

reference region was delineated on an area that was defined as the GM region. Test-retest reproducibility and reliability of the BP values were assessed using test-retest variability (VAR) and intra- class correlation coefficients

$$VAR = \frac{|\, BP_2 - BP_1 \,|}{0.5 \,|\, BP_1 + BP_2 \,|} \qquad (4\text{-}5),$$

where BP_1 and BP_2 refer to BP values of ROI in test and retest scans, and

$$ICC = (BSMS - WSMS) / (BSMS + (n\text{-}1) \times WSMS) \qquad (4\text{-}6),$$

where BSMS is the between-subject mean square of the BP values, WSMS is the within-subject mean square, and n is the number of repeated observations (in this case, $n = 2$). ICC values can range between -1 and 1; values close to 1 indicate that most variance is due to between-subject rather than within-subject variation (good reliability), whereas values below zero imply greater within-subject than between-subject variation (poor reliability).

The mean BP values between test-retest data over eight subjects were compared with t-test ($p < 0.05$, $df = 7$) with non-corrected data and with each of the four evaluated PVC methods. Also, the mean BP values over all 16 studies and the mean variability over eight subjects with non-corrected data were tested to the corresponding values of the four PVC approaches with t-test ($p < 0.05$, $df = 15$ and $p < 0.05$, $df = 7$ respectively). All the t-tests were paired and the t-values were compared to two-tailed t-distribution critical values.

4.2.4. Partial volume correction

Partial volume correction software PVEOut (http://pveout.area.na.cnr.it) was used for the method evaluation. The system incorporates the methods, M-PVC, MG-PVC, R-PVC and A-PVC. The MG-PVC and A-PVC methods utilize WM mean value estimation with the A-WME, R-WME or CS method. As a result, eight PVC methods were available. All the methods were evaluated with a phantom study. The FWHM specified in section 4.2.1 was used for tomograph-specific PSF information in PVEOut. No brain regions other than the GM and WM were assumed to contribute to the radioactivity distribution. The PSF values used with the test-retest data were the same as those used in the phantom study. The PVC process for phantom and test-retest data were all run as batch processes, which required no user interaction after setting the PSF values and input images.   The MG-PVC and A- PVC methods apply correction only to the GM region, setting other voxel values to zero. Therefore, voxels outside the GM region were removed from the test-retest ROIs to make the results comparable with each other.

4.3. Dual gating (III, IV)

4.3.1 Method

All dual-gated cardiac PET scans were performed using the GE Discovery VCT PET/CT scanner (General Electric Medical Systems, Milwaukee, USA). This scanner

has the capacity to acquire data in addition to normal sinograms on a separate disk as a List Mode (LM) file. In LM every event occurring during the acquisition is written in a chronological manner. The scanner was upgraded with a research package in order to accept and process two separate trigger signals in the LM stream. The LM file contains different information, such as time markers, coincidence events, ring position and trigger events. All these events are coded in 32-bit words. The time markers are written every millisecond and the trigger events from the respiratory gating device and the ECG monitor are differentiated by a 7 bit tag at the end of the 32-bit words in the LM file. The LM file enables the rearranging and post-processing of the acquired data according to collected trigger signals. This is done according to a special workflow developed and show in Figure 4-1.
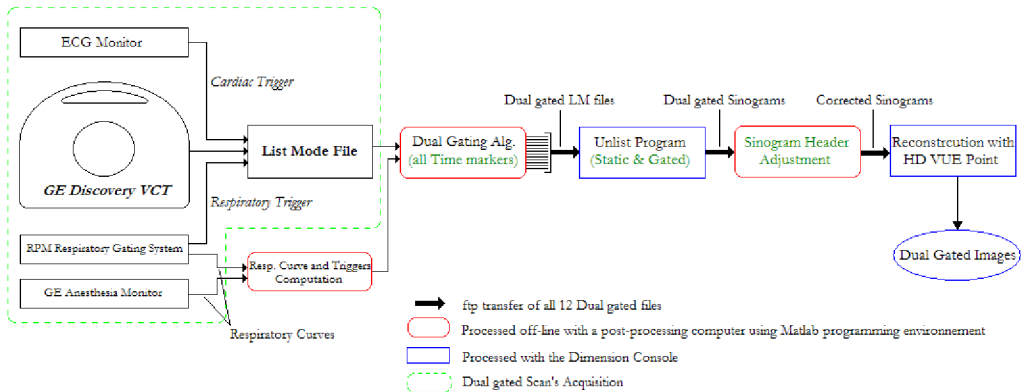
Figure 4-1. Schema of the dual gating workflow.

The ECG monitoring was performed with a standard monitor (IVY Biomedical Systems). This ECG monitor generated a trigger event at every R-peak of the ECG cycle that is directly sent to the PET/CT scanner. The respiratory triggers are generated by the Real-Time Position Management (RPM) Respiratory gating System (Varian Medical Systems, USA). This respiratory gating device is designed to save the respiratory curve with a sampling frequency of 40 ms, and to generate a trigger event every time the patient inspiration turns to expiration. To follow the respiratory cycle, the RPM device uses a charge-coupled device (CCD) camera that tracks the vertical displacement of a pair of reflective markers fixed on the patient's abdomen or chest. The respiratory curve is saved in a separate log file.

Once the acquisition is completed, the LM file and the respiratory curves are sent via the hospital network to a post processing computer where the separation of the different dual gates is processed (see 4.3.1.1).

After processing, the data into dual gates the data is transferred back to the scanner database and replayed to sinograms with an unlisting programme. Before reconstruction, an additional step for adjusting the sinogram header information is needed before final reconstruction (see 4.3.1.2).

Both processes, the dual gating algorithm and the header correction, were designed by our group and carried out off-line.

4.3.1.1. The dual gating algorithm

An algorithm for processing the dual-gated LM data was implemented using the MatLab programming environment (Mathworks, INC) assuming the following requirements:

1. The motion of the heart consists of a respiratory motion and an electrically induced cardiac contraction.

2. Two independent trigger signals are sent to the LM data at every upper-most position of respiratory motion and at every R-peak of the ECG cycle.

3. Amplitude information on respiratory motion is available together with timing of trigger events.

4. Respiratory motion is relatively stable and the amplitude baseline does not vary significantly.

5. If heart rate varies, then the diastolic phase varies accordingly, and the systolic phase remains unchanged when studied at rest.

The programmed algorithm handles the LM data so that it reads every 32 bits of the LM data sequentially and finds different trigger events according to their identifiers. With the help of identifiers, the algorithm labels the periods of two independent motions with a 1-ms time resolution.

In heart studies, the algorithm utilizes the collected respiration amplitude information to determine the time labels for respiratory phases with 40-ms time resolution. We chose at this point to divide the cardiac motion into four (Fig. 4-2, part 3) and the respiratory motion into three separate amplitude phases: expiration, middle, and inspiration. The amplitude thresholds for respiratory phases are adjustable. Thresholds are calculated from the averaged maximum amplitude. Three separate respiratory phases mean that one respiratory cycle is divided into four separate time intervals where the second and fourth phases represent the same spatial location and can be combined (Fig. 4-2, part 2). For phantom studies, the thresholds of respiratory phases were chosen to get equidistant respiratory motions for all phases.
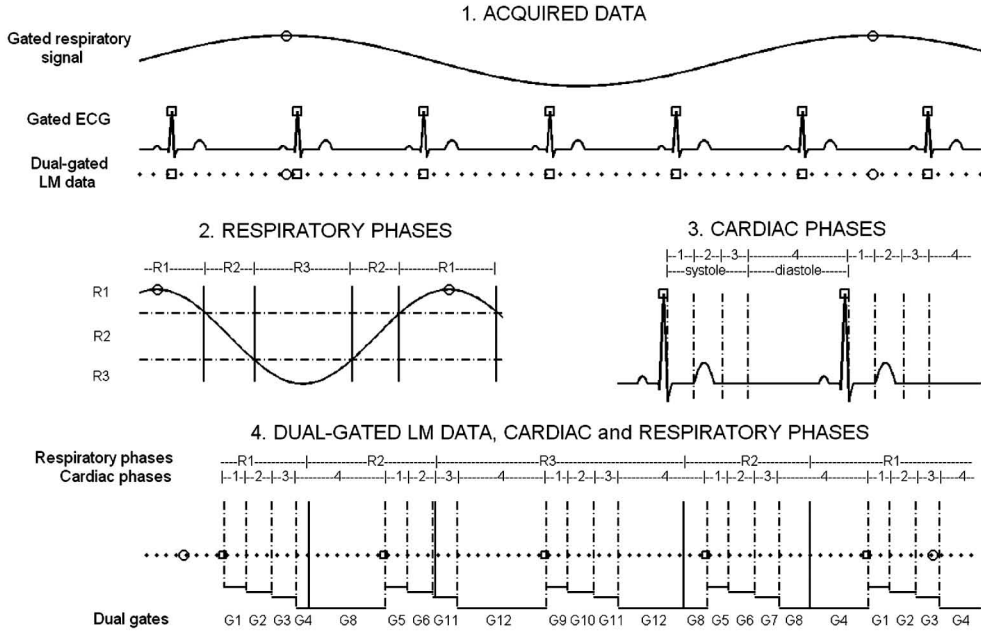
Figure. 4-2. Diagram of the dual gating method. *Part 1*: Gated respiratory motion data from RPM file, gated ECG signal and LM data with triggers. Open circle = respiratory trigger, open square = ECG trigger, dot = LM data event. *Part 2*: Respiratory phases determined by amplitude signal: R1=inspiration, R2=middle, and R3=expiration. Horizontal dashed lines indicate splitting of respiration cycle into three phases R1-R3. Vertical lines indicate onsets of respiratory phases R1-R3. *Part 3*: ECG phases: Phases 1 to 3 are constant systole intervals and phase 4 is time-varying diastole interval. Vertical dashed lines (1-4) indicate onsets of ECG phases. *Part 4*: Dual-gated LM data. Vertical full and dashed lines indicate respiratory (R1-R3) and ECG (1-4) labels on LM data. Dual gates (G1-G12) are determined by respiratory and ECG phase labels. Dual-gated LM data are divided into 12 different LM files.

The duration of systolic ECG phases were fixed assuming that the length of the systole varies significantly less than the length of the diastole which correlates with heart rate variations [Wang et al. 1999]. Only the last diastolic ECG phase is allowed to vary during the study. For different heart rates the duration of systolic ECG phases can be adjusted with the help of ECG-gated cardiac CT images from different patient studies. Determination of ECG and respiratory phases in the patient study is schematically illustrated in Figure 4-2 part 4 and Article (III), Table I.

4.3.1.2. Corrections to preserve quantitation

When processing the raw data to dual-gated data some basic attributes such as scan length (=BinDuration) and Events Lost stored into the raw data file (RDF) header of the scan are changed. These attributes are used in the reconstruction phase when calculating, for example, the scatter fraction, dead time correction and decay correction. When performing the segmentation with the dual gating algorithm, the time used for each segment is recorded. An algorithm for correcting the RDF header for the duration of each segment was developed and tested. This work is presented in detail in

the master thesis of Durand-Schaefer [Durand-Schaefer, 2008]. With these corrections the dual-gated algorithm is assumed to produce quantitative images without image artefacts.

4.3.2. Phantom tests

4.3.2.1. Quantification test

This test was performed using the IEC NEMA 2001 image quality phantom (Fig. 2-8) which simulates the body with non-uniform attenuation. Inside the phantom, spheres of different diameters are inserted. Three of these spheres with diameters of 10 mm, 17 mm and 28 mm were used in the test. The spheres were filled with a radioactive solution of ^{18}F-FDG at an activity concentration of 35.5 kBq/ml. The aim was to acquire a static phantom in dual-gated mode to verify that data post-processing does not alter the files and to validate the method as a quantitative method. By acquiring a static phantom, it was shown that there is no mis-registration of CTAC and PET images during the attenuation correction process. Moreover, it was also possible to compare the image quality and the correction factors of the dual-gated images with the reference static image. The acquisition was performed with the standard dual-gated PET method. First, a standard static CTAC scan was acquired for the attenuation correction purpose, followed by a 7 min dual-gated emission scan with simulated trigger events. The cardiac triggers were simulated with the ECG monitor operating in test mode at a heart rate of 65 bpm. The respiratory motion was mimicked with a mechanism that produces a respiratory-like motion of the reflector's box. The respiratory motion was followed with the RPM device and respiratory triggers were sent to the scanner as in standard dual-gated studies. After acquisition, data were unlisted with respiratory gated only and dual-gated modes. Both raw data file (RDF) dual-gated sets, with and without header adjustments, were reconstructed. Static RDFs with different acquisition times were created in order to compare the dual gates' parameters with the static reference parameters [Durand-Schaefer 2008].

In order to analyse the data, the scatter fraction, dead time and decay correction factors were corrected for all modes. Comparing these factors enables to assess the validity of the correction of the dual-gated images. The evolution of the signal-to-noise ratio (SNR) as a function of the acquisition time was also analysed. All three spheres were analysed in each image using a standard volume-of-interest (VOI) analysing method which computes the maximum value, the mean value and the standard deviation of the activity concentration within the sphere. To compute the SNR within the sphere, the following formula was used:

$$\text{SNR} = \frac{\text{Mean}_{\text{Activity concentration}}}{\sigma_{\text{Activity concentration}}} \quad (4\text{-}7),$$

where $\sigma_{\text{Activity concentration}}$ represents the standard deviation of the activity concentration within the VOI).

4.3.2.2. Rotating 2D phantom

The basic test of the dual gating method was carried out with a phantom mimicking respiratory and cardiac motions. The circular motion of the phantom represents contraction and the axial motion represents respiration. The phantom that consists of a disc that rotates on constant velocity and moves axially back and forth was constructed (Fig. 4-3). Motions are orthogonal and periodic and axial displacement, radius of circular motion and frequencies of both motions were adjustable. Both motions generate synchronized trigger signals during each period. The trigger signals are launched by a magnetic and a mechanical sensor. The phantom was connected to the PET/CT with two trigger inputs. Trigger signals from the phantom were sent via these inputs to the LM data.

The phantom study was carried out with the following parameters: radius of circular motion was 30 mm and axial displacement 20 mm. Frequencies of ECG and respiratory motions were set to 54 cycles/min and 17 cycles/min, respectively. A CT attenuation correction (CTAC) scan and a 5 min dual-gated emission scan were acquired using a cylindrical (3 mm diameter and 5 mm height) radioactive source of ^{11}C attached to the rotating disk.

4.3.2.3. The heart phantom

The ability to image coronary plaques with the dual-gating method was tested with a cardiac phantom [Sipilä et al.2007] mimicking respiratory and cardiac motions. The phantom consists of two balloons forming the myocardium and the left ventricle. Coronary tubes were placed on the surface of the myocardium, and four plaques were placed beside the coronaries (Fig. 4-3). Coronaries, myocardium, and ventricle were filled with radioactive concentrations of ^{18}F-FDG and CT contrast agent estimated from human studies performed at our centre (see article III, Table II). The ventricles and the myocardium had a concentration of 1 kBq/ml and 0.2 kBq/ml, respectively. Plaques were manufactured by diluting small ceramic spheres (diameter around 3mm) with different concentrations of ^{18}F-FDG solution, and the activity of each sphere was measured with a cross-calibrated well counter. The activities were 6 kBq, 3 kBq, 2 kBq and 1 kBq.

The heart was contracted by a pneumatic pump and respiratory motion was simulated by an axially moving box inside which the axial position of the heart was fixed. The box was filled with water to achieve more realistic attenuation and scatter conditions. Respiratory motion was connected with an IR-reflector to the RPM system. Pumping rate and time of diastole (delay of contraction) were set to 51 bpm and 400 ms, respectively. Respiratory rate was set to 19 cycles/min.
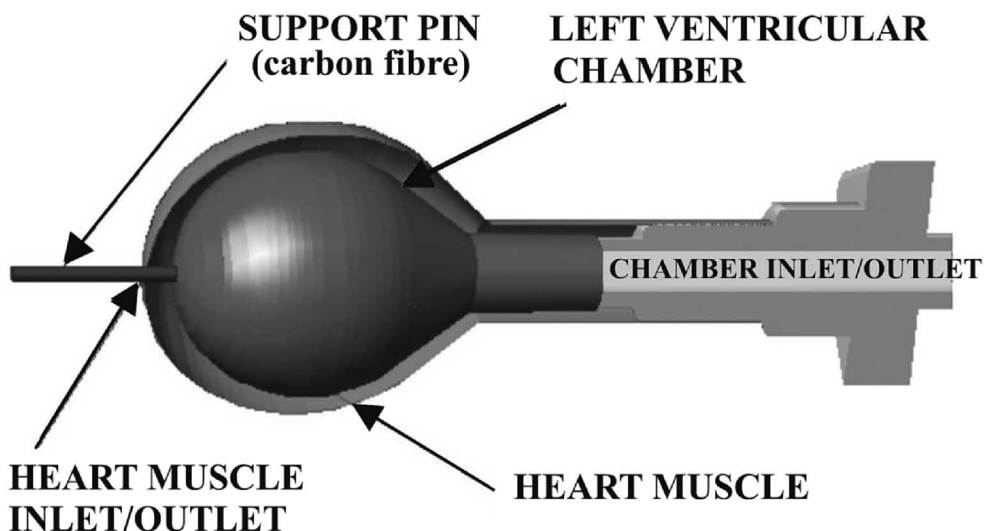
Figure 4-3. Graph (top) and photograph (below) of the heart phantom: two balloons form myocardium and left ventricle. The apex of the heart is supported with a pin. Both compartments are filled separately. Left ventricular chamber was contracted by a pneumatic pump. Additional coronary tubes and plaques are seen on the surface of heart muscle (not in graph). The phantom is in a box filled with water.

The following imaging protocol was used:

> (1) Respiratory-gated CTAC
> (2) 30 min dual-gated PET scan
> (3) 5 min PET static scan without any motions

Cardiac phases were chosen so that systolic phases were of equal length in time (260 ms) and the diastolic phase was set to match the delay phase. Respiration phases were chosen so that each phase includes the same spatial amount of respiration amplitude. Data processing was done as described previously (Fig. 4-2).

4.3.2.4. The minipig study

In minipig study a radioactive source in the tip of coronary catheter was prepared and placed into a coronary artery and imaged with and without respiratory and contraction movement both with PET and CT. The study was performed both with and without background radioactivity.

The radioactive source was prepared by cutting a standard coronary catheter (5F) from the distal end and placing a small (length 2mm and diameter 1 mm) radioactivity with a known activity into the catheter, and the tip was sealed. The activity of the tip was measured in a cross-calibrated well counter (3"x3" NaI crystal, Ortec, Knoxville, USA) and was around 6 kBq.

The pigs were anesthetised and put in the respirator and then moved to a catheterization laboratory. Catheterization was performed by an experienced

cardiologist and angiographic images were obtained to localize the tip of the catheter containing the activity. The movement of the catheter tip due both to cardiac and respiratory cycles was evaluated.

In the imaging protocol was as follows:

- a CT angiography using standard protocol
- a standard CT attenuation correction scan (CTAC) with 100 kV and 80mAs in breath-hold (respirator off)
- a 15 minute PET scan with LM and 2 trigger signals (ECG and respiratory)
- injection of the background radioactivity (approximately 50 MBq of $[^{18}F]$-FDG)
- a 15 minute PET scan with LM and 2 trigger signals (with background radioactivity)
- CineCTAC with triggering from the RPM in order to respiratory gate also the attenuation u-map
- sacrifice of the minipig
- a standard CTAC (without movements)
- a 5 minute static PET (without movements)

The study was analysed with manufacturer's gating protocols and with the developed dual gating technique. The real movement of the tip was estimated from the angiograms. The project was approved by ethical committee for animal studies (1606/06).

4.3.3. Patient study

4.3.3.1. Human cardiac data

The patients who have been referred for cardiac FDG PET studies due to suspected cardiac sarcoidosis were studied using dual gating. In addition, one patient with documented coronary artery disease (CAD) was studied. A dual-gated acquisition 60-120 minutes after injection of 260 MBq of $[^{18}F]$-FDG was performed for 8 minutes or 30 minutes (patient with CAD). CineCTAC for matching individual gates with the attenuation correction with the same respiratory phase was performed only with the patient with CAD. Images were reconstructed with the scanners' standard gating protocols and with our dual gating protocol. The dual-gated images were analysed qualitatively (visual comparison) and quantitatively using the analysing tools of the AW Workstation (General Electric Medical Systems, Milwaukee, USA).

5. RESULTS

5.1. PET performance of DVCT (I)

Spatial resolution

Transverse and axial resolution (FWHM and FWTM) values according to NEMA NU-2 2001 in 2D and 3D, and axial resolution values derived from the axial slice width test in 2D according to NEMA NU-2 1994 are reported in Table 5-1. Spatial resolution for 2D (3D) mode in FWHM was 4.87 mm (5.12 mm) in the centre, and radial and tangential resolutions were 5.70 mm and 5.84 mm (5.89 mm and 5.47 mm), respectively, at 10 cm offset from the centre. In Figures 5-1 and 5-2 representative axial profiles are shown.

Table 5-1. Spatial resolution FWHM and FWTM results.

Spatial resolution (mm)			2D	3D
NEMA NU-2 2001				
R1 = 1cm off centre	FWHM	Average radial and tangential	4.9	5.1
	FWTM		9.3	9.8
R10 = 10cm off centre	FWHM	Radial	5.7	5.9
		Tangential	5.8	5.5
	FWTM	Radial	10.2	11.2
		Tangential	12.8	10.3
Axial resolution (mm)				
R1 = 1cm off centre	FWHM		4.4	5.2
	FWTM		8.7	10.2
R10 = 10cm off centre	FWHM		9.0	5.9
	FWTM		11.9	11.4
NEMA NU-2 1994				
Axial resolution (mm)				
1 cm	FWHM		4.0	
10 cm	FWHM		5.5	

a)   b)
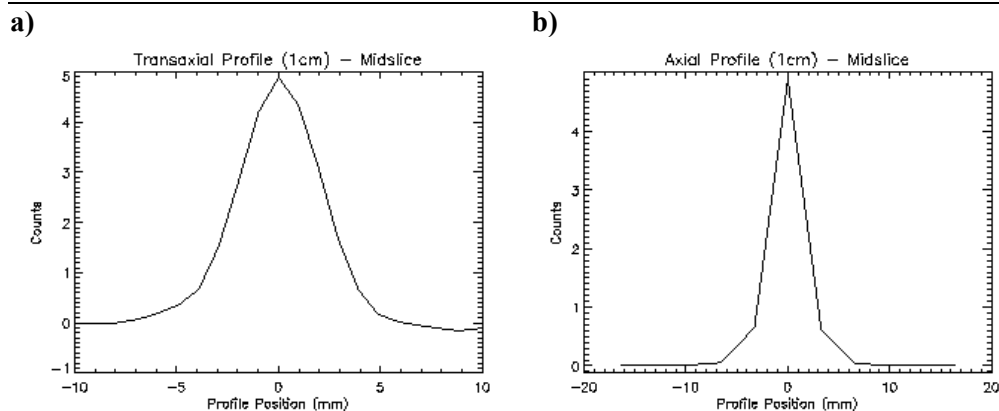
Figure 5-1. Spatial resolution plot for 2D measurement: **a** radioactivity profile transaxially at 1 cm off-centre where FWHM is 4.9 mm, **b** axial profile at 1 cm off-centre where FWHM is 4.4 mm (Note: different scales on X-axis).

a)   b)
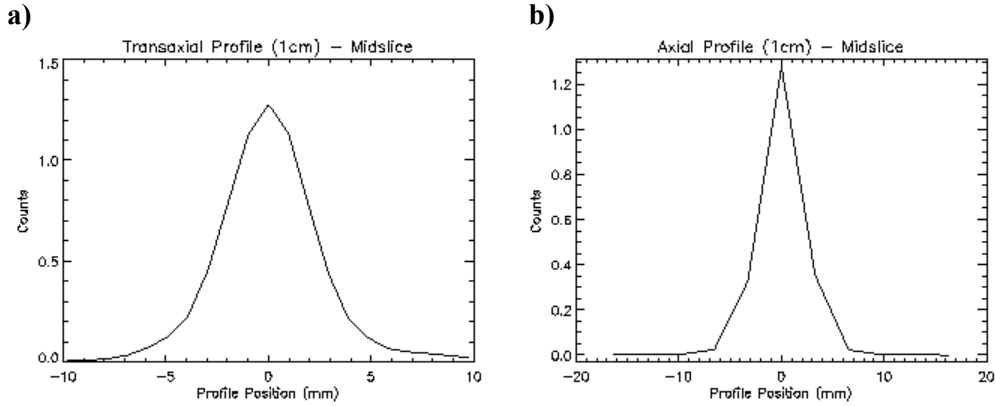
Figure 5-2. Spatial resolution for 3D measurement: **a** radioactivity profile transaxially at 1 cm off-centre where FWHM is 5.1 mm, **b** axial profile at 1 cm off-centre where FWHM is 5.2 mm.

Sensitivity

The results of sensitivity measurements are shown in Table 5-2. The low level energy discrimination (lld) of 375 keV is shown for both 2D and 3D as we tested with the STE. The lld of 425 keV is used in VCT but only for 3D, whereas the lld of 375 keV remains for 2D. The sensitivity loss in 3D mode with the higher lld is approximately 18 % from 9.3 cps/kBq to 8.8 cps/kBq in R0 and from 9.7 cps/kBq to 8.9 cps/kBq in R10. Figures 5-3 and 5-4 show the slice sensitivity profiles for 2D and 3D, respectively.

Table 5-2. Sensitivity for 2D and 3D with lld 375 keV and for 3D with lld of 425keV.

Sensitivity (cps/kBq)	2D lld 375	3D lld 375	3D lld 425
R0 = at centre	2.3	9.3	8.8
R10 = 10cm off centre	2.3	9.7	8.9

a)   b)
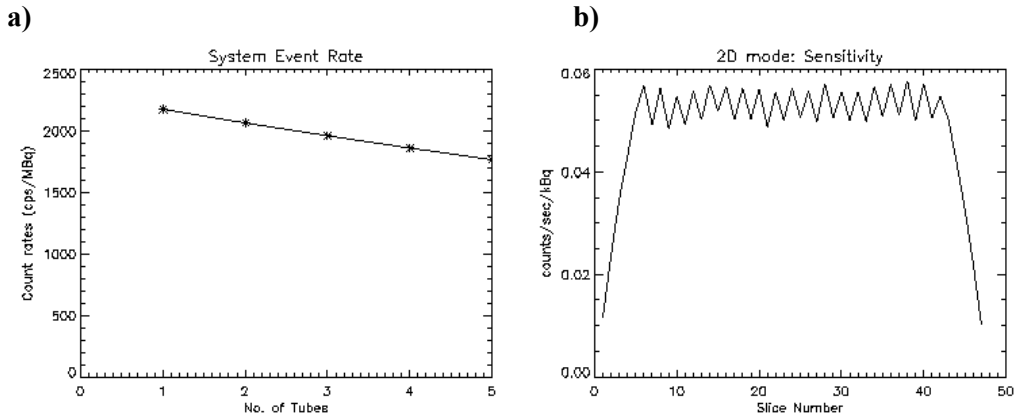
Figure 5-3. Sensitivity for 2D (lld of 375 keV) in the centre of the FOV: **a)** system event rate as function of wall thickness (number of attenuating tubes), **b)** sensitivity value per plane which yields a system sensitivity of 2.3 cps/kBq.

a)   b)
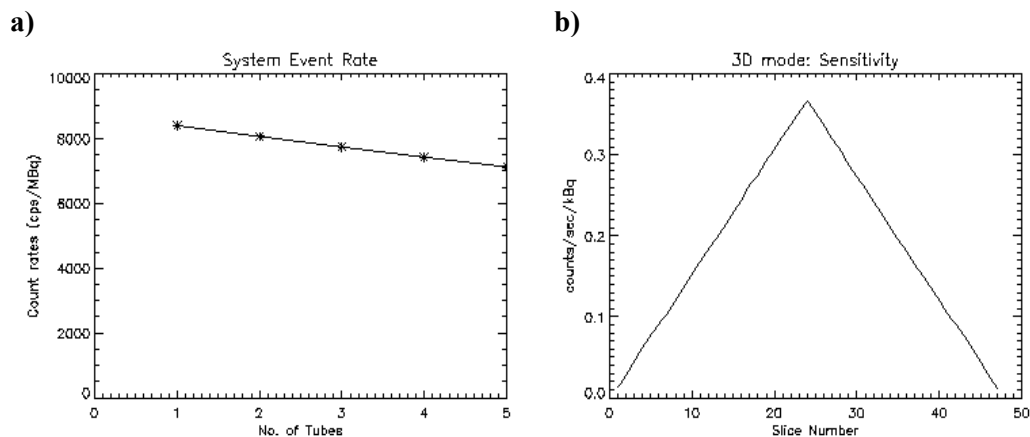
Figure 5-4. Sensitivity for 3D (lld of 425 keV) in the centre of the FOV: **a)** system event rate as function of wall thickness, **b)** sensitivity value per plane which yields a system sensitivity of 8.8 cps/kBq.

Scatter fraction, count rate performance and randoms test

The results for the scatter fraction as well as peak, true, random, scatter and NEC rates are shown in Table 5-3. In 2D the lld was set to 375 keV, but in 3D there are results for both lld 375 keV and lld 425 keV. The scatter fraction in 2D is 21.4%, and in 3D it is reduced from 44.7 % to 33.9 % when comparing the lld values 375 keV and 425 keV. Count rate curves against activity concentrations for true, random, scatter and NEC rates (k=1 and k=2) are displayed in Figures 5-5 and 5-6. The maximum error for count losses and randoms for 2D and 3D was 1.31 % and 1.94 %, respevtively for activity concentrations below corresponding peak NEC (k=1) rates.

Table 5-3. Count rate test and scatter fraction results with lld of 375 keV and lld of 425 keV.

	2D – lld 375 keV	3D – lld 375keV
System scatter fraction	21 %	45 %
Peak trues rate	300 kcps @ 110 kBq/ml	310 kcps @ 29kBq/ml
Peak randoms rate	1760 kcps @ 146 kBq/ml	2400 kcps @ 47 kBq/ml
Peak scatter rate	81 kcps @ 110 kBq/ml	250 kcps @ 29 kBq/ml
Peak NEC (k=1) rate	85 kcps @ 44 kBq/ml	62 kcps @ 11 kBq/ml
Peak NEC (k=2) rate	57 kcps @ 32 kBq/ml	43 kcps @ 8.3 kBq/ml
	2D – lld 375 keV (repeated)	3D – lld 425 keV
System scatter fraction	20.3%	33.9%
Peak trues rate	300 kcps @ 110 kBq/ml	250 kcps @ 32 kBq/ml
Peak randoms rate	1500 kcps @ 120 kBq/ml	2000 kcps @ 42 kBq/ml
Peak scatter rate	76 kcps @ 110 kBq/ml	130 kcps @ 32 kBq/ml
Peak NEC (k=1) rate	88 kcps @ 47 kBq/ml	68 kcps @ 12 kBq/ml
Peak NEC (k=2) rate	61 kcps @ 38 kBq/ml	49 kcps @ 10 kBq/ml

a)   b)
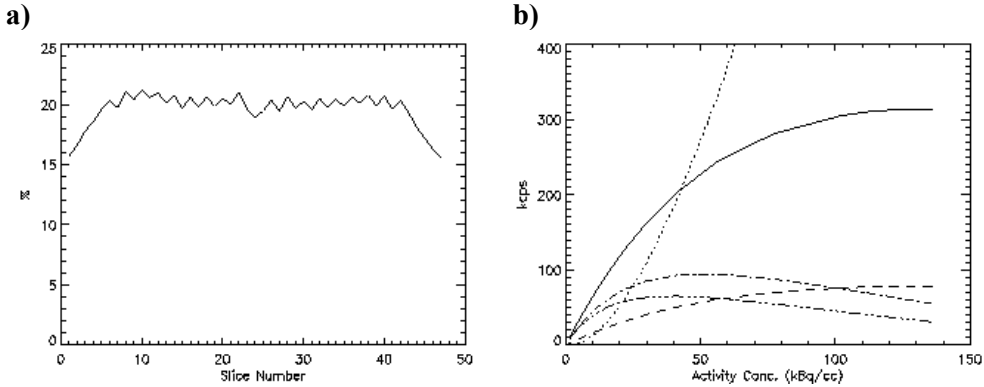
Figure 5-5. Scatter fraction and count rate performance in 2D. **a)** System scatter fraction in 2D was 20%, here SF is printed for each plane. **b**) Curves for 2D scattered events (dashed curve), random events (point curve), true events (solid curve), NEC (k=1) (point dash curve) and NEC (k=2) (3 points dash curve) rates as function of radioactivity concentration.

a)   b)
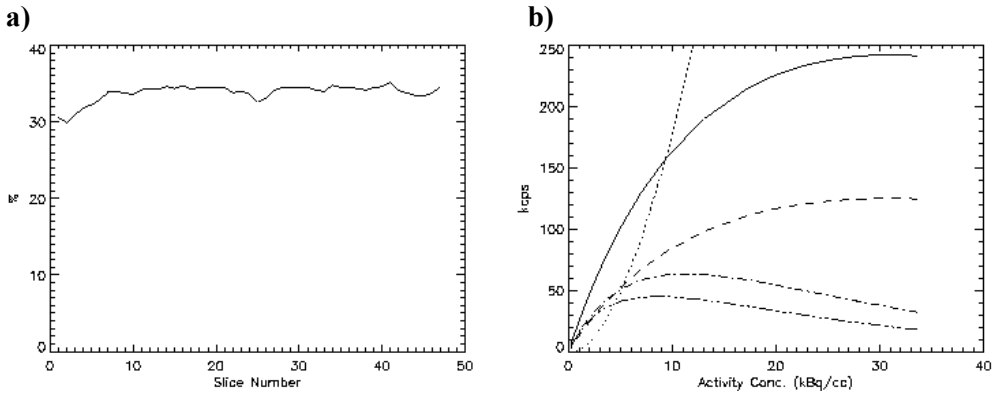
Figure 5-6. Scatter fraction and count rate performance in 3D. **a)** System scatter fraction in 3D was 34% with lld value 425 keV. **b)** Curves for 3D scattered events (dashed curve), random events (point curve), true events (solid curve), NEC (k=1) (point dash curve) and NEC (k=2) (3 points dash curve) rates as function of radioactivity concentration

Image quality test

Image quality results for hot sphere recovery coefficient, cold sphere contrast, average residual attenuation and scatter correction error in the lung region and background variability are shown in Figure 5-7 and Table 5-4. All results shown are for the VCT where in 2D the lld was set to 375 keV and in 3D the lld is set to 425 keV. Hot and cold sphere contrasts were slightly better in 3D than in 2D. Average lung residual was around 30 % in all tests. Comparison with ST shows that cold lesion and lung residual results give higher values in the new system. In addition to the clinically used reconstruction parameters (128x128 matrix and 2 iterations), results of the image quality data are tabulated using a greater 256x256 matrix and 4 iterations.

a)

b)
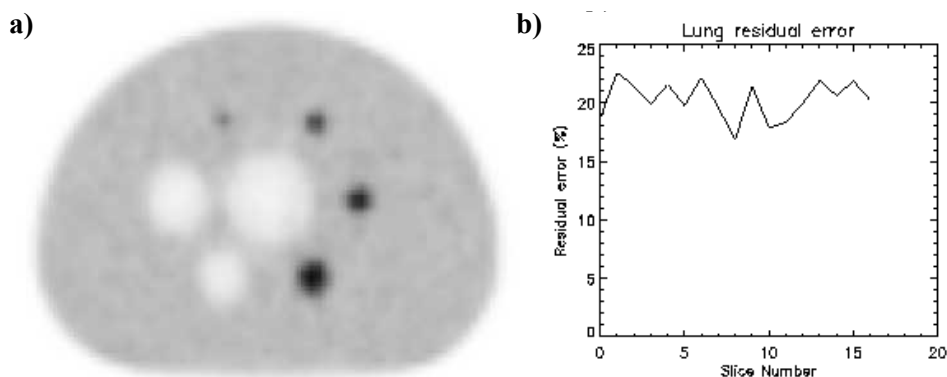
Figure 5-7. Image quality: **a)** sphere positioning for image quality measurement according to NEMA NU-2 2001, **b)** lung residual error plot to show the scatter and attenuation correction accuracy (AC) for a 2D scan.

Smaller pixel size (5.47mm vs. 2.73 mm) resulted in better hot sphere contrast and higher iteration count resulted in better cold sphere contrast and lower lung residual. The increased noise, on the other hand, gave higher background variability values.

Table 5-4. Image quality test results for the VCT.

	128x128 matrix 2 iterations							256x256 matrix 4 iterations						
	lung	Sphere diameter (mm)						lung cylinder	Sphere diameter (mm)					
		10	13	17	22	28	37		10	13	17	22	28	37
3D ratio 8/1														
Hot sphere contrast (%)		31	41	56	68				58	62	68	79		
Cold sphere contrast (%)						51	63						62	75
Background variation (%)		6	6	6	5	5	5		13	10	8	7	7	6
Avg. residual lung error (%)	32							22						
3D ratio 4/1														
Hot sphere contrast (%)		22	40	55	66				44	64	71	79		
Cold sphere contrast (%)						57	64						67	71
Background variation (%)		5	4	4	4	3	3		8	7	6	5	4	3
Avg. residual lung error (%)	30							22						
2D 8/1														
Hot sphere contrast (%)		25	39	51	66				52	60	62	76		
Cold sphere contrast (%)						60	69						66	82
Background variation (%)		7	6	6	5	4	3		21	17	14	10	8	6
Avg. residual lung error (%)	31							23						
2D 4/1														
Hot sphere contrast (%)		14	34	49	56				43	54	70	65		
Cold sphere contrast (%)						65	68						76	78
Background variation (%)		6	6	5	4	4	3		21	15	11	8	6	4
Avg. residual lung error (%)	29							22						

5.2. PVC (II)

5.2.1. Results of quantification

Quantification results of the Hoffman phantom images are shown in Table 5-5. The results are given both before and after the correction for all three tomographs. The PVE-corrected values were divided by the calculated theoretical values to quantify recovery.

PVE-corrected Mean Radioactivity.

The main focus of the evaluated PVC methods is to correct the PET GM radioactivity values. The corrected WM values are used when calculating the PVE corrected GM activities, except in the case of the R-PVC method, which gives equal focus to all the regions. The relative performance of the three WM estimation methods (A-WME, R-WME, CS) varied depending on the PET tomograph. The R-WME estimates were higher than the A-WME estimates with all three PET tomographs. With the GE Advance and HRRT, the CS method gave good estimates for WM, but with the PET-CT, considerable overestimation occurred. The PVE corrected WM mean value for the M-PVC method was higher than the non-corrected value in all the tomographs. The MG-PVC method was more robust to the changes of the WM estimation value than the A-PVC method as seen from the GM values when using different WM estimations in Table 5-5.

Table 5-5: PVC results for a Hoffman phantom. The mean radioactivity values (Bq/ml) are shown for areas of GM and WM for three different PET tomographs. Recovery rate = radioactivity in relation to the calculated true values of GM and WM; SD increase = increase in standard deviation of the radioactivity values in the GM and WM regions when compared to non-corrected image when applicable.

GM			WM			PVC	WM
Bq/ml	recovery rate	SD increase	Bq/ml	recovery rate	SD increase	method	estimation
PET-CT							
36378	65.3%		19863	142.6%		Non-corrected	
55067	98.9%	37.5%	12871	92.4%		A-PVC	A-WME
52414	94.1%	49.4%	16600	119.2%		A-PVC	R-WME
51818	93.0%	57.4%	17438	125.2%		A-PVC	CS
50231	90.2%	21.6%	12871	92.4%		MG-PVC	A-WME
49628	89.1%	21.5%	16600	119.2%		MG-PVC	R-WME
49492	88.9%	21.6%	17438	125.2%		MG-PVC	CS
46177	82.9%	20.4%	21854	156.9%	24.3%	M-PVC	
52154	93.6%		16603	119.2%		R-PVC	
GE Advance							
11266	60.6%		6625	142.5%		Non-corrected	
17602	94.6%	56.1%	4345	93.4%		A-PVC	A-WME
16682	89.7%	68.7%	5629	121.0%		A-PVC	R-WME
17505	94.1%	54.6%	4481	96.4%		A-PVC	CS
15815	85.0%	30.8%	4345	93.4%		MG-PVC	A-WME
15595	83.8%	29.8%	5629	121.0%		MG-PVC	R-WME
15792	84.9%	30.6%	4481	96.4%		MG-PVC	CS
11492	77.9%	29.3%	7296	156.9%	25.1%	M-PVC	
16016	86.1%		5907	121.0%		R-PVC	
HRRT							
37205	80.0%		16084	138.4%		Non-corrected	
49254	105.9%	48.9%	11302	97.2%		A-PVC	A-WME
47322	101.8%	55.4%	13633	117.3%		A-PVC	R-WME
48405	104.1%	44.6%	12326	106.0%		A-PVC	CS
44283	95.2%	13.0%	11302	97.2%		MG-PVC	A-WME
43989	94.6%	12.7%	13633	117.3%		MG-PVC	R-WME
44154	95.0%	12.8%	12326	106.0%		MG-PVC	CS
41506	89.3%	16.6%	16222	139.5%	2.2%	M-PVC	
45429	97.7%		13633	117.3%		R-PVC	

In the corrected GM radioactivity values there was a general trend towards the correction efficiency decreasing in the following order of PVC methods: A-PVC, R-PVC, MG-PVC and M-PVC. The highest efficacy was observed for the A-PVC method. The same order of results generally held for all three tomographs. The GM activity calculated for the HRRT tomograph was relatively good, even prior to PVC. Due to having the highest tomograph resolution, the PVE-corrected mean radioactivity values with HRRT were also closest to the calculated values. The HRRT tomograph with A-PVC slightly overestimated the mean activity, but the percentage error was still of the same magnitude as with R-PVC and MG-PVC.

Distribution of the radioactivity values.

The PVC not only changes the mean radioactivity values of the regions, but also affects their distributions (see Fig. 5-8), when a 3x3x3 voxel kernel was used to calculate the standard deviation for each voxel. With the MG-PVC method, the increase in standard deviation of voxel values in GM and WM varied between the PET tomographs, but it produced a small increase in deviation with all the tomographs (Table 5-5). It was not possible to calculate the change in standard deviation in the WM region for the A-PVC and MG-PVC methods, since these methods produce only an estimate of the true mean radioactivity value for that region. The R-PVC method did not provide standard deviation for either GM or WM.
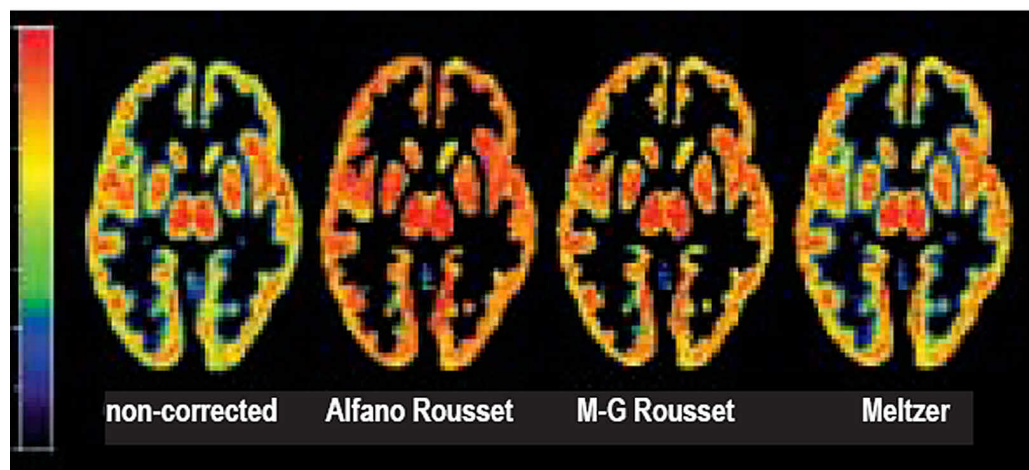
Figure 5-8. Distribution of the standard deviation in a PET image before and after PVC (Bq/ml). Form left to right: non-corrected, A-PVC, MG-PVC and M-PVC WM estimation by Rousset was used in A-PVC and MG-PVC.

5.2.2. Test-retest results

The mean BP values and mean variability between test sets were calculated for the four regions of interest. In addition, the ICC values were calculated for the eight PVC methods. The values were acquired by correcting the image data from eight human subjects scanned twice. A summary of four of the methods is shown in Table 5-6. The results of the A-PVC and MG-PVC methods used with the WM estimation methods other than A-WME were essentially similar. As a general observation, almost all the

tested correction methods increased the mean BP values in all the examined brain ROIs. A-PVC gave higher BP values than MG-PVC in almost all cases. This result is in accordance with the phantom tests. The R-PVC method resulted in mean BP estimates of $[^{11}C]$raclopride close to the mean values of A-PVC and MG-PVC. The mean BP values were lowest with the M-PVC method. The mean BP values of the methods varied most in the thalamus regions, which were particularly difficult to segment. The standard deviation of the calculated BP increased as a result of PVC in most of the ROIs.

The variation in the ICC values was one of the main issues of interest, and there were indeed large differences between the different methods in this respect. The M-PVC method gave ICC values that were greater than or similar to the non-corrected images in all ROIs. The R-PVC method also performed well, with a slight decrease in the results of the caudate and medial thalamus regions.

The performance of the A-PVC and MG-PVC methods varied among the examined regions. In the lateral thalamus region all the PVC ICC values were greater than the non-corrected values. In the medial thalamus, the A-PVC and MG-PVC methods resulted in markedly smaller ICC values than with non-corrected images. The null hypothesis in the test-retest data was that the mean BP values of the test and retest scans would be equal. This hypothesis was not disproved in any region with any PVC method ($p < 0.05$, see Table 5-6). The mean BP value over all 16 studies with non-corrected data was found to be significantly different from the corresponding values of all PVC methods ($p < 0.05$) except in the putamen and lateral thalamus regions with M-PVC (in putamen, significance found when $p < 0.1$). For the mean variability (VAR) over eight subjects, the only significant differences were found with A-PVC in the caudate region ($p < 0.05$, variability increased) and in the thalamus region ($p < 0.1$, variability decreased).

Table 5-6 Effect of the PET PVC methods on BP estimated by SRTM for different brain regions. The test set consists of eight subjects. Each subject was scanned twice: mean = mean value of BP over all 16 scans; VAR = mean variability between two scans over eight subjects; t-value = tvalue between the mean values of test and retest scans (df=7, critical value=2.306 with $p<0.05$); ICC = mean intra-class correlation value between scans over eight subjects. Alfano and Müller-Gärtner methods were used with the WM estimation method by Alfano et al. as no difference is seen between WM corrections.

Method		Brain region of interest			
		Caudate	Putamen	Lateral thalamus	Medial thalamus
No correction	mean ± SD	1.81 ± 1.63	1.31 ± 1.22	2.10 ± 1.69	1.82 ± 1.58
	VAR	3.45	4.93	7.88	8.25
	ICC	0.98	0.91	0.83	0.89
	t-value	0.69	1.03	0.60	1.23
Alfano et al. WME Alfano	mean ± SD	2.82 ± 2.60	2.27 ± 1.81	2.71 ± 2.50	2.04 ± 1.84
	VAR	5.49	5.84	4.76	6.83
	ICC	0.92	0.94	0.98	0.75
	t-value	0.76	1.16	1.24	1.22
Müller-Gärtner et al. WME Alfano	mean ± SD	2.50 ± 2.34	1.86 ± 1.70	2.40 ± 2.26	2.31 ± 1.88
	VAR	4.35	6.13	6.32	8.23
	ICC	0.94	0.88	0.93	0.77
	t-value	0.76	1.02	0.85	1.48
Rousset et al. no WME	mean ± SD	2.03 ± 2.39	1.28 ± 1.60	2.24 ± 2.30	1.70 ± 1.90
	VAR	4.08	5.92	8.89	11.41
	ICC	0.97	0.92	0.94	0.84
	t-value	2.20	1.98	0.81	1.06
Meltzer et al. no WME	mean ± SD	1.92 ± 1.68	1.33 ± 1.24	2.19 ± 1.71	1.84 ± 1.58
	VAR	3.25	5.21	7.99	9.15
	ICC	0.98	0.92	0.87	0.91
	t-value	1.65	1.15	0.86	1.31

5.3. Results from the dual gating method (III, IV)

5.3.1. Quantification

The static whole body image quality phantom results are compared with and without header correction, and also from the static images unlisted with different acquisition durations. The results are shown in Table 5-7. Since the reconstruction algorithm is dependent on the statistics (= acquisition time), it is important to compare dual gates with static images that have the same acquisition duration. The decay correction factor is constant in all dual-gated images. However, this correction factor increases with acquisition time in static images. This evolution of the decay correction factor is normal in static images since the decay correction is computed as a function of acquisition duration and radiotracer properties.

Table 5-7: Correction factors of dual-gated images with and without header adjustments compared to correction factors of static images with different acquisition times (na = not applicable).

	Dual Gated Images without RDF Header Adjustments			Dual Gated Images with RDF Header Adjustments			Static Images Parameters			
Time (s)	Scatter Fraction Factor	Dead-time Factor	Decay Factor	Scatter Fraction Factor	Dead-time Factor	Decay Factor	Time (s)	Scatter Fraction Factor	Dead-time Factor	Decay Factor
7,89	να	53,13	1,0227	0,12	1,001	1,0227	8	0,12	1,001	1,0004
8,64	να	48,89	1,0227	0,12	1,001	1,0227	9	0,12	1,001	1,0005
12,93	να	32,67	1,0227	0,13	1,001	1,0227	13	0,13	1,001	1,0007
13,11	να	32,02	1,0227	0,13	1,001	1,0227	18	0,14	1,001	1,0010
17,77	0,99	23,87	1,0227	0,15	1,001	1,0227	29	0,15	1,001	1,0015
28,73	0,68	14,77	1,0227	0,16	1,001	1,0227	49	0,16	1,001	1,0026
28,97	0,65	14,52	1,0227	0,16	1,001	1,0227	50	0,16	1,001	1,0026
29,27	0,66	14,46	1,0227	0,16	1,001	1,0227	64	0,17	1,001	1,0034
49,49	0,38	8,55	1,0227	0,17	1,001	1,0227	111	0,19	1,001	1,0059
49,95	0,37	8,48	1,0227	0,17	1,001	1,0227	420	0,22	1,001	1,0223
64,13	0,29	6,58	1,0227	0,17	1,001	1,0227				
111,1	0,23	3,80	1,0227	0,19	1,001	1,0227				

The dead-time correction factors of dual-gated images with RDF header adjustments are equal to the correction factors of static images. This correction factor is constant regardless of the acquisition duration which was expected since the dead-time correction is mainly dependent on the count rate. On the contrary, the dead-time correction factor of dual-gated images without RDF header adjustments decreases with increasing acquisition duration. Thus, it can be concluded that the dead-time correction is efficiently performed in the enhanced the dual -gated protocol.

The scatter correction factor is clearly mis-computed in dual-gated images without RDF header adjustments. The scatter correction factors of the dual-gated images with RDF header adjustments are similar to those of corresponding static images. Since the precise description of the scatter correction algorithm implemented in VUE Point has not been published by the manufacturer, it is difficult to explain the increase in the scatter fraction with increasing acquisition duration. One explanation could be that the scatter correction algorithm requires enough coincidence events to give a good estimate of the scatter fraction within two iterations. Thus, the algorithm can not reach the estimate of the scatter fraction with a short acquisition time. Since the values of corrected dual gates and static images are similar, it can be estimated that the scatter correction is performed correctly in the dual gating protocol [Durand-Schaefer 2008].

5.3.2. Rotating 2D phantom

All LM data between first and last trigger event of axial motion were written into the 12 separate LM files (Article III, Table III). The motions of the 2D phantom remained

stable during the scan. The periodic time of the rotating movement was stable at 1118 ms ± 7 ms derived from triggers of rotating motion. The periodic time of axial movement triggers was stable at 3462 ms ± 14 ms. Dual-gated images showed that the movement of the source was separated into 12 spatially different segments with well-defined borders on the cylindrical surface. Circular motion was divided into and four axial motion into three periods of equal length.
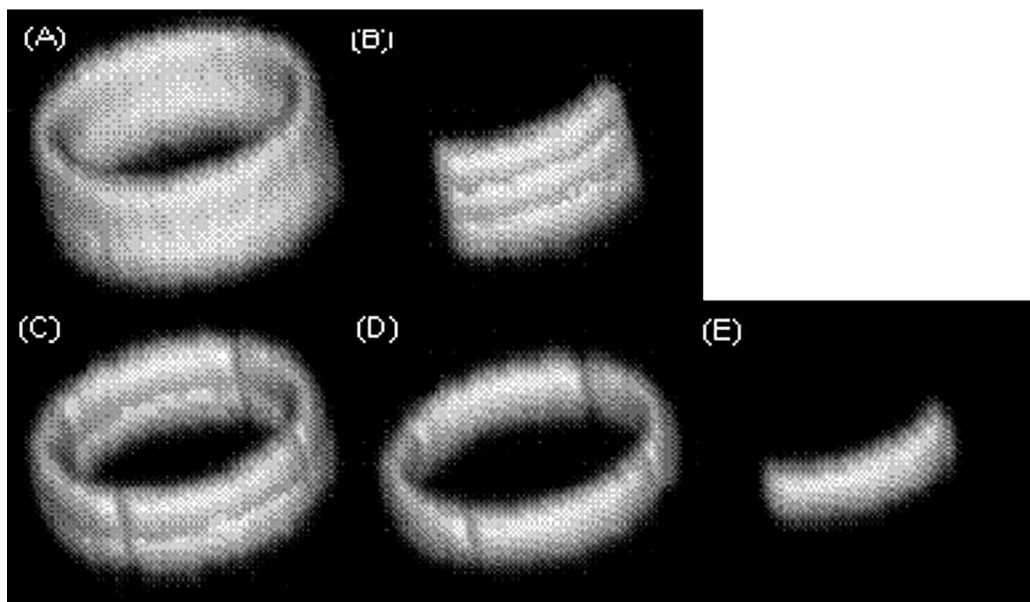
Figure 5-9. Dual-gated PET images from 2D phantom study. (A) Non-gated image. (B) Fused image of three dual-gated axial phases. (C) Fused image of eight dual-gated phases during the two axial phases. (D) Fused image of four dual-gated phases during the same axial phase. (E) A single dual-gated phase out of 12 phases. All dual-gated PET images had well-defined borders on the cylindrical surface.

5.3.3. The heart phantom

Stability of contraction and axial motion frequencies during PET scan were analysed utilizing triggers in LM data. Both motions were stable: periodic time of contraction was 1178 ms ± 3 ms, and periodic time of respiration 3172 ms ± 58 ms. Three plaques out of four were clearly detectable in all dual-gated PET images (Fig. 5-10). The fourth plaque with the lowest activity concentration is not detected accurately. Image analyses were done between every dual-gated image, image without gating, and image from the scan without motions. The analysis focused on one representative plaque with a total activity of 6 kBq. Motion analyses were performed so that the activity profile of the plaque was measured in axial, sagittal, and coronal directions over the maximum voxel position. The maximum pixel value and pixels next to it were used to fit parabolic function to determine the peak activity value of the plaque and the position of the peak value, defined as the centre of the plaque, in the analysed direction. The peak value was used to define the value of full width at half maximum (FWHM) in all three directions.
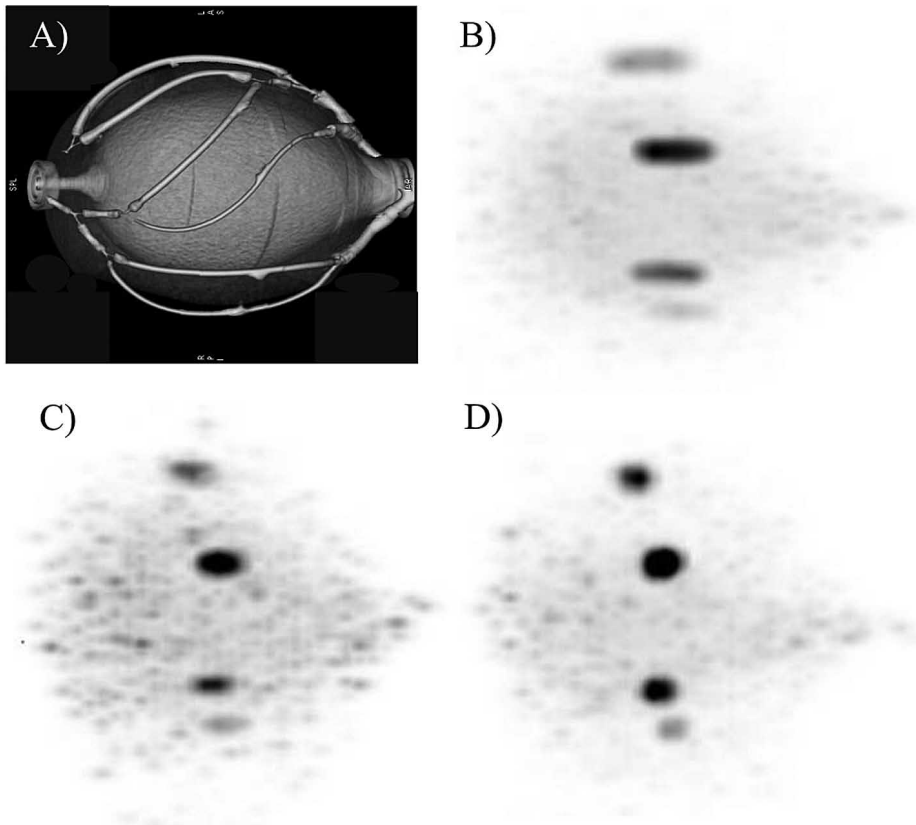
Figure 5-10. Comparison of (A) CTA image from no motion phantom, (B) non-gated PET image, (C) dual-gated 12 PET image, and (D) no-motion PET image. In the CTA image the left ventricle and coronaries of the phantom are clearly visible. The axial dimensions of plaques are evidently reduced in the dual-gated image when compared to the non-gated image. All images are 3D-projection images.

The mean motion of the centre of the plaque between different respiratory and contraction phases is reported in Table 4 (article III). It can be seen that during respiratory motion, the plaque is moved around 6 mm between adjacent respiratory phases. Within the respiratory phases, the SDs of peak value positions of different dual gates are less than 1.3 mm. Table 4 (article III) also shows that during contraction, plaque is moved between diastolic and systolic positions about 2.6 mm in the sagittal direction and about 2.0 mm in the coronal direction. Within the coronary phases, SDs of peak value positions of different dual gates is less than 0.5 mm in the sagittal and less than 0.3 mm in the coronal direction. Maximum displacements between dual gates were the following: in the axial direction 14.1 mm (between dg 2 and dg 9), in the sagittal direction 3.2 mm (between dg 9 and dg 11), and in the coronal direction 2.6 mm (between dg 2 and dg 12). Activity profiles from dual-gated images 6, 8, 4, and 12 are presented in Figure 5-10. Combining both contraction motion directions to get radial motion a 3.6 mm radial motion separation is achieved between dual gates 7 and 8. This means that a 51 % motion elimination of contraction motion (true motion 7.0 mm) and a 70 % motion elimination of respiratory motion (true motion 20.0 mm) are achieved.
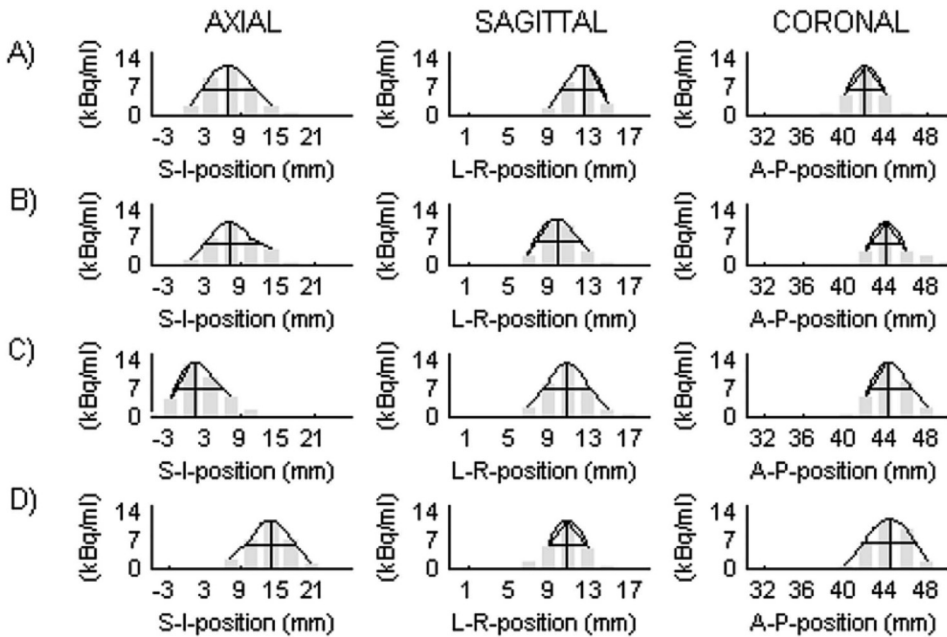
Figure 5-11. The motion of a plaque in dual-gated images. Activity profiles are given in three orthogonal directions: (A) Dual gate 6, (B) dual gate 8, (C) dual gate 4, and (D) dual gate 12. Activity profiles of (A) and (B) represent the contraction motion of the plaque: 2.6 mm sagittal and 2.1 mm coronal displacement. Activity profiles of (C) and (D) represent the respiratory motion of the plaque: 12.3 mm axial displacement. Motion in other directions not quantified here is negligible.

In Table V (article III), peak activity values from dual-gated images, image without gating, and image from the scan without motions are shown. The values are mean of the peak activity values of three orthogonal directions. The average peak activity value from all dual-gated images (12.2 kBq/ml) shows an 89 % increase of recovery of activity compared to the image with no motion correction (6.5 kBq/ml). The average peak activity value from all dual-gated images (12.2 kBq/ml) almost reaches the peak activity value of the plaque from the scan without motions (15.2 kBq/ml). The activity profiles for dual-gated image 10, image without gating, and image from the scan without motions is presented in Figure 5-12. When analysing plaques, where the plaque-background-ratio was smaller, the maximum activity values for dual-gated images were also markedly higher than in the non-gated image. Axial motions of plaques were detectable between dual-gated images for every other plaque except the 1 kBq plaque, which was blurred by the coronary beside it. FWHM analysis showed that in the axial direction the width of the plaque is blurred the most, and the widening can be suppressed.
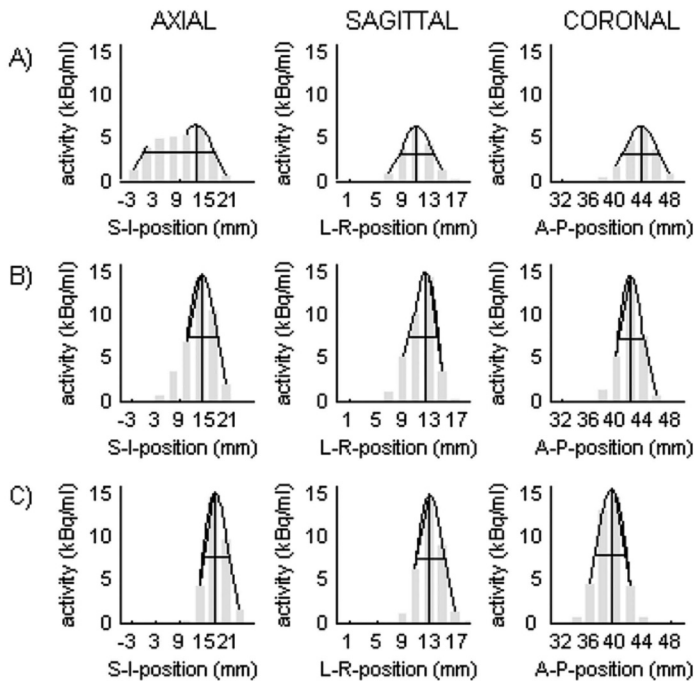
Figure 5-12. Activity profiles of a plaque in three orthogonal directions: (A) Non-gated image, (B) dual gate 10, (C) No-motion image. Peak activities (mean 14.8 kBq / ml) of dual-gated images show the increase in sensitivity when compared with the non-gated peak activities (mean 6.5 kBq / ml). The peak activities in dual-gated images and no-motion images are almost the same. Axial activity profiles of dual-gated images show a clearly decreased FWHM value of 7.6 mm when compared to the 17.8 mm value of the non-gated profile. Qualitatively, the activity profiles of the dual-gated image do not differ much from the profile of the no-motion image.

5.3.4. Minipig studies

Results from minipig studies are summarised in Figures 5-13 to 5-15. In general, the respiratory movement of the heart was small. With the RPM device the detected amplitude of the chest motion was around 0.9 mm – 1.3 mm. The contraction motion seen in the X-ray film from the angiolab showed that the tip was moving along with the contraction, and the small movement in the apico-cranial direction of the heart caused by respiration was in the apical part of the heart (snapshot in Fig. 5-13 left). In the CTA image series the catheter could be followed (snapshot in Fig. 5-13 right), and the place of the tip with the activity without background from two views can be seen in Figure 5-14.
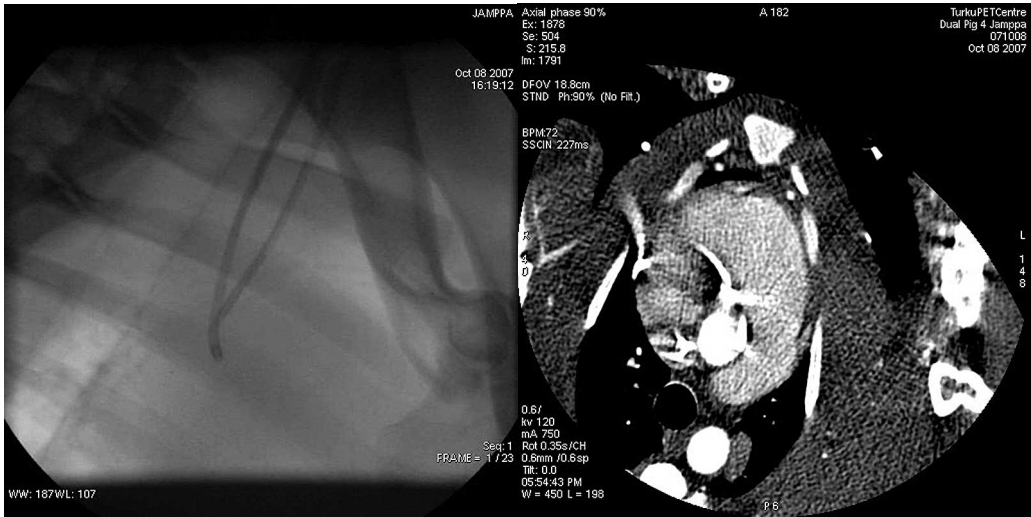
Figure 5-13. Snapshots from the X-ray angio (left) and CTA image series (right).
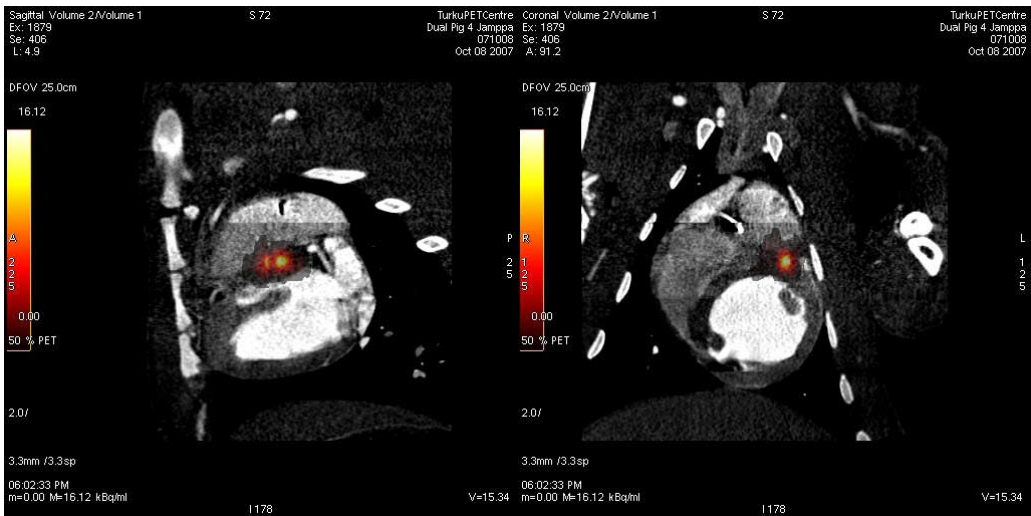
Figure 5-14. Two views localizing the radioactive tip of the catheter.

In PET images (Fig. 5-15), we see the effect of gating and comparison with the static no motion image of the sacrificed pig as the golden standard. The higher noise level of dual-gated images represents the lower statistics. The radioactive tip is blurred in the non-gated image. The radioactivity in the tip at the time of measurement is around 6 kBq, Results of profile measurements of the tip are shown in Figure 5-16. The best correlation is achieved in with the inspiration diastolic phase (dual gate 10, row A) when compared to the golden standard profile of the sacrificed pig (no motion, row D). The position of the tip is different because of muscle relaxation after death. Non-gated profiles (row C) have clearly flattened profiles with axial FWHM of 11.0 mm when compared to static (6.3 mm) or dual gates 10 and 12 (7.0 mm and 7.4 mm).

a)

b)

c)

d)
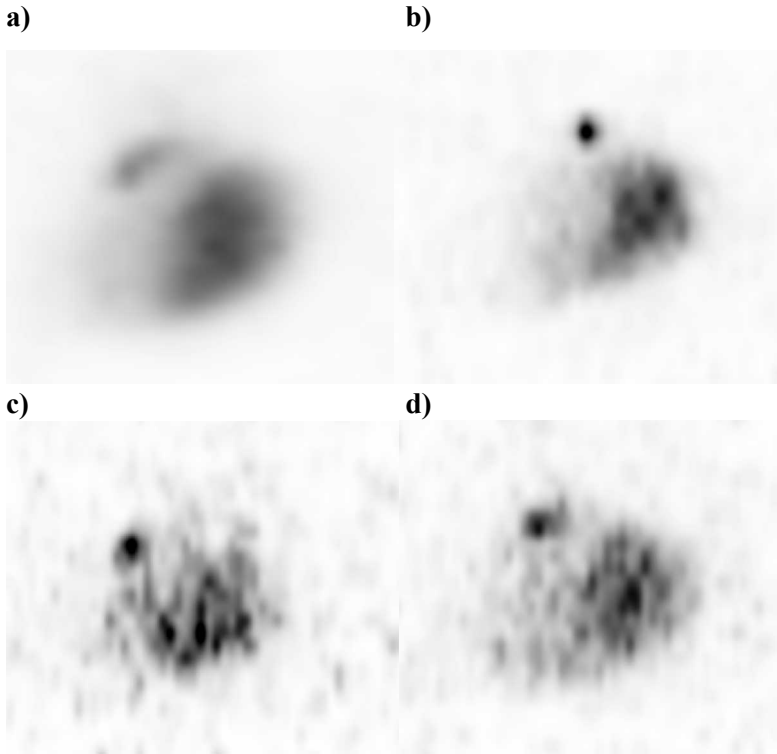
Figure 5-15. PET image of the heart of the minipig: **a)** non-gated image with all motion, **b)** static image after sacrificing the pig, **c)** dual gate 10 representing end-expiration systolic phase and **d)** dual gate 12 representing end-expiration diastolic phase
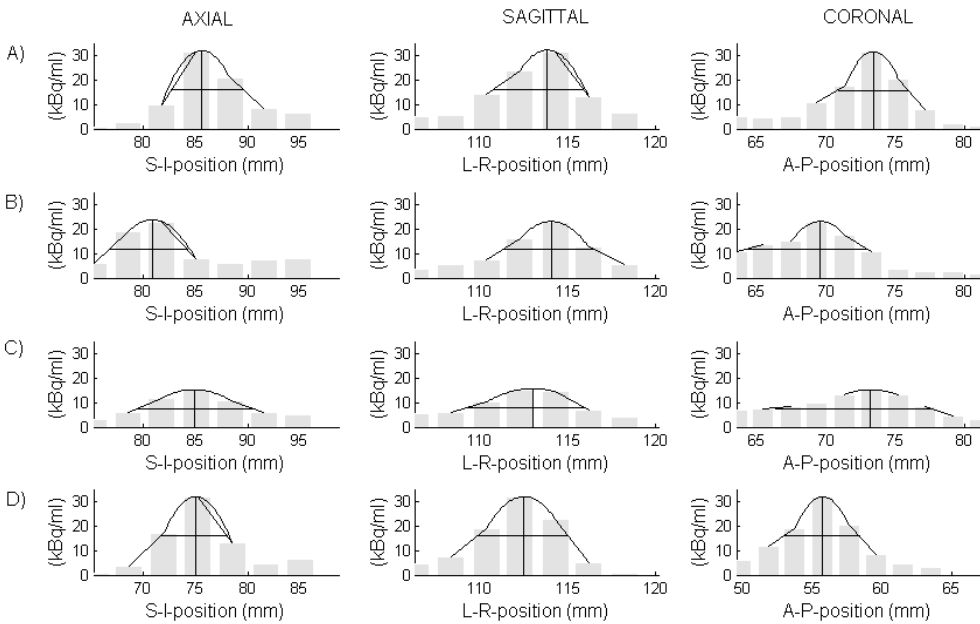
Figure 5-16. A) dual gate 10 (end-expiration systolic phase), B) dual gate 12 (end-expiration diastolic phase), C) non gated, and D) static no-motion image (the aim).

The dual-gated images have poorer statistical quality, which is obvious as the acquisition time of the non gated image is around 6 times longer than the longest dual-gated image.

5.3.5. Patient study

Results of the patient study are shown in Figures 5-17 to 5-20. In Figure 5-17 no-motion image is compared with the dual-gated image in full expiration and the diastolic phase. Images are scaled to the same activity concentration level and papillary muscles are visualised in the dual-gated image. The maximal respiratory movement was found to be 15 mm between full inspiration and full expiration in diastolic phases (Fig. 5-18), and maximal contraction motion between systolic and diastolic phases in full expiration was 7 mm (Fig. 5-19). The maximal movement of the wall of the myocardium was found to be 21 mm in the cranio-caudal direction.

It can also be noticed that the shape of the heart muscle is significantly changed between dual gates. In Figure 5-20, respiration data recorded with the RPM system are shown. Black (top) areas indicate inspiration, yellow (light grey), middle respiration, and green (dark grey, bottom), expiration phases. Small dots indicate trigger signals sent to the LM stream.
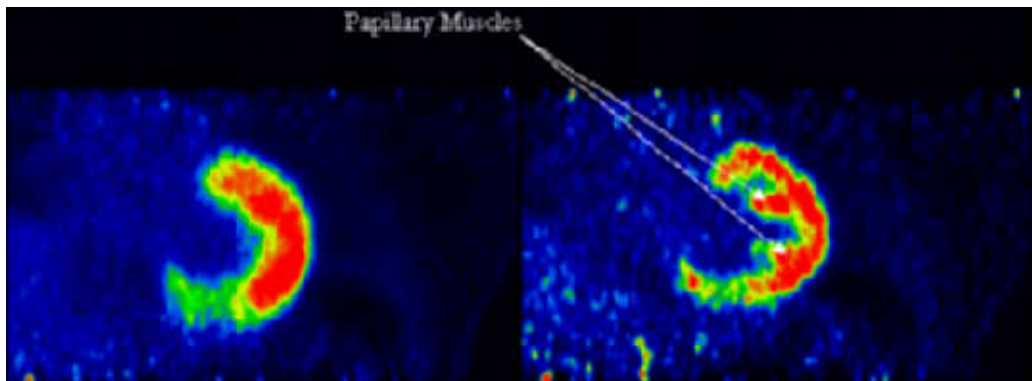
Figure 5-17. Comparison between the image with no-motion correction (left) and the dual-gated image in diastolic and full expiration phases (right). Both images are in coronal orientation and scaled at 17 kBq/ml. Papillary muscles are clearly visible in the dual-gated image
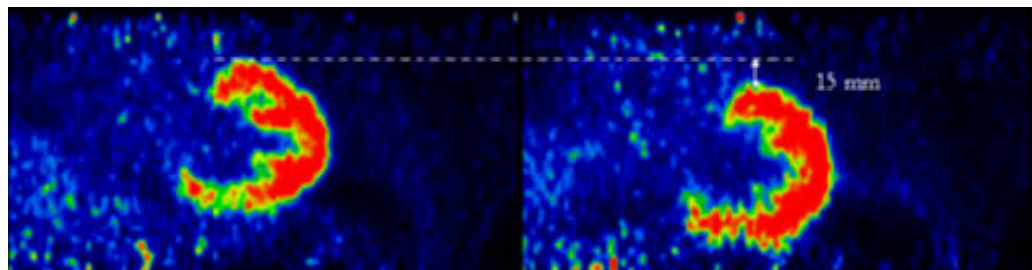
Figure 5-18. Respiratory motion between full inspiration (right) and full expiration (left) in diastolic phase dual-gated images
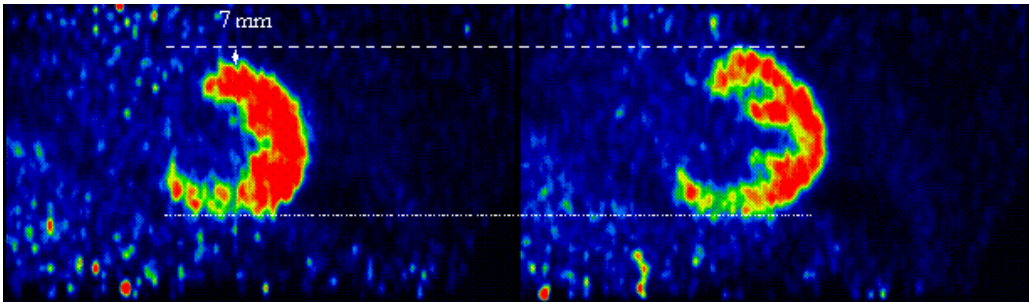
Figure 5-19. Contraction motion between diastolic (right) and late systolic (left) phases in full expiration dual-gated images.
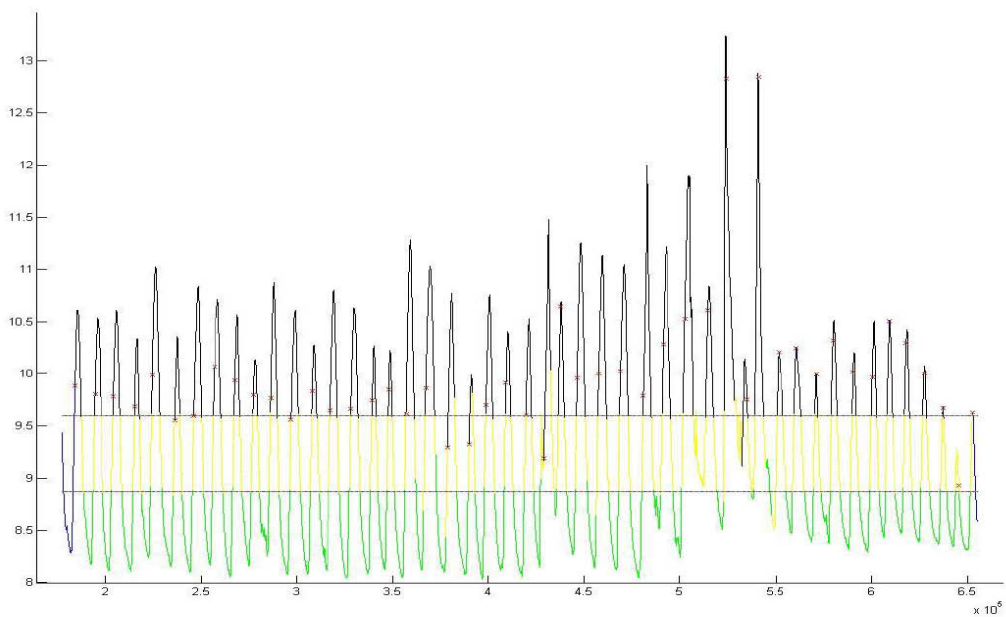
Figure 5-20. An example of RPM data. Black (top) represents inspiration, green (bottom) expiration and, yellow (middle) mid respiration.

6. DISCUSSION

6.1. Performance

6.1.1. Methods

The present NEMA standards, NU 2-1994 and NU 2-2001, do not meat the needs of present PET devices combined with a CT for attenuation correction. Moreover the main reconstruction algorithm is based on the iterative OSEM algorithm and NEMA standards refer to filtered backprojection algorithms that might not even be available in current scanners. Another feature not covered by the present standards is the intrinsic radioactivity of LSO and LYSO crystals. This affects the count rate tests where NEMA advises continuing until the randoms rate is less than 1% of true counts. This is never achieved with LSO and LYSO based scanners. Another problem related to the count rate test is that the NEC curve is very shape- and volume-dependent [Townsend et al. 1998, p118-120]. Also the activity outside the FOV decreases NEC and should be taken into account. In future, separate measurements might be needed for body and brain regions. The image quality test was designed to represent a routine clinical setting for acquisition times and reconstruction parameters. These settings have changed with the introduction of CT for attenuation correction and iterative reconstruction for a standard whole body PET study. Furthermore the resolution test in the axial direction suffers from poor sampling which, together with iterative reconstruction, gives results that are not comparable with different scanners. To overcome these problems, a new NEMA standard has been launched lately, but no further comments on it can be made at this moment. The new standard [National Elec. 2007] takes into account the intrinsic radioactivity of LSO and LYSO crystals, as well as the Time-of-Flight (TOF) capability.

6.1.2. Results

In the present study, we performed NEMA measurements in the new generation GE Discovery PET scanner. This PET scanner is available with 16-slice CT (STE) or 64-slice CT (VCT). The main improvement as compared with the previous generation PET scanner Discovery ST (ST) is in the BGO crystal design and the improved front-end electronics. The new crystal design increases the detector number per ring from 420 to 560, and this improved in-plane sampling should give better resolution. Electronic improvements make it possible to use a shorter coincidence window and a higher low-level discriminator setting. This improvement should give better scatter characteristics at the cost of sensitivity. In the Discovery RX (RX) with the new LYSO crystals, the main difference should be seen in count rate capabilities as the shorter coincidence timing window reduces the randoms coincidence rate. Comparison of the main NEMA NU-2 2001 performance values in 3D mode on the GE ST, STE/VCT (lld 425 keV) and RX are summarised in Table 7 (article I). More results concerning the performance of different scanners not compared here can be found from Surti et al. [2007] and Brambilla et al. [2006].

The spatial resolution of this new system is improved compared with the ST. The 2D transaxial resolution (average radial and tangential FWHM) at 1 cm off centre (R1) in the new scanner is 4.9 mm, while it was 6.28 mm [Kemp et al. 2006] or 6.1 mm [Humm et al. 2003] in the ST, and 5.1 mm in the RX [Karp 2002]. At 10 cm off centre (R10), the spatial resolution is slightly reduced, but still the transaxial resolution is improved (radially 5.7 mm and tangentially 5.8 mm) as compared with the resolution in the ST (radially 6.7−6.9 mm and tangentially 6.8−7.0 mm). The RX showed comparable results with our measurements (radially 5.9 mm and tangentially 5.1 mm).

The axial sampling was not changed between the ST and the new designs (VCT and RX) but still some improvement was detected. At R1, axial resolution was 4.4 mm in the VCT, 4.6 mm in the ST [Kemp et al. 2006] and 4.8 in the RX [Karp 2002]. At R10 the corresponding values were 6.0 mm, 6.1 mm and 6.3 mm. The VCT axial resolution in 2D was also measured with the NEMA NU-94 method since we believe that the axial sampling with a slice thickness of 3.27 mm used in the NEMA NU-01 method is insufficiently accurate. The axial resolution results obtained from the NU-94 were 4.4 at R1 and 5.5 at R10. Thus, there is a slight improvement in axial resolution when compared with the ST or RX. In 3D mode, the improvement in transaxial resolution in the VCT as compared with the ST is from 6.3 mm to 5.1 mm at R1, and from 7.0 mm to 5.9 mm (radial) and from 6.6 mm to 5.5 mm (tangential) at R10. The RX gives a transaxial resolution of 5.0 mm at R1 and 5.9 mm (radial) and 5.2 mm (tangential) at R10. Axial resolution improvement in the VCT as compared with the ST in 3D mode is from 5.7 mm to 5.2 mm at R1, and from 6.0 mm to 5.9 mm at R10. The corresponding values in the RX are 5.8 mm and 6.5 mm. The improvements in FWTM are of the same magnitude as those in FWHM.

The sensitivity in 2D in R0 and R10 was 2.3 cps/kBq, compared with 1.9 and 1.7 cps/kBq with the ST and the RX, respectively. In 3D mode, sensitivity was measured with different lld and coincidence timing settings. Results with settings comparable to the ST (lld 375 keV and coincidence timing window set to 11.7 ns) at R0 (R10) were 9.3 (9.7) cps/kBq vs 9.0 (9.3) cps/kBq. If the discriminator was set to 425 keV and coincidence timing to 9.3 ns, the sensitivity decreased to 8.8 (8.9) cps/kBq. The result was still good and quite comparable to the ST. In the RX, the sensitivity in 3D was 7.3 (7.5) cps/kBq at R0 (R10). As the lld in the RX and VCT is the same, the difference mainly derives from the different scintillation material.

The scatter fraction in the new system using an lld of 375 keV is 21 % for 2D and 45% for 3D. The previously reported values for the ST were 19% and 45%, respectively. The shift of lld value to higher energy at 425 keV reduces the scatter fraction in 3D mode to 34%, compared with 32% in the RX.

Count rate performance in 2D was measured with an lld value of 375 keV. The 2D peak NEC (k=1) rate was 85 kcps at 44 kBq/ml in our study, which is better than the corresponding value for the ST (81 kcps at 64 kBq/ ml). Our measurements in 3D were highly dependent on the chosen lld value, but using the value that is applied in clinical studies (425 keV), the NEC rate of 67.6 kcps at 12.1 kBq/ml is comparable to the ST value of 66 kcps at 15 kBq/ml obtained with the lower lld value (375 keV). The main

benefit in the RX is seen in the count rate capabilities, where the NEC (k=1) rate in 2D (3D) was 160 kcps at 92 kBq/ml (120 kcps at 22 kBq/ml).

The maximum error for count losses and randoms for 2D and 3D was 1.3% and 1.9%, respectively.

The image quality test with the new system showed comparable results in 3D hot and 2D cold sphere contrasts when compared with the ST. Results for cold sphere contrast in 3D and hot sphere contrast in 2D were slightly poorer than with the ST, while the background variability was similar. The largest difference was in the average lung residual error, which in the new system was around 30%, whereas in the ST it had been 17% in 3D, and 24% in 2D.

This difference might be due to a new ML-OSEM reconstruction algorithm that has been analysed elsewhere [Seppänen et al. 2006]. It is generally known that low-activity areas need more iterations for convergence but this typically leads to a higher noise level. This could also be seen in our experiment, where the lung residual error decreased from 30% to 22%, but at the expense of background variability by increasing the number of iterations. The largest increases were seen in the smallest spheres, from 6% to 21% in 2D, and from 5% to 13% in 3D.

Another typical problem in the image quality test arises when the pixel size is close to the sphere size. When increasing the image matrix from 128×128 (pixel size 5.47 mm) to 256×256 (pixel size 2.74 mm), the smallest hot sphere contrast increased significantly. These results indicate that to improve detection of cold lesions, a higher number of iterations and a larger matrix size should be considered.

6.1.3. PET/CT image co-registration

For accurate quantitative results in PET imaging of the thoracic region, proper co-registration of CT and PET images is essential. In oncological applications such as lung nodule staging, average CT [Pan et al. 2006] or breath hold in both CT and PET [Nehmeh et al. 2007] might be sufficient techniques for good co-registration although they induce artefacts, mainly above the diaphragm where the lung motion is large and around the heart. One simple way to overcome the false positive diagnosis caused by the mis-registration is to reconstruct images without attenuation correction to verify whether lesions are visible. In cardiac applications the quantitative analysis is needed for the whole myocardium (including coronary plaques). The spillover between heart and lung and liver requires proper co-registration. The way to do this is to use respiratory gating in both CT and PET.

6.2. PVC

The main purpose of PVC is to improve the quantitative characteristics of PET images. The effect of PVC for a single scanning session was tested with a phantom object, with the focus on the mean values of ROIs before and after the PVC. The results of these experiments were generally as expected concerning the increase in radioactivity values; the difference in ROI mean values before and after the correction operation follows the

results reported earlier [Meltzer et al. 1999, Quarantelli et al. 2004, Slifstein et al. 2001]. The situation deviates strongly from the above when the interest is especially on PVE-corrected images [Boussion et al. 2006]. While the voxel-based PVC methods provide more possibilities for further PET analyses, they are not very robust to noise. As can be seen from the results of the phantom tests (Table 5-5 and Fig. 5-8), the standard deviation of voxel values increases with the mean radioactivity values. This affects the calculation of the [^{11}C]raclopride BP in the present findings. With the test-retest data on humans, the M-PVC method was the only method which did not decrease the ICC values in any tested region. The main observation was that it is difficult to correct PVE with high radioactivity restoration, while at the same time keeping the standard deviation low. No single method performed better than the others in all aspects. To choose the most suitable PVC method, a compromise must be made between radioactivity restoration and the reproducibility and reliability of PET scans. Some issues related to choosing the PVC method are discussed in the following in more detail.

6.2.1. Quantification

In the phantom tests of the present study, the true mean radioactivity magnitude restoration was smaller with M-PVC than with the other three methods. Moreover, the t-test between the mean BP values in the caudate and lateral thalamus regions with M-PVC did not indicate significant difference from non-corrected BP values. Therefore the following conclusions for A-PVC, R-PVC and MG-PVC can be drawn:

- A-PVC produced the best mean radioactivity restoration so this method could be used to look for PVE-corrected mean radioactivity values without further voxel-based image analysis or reproducibility.

- R-PVC gave weaker radioactivity restoration than A-PVC for the phantom. With the GE Advance PET, it was seen to produce uniform ICC values between the studied regions. This method could be useful when only the mean radioactivity value of the region is used, and both radioactivity value restoration and reproducibility are needed.

- MG-PVC could be considered a compromise between A-PVC, which is quantitatively accurate, and M-PVC, that better preserves the voxel characteristics in ROIs. MG-PVC is robust to errors in WM estimation, so that either R-WME or A-WME could be used as its WM estimator.

Important issues in the calculation of the ROI mean value by A-PVC or MG-PVC are the volume of ROI and its vicinity to the GM border. The former affects the mean sensitivity and the latter the increases in local radioactivity variation due to the noise amplification in PVC. Because ROIs often tend to lie at the border of GM, this becomes an issue. On the other hand, when ROIs contain voxels from WM the estimation of the radioactivity values of WM voxels may crucially affect the usability of A-PVC and MG-PVC. In order to include the WM voxels in a ROI, the estimated WM mean values may be used as corrected values of the WM voxels. Another alternative is to exclude the non-corrected voxels of ROIs when the number of

remaining voxels is reasonable, as was the case in the present study. In contrast, the R-PVC method does not suffer from such a weakness. The M-PVC method solves the issue by not using the border between GM and WM.

6.2.2 Test-retest

Not only the capability of restoring the mean radioactivity values in ROIs, but also the reproducibility and reliability are essential properties of PET. This role should be underlined in studies where the same subject is scanned multiple times. Then, if all true PVE were corrected by a PVC method, the ICC values would be at least the same as without correction. If the BP values remain the same with correction as without it, PVC naturally has no effect on ICC values, and the observed variance between scans is due to other factors, such as biological variability. When ICC values decrease as a result of PVC, the reason might be that the correction has added additional variability between the scans. On the basis of the results of the test-retest experiment (Table 5-6), M-PVC is more robust as regards the ICC values; the region of the medial thalamus posed a challenge to all other PVC methods. When the image intensity values approach some constant value, the characteristic numbers of the reproducibility test automatically approach their optimal values (std and variability tend toward zero and ICC toward 100%). Because of this, quantification tests should be carried out in conjunction with the reproducibility test. From the phantom test (Table 5-5) it was observed that the M-PVC method overestimates the radioactivity in the WM region, and this can affect the ICC values of the thalamus regions. However, the effect is expected to be small especially for the medial thalamus, since it is located mainly in the GM region. Therefore, on the basis of the experiment, we conclude that the M-PVC method is the preferred choice for human studies in which individual subjects are scanned repeatedly. This conclusion, however, includes the assumption that less radioactivity value restoration is acceptable.

6.3. Dual gating

The robust dual gating method with the developed algorithm shows that detection of cardiac motion is feasible. The rotating phantom study showed that the algorithm is reliable for separating the measured coincident events into the expected 12 spatially different locations when the motion of the target is known. Some axial overlapping was seen between dual-gated images from different axial phases, mostly due to target size (5 mm length in axial direction) and the PSF (Point Spread Function) of the PET scanner.

The heart phantom study showed that it is feasible to detect the motion of the coronary plaque. The contraction motion of the surface of the heart phantom was only 7 mm, whereas the real contraction motion of epicardial surfaces and coronaries is reported to be 9 to 13 mm [Slomka et al 2004, Wang et al. 1999]. We were able to detect 51 % (3.6 mm) of the total contraction motion. Detection of maximal contraction motion of the plaque was not totally attainable because of plaque size (3 mm diameter), and voxel size (3.3 mm x 2.0 mm x 2.0 mm) in the analysis, cardiac phasing and spatial resolution of the PET/CT scanner (5-6 mm). The selected number

of cardiac phases seems to be enough to detect maximal cardiac motion with current analysis accuracy and spatial resolution because the plaque size (FWHM in sagittal and coronal directions) and peak activity value in the dual-gated image from the diastolic phase (delay phase = no motion) was almost the same as in the no-motion situation, and did not show any benefit when compared to other dual-gated images of the plaque from different cardiac phases (including contraction motion). This can be read so that motions inside cardiac phases are so small that detection of them is not possible with the current PET/CT scanner and analysing methods. We were not able to totally reach the FWHM value of the plaque in the axial direction when compared to the no-motion image, thus implying that respiratory motion elimination can be improved by adding more respiratory phases.

Amplitude-based respiratory gating did not causes any problems in the heart phantom study but, in patient studies, the baseline shift might cause some problems when determining respiratory gates. One way to overcome this is to increase the respiratory phases from three, which may also benefit the respiratory motion elimination. According to Visvikis et al. [2006], respiratory synchronised acquisitions are moving from being a research subject into routine clinical practice, but the development of respiratory motion correction algorithms to make use of all available data throughout a respiratory average emission acquisition is limited. Such approaches can be broadly divided into two distinct categories: namely those which are applied either in the raw data domain or during the image reconstruction process, and those, which are applied post-reconstruction [Dawood et al. 2006, Lamare et al. 2007, 2008]. To sum up, respiratory phases after movement correction will recover most of the statistics and, thus, the actual acquisition time could be shortened.

7. CONCLUSION

7.1 PET performance of DVCT

The PET scanner in the GE Discovery STE/VCT with newly designed BGO crystals has improved spatial resolution compared with the previous model, Discovery ST. The Discovery RX like other LSO or LYSO scanners shows much better NEC rate values and this is useful in high-count rate studies, such as heart perfusion studies in 3D. In whole body studies the count rates are typically much lower and the sensitivity is a more important parameter. The physical performance measured with NEMA standards of the latest generation whole body scanners of all manufacturers are quite similar. Special attention, apart from physical performance, should also be directed to reconstruction methods and parameters, as well as to image co-registration between different modalities The most promising way of improving the performance is to incorporate partial volume correction into the reconstruction. A need for a revised version of performance measurement standards is valid after the introduction of CT attenuation correction, new crystal materials and iterative reconstruction methods.

7.2 PVC

Four PVC methods (M-PVC, MG-PVC, R-PVC, A-PVC), and three WM estimation methods (CS, A-WME, R-WME) were tested in order to evaluate their performance in studies of WM/GM radioactivity measurements. The main observation was that with the sophisticated A-PVC method, PET accuracy was improved the most. This is useful when activity values of ROIs are compared between study groups. Although M-PVC had weaker single study accuracy, it improved or maintained tomograph reliability even in regions where other methods failed (caudate, putamen, medial thalamus). This property is beneficial in test-retest study designs such as drug effect studies. In general all methods compared here were based on MR segmentation and the assumption of homogenous activity distribution within segments. This limits the use of these methods in the brain, and is most reliable in larger brain structures such as the caudate and putamen. New correction methods without anatomical a priori, are under intensive research and will be available in the near future. These methods work on a pixel by pixel basis and can be used in all parts of the body.

7.3 Dual gating method

The dual gating method presented worked well with phantom studies. Preliminary human data warrant continuing the work with a research project for detecting vulnerable coronary plaques. In such work, the optimisation of the number of respiratory gates and correction for respiratory movement should be addressed. Furthermore, implementation of partial volume correction for improving quantitative value is needed. With these improvements the method of dual gating has the potential of becoming a clinical tool in cardiac PET in patients suffering, e.g. from acute myocardial infarction.

ACKNOWLEDGEMENTS

REFERENCES

[Adam et al. 2001] Adam L-E, Karp JS, Daube-Witherspoon ME, Smth RE: Performance of a Whole-Body PET Scanner Using Curve-Plate NaI(Tl) Detectors. J Nucl Med, 42:1821-1830, 2001.

[Alessio et al. 2006] Alessio AM, Kinahan PE, Lewellen TK: Modelling and incorporation of system response function in 3-D whole body PET. IEEE Trans Med Imaging, 25:828-837, 2006

[Alfano et al. 2004] Alfano B, Quarantelli M, Comerci M, Brunetti A, Salvatore M: A new method for voxel-based partial volume effect correction. Conference of functional mapping of the human brain, HBM Poster #TH360, 2004.

[Assie et al. 2004] Assie K, Breton V, Buvat I, Comtat C, Jan S, Krieguer M, Lazaro D, Morel C, Rey M, Santin G, Simon l, Staelens S, Strul D, Vieira JM, Walle RV: Monte Carlo simulation in PET and SPECT instruentation using GATE. Nucl Instruments Met Phys Res, 527:180-9, 2004.

[Aston et al. 2002] Aston JA, Cunningham VC, Asselin MC, Hammers A, Evans AC, Gunn RN: Positron emission tomography partial volume correction: Estimation and algorithms. J Cereb Blood Flow Metab, 22:1019-34, 2002.

[Avril et al. 1997] Avril N, Bense S, Ziegler SI, Dose J, Weber W, Laubenbacher C, Römer W, Jänicke F, Schwaiger M : Breast imaging with fluorine-18-FDG PET : Quantitative image analysis. J Nucl Med, 38:1186-1191, 1997.

[Bacharach et al. 2003] Bacharach SL, Bax JJ, Case J, Delbeke D, Kurdziel KA, Martin WH, Patterson RE: PET myocardial glucose metabolism and perfusion imaging: Part 1-Guidelines for data acquisition and patient preparation. J Nucl Cardiol, 10:543-556,2003.

[Bailey et al., 1991a] Bailey DL, Jones T, Spinks TJ, Giraldi MC, Townsend DW: Noise equivalent count measurements in Neuro-PET scanner with retractable septa. IEEE Trans Med Imag, 10:256-260, 1991.

[Bailey et al. 1991b] Bailey DL, Jones T and Spinks TJ: A method for measuring the absolute sensitivity of poritron emission tomographic scanners. Eur J Nucl Med, 18:374-379, 1991.

[Bettinardi et al. 2004] Bettinardi V, Danna M, Savi A, Lecchi M, Castiglioni I, Gilardi MC, Bammer H, Lucignani G, Fazio F: Performance evaluation of the new whole-body PET/CT scanner: Discovery ST. Eur J Nucl Med Mol Imaging, 31:867-881, 2004.

[Boussion et al. 2006] Boussion n, Hatt M, Lamare F, Bizais Y, Turzo A, Cheze-Le Rest C, Visvikis D: A multiresolution image based approach for correction of partial volume effects in emission tomography. Phys Med Biol, 51:1857-76, 2006.

[Brambilla et al. 2005] Brambilla M, Secco C, Dominietto M, Matheoud R, Sacchetti G, Inglese E: Performance characteristics obtained for a new 3-dimensional Lutetium Oxyorthosilicate-based whole-body PET/CT scanner with the national electrical manufacturers association NU 2-2001 standard. J Nucl Med, 46:2083-2091, 2005.

[Budinger et al. 1998] Budinger TF: ^{18}F-FDG PET Instrumentation: What are the limits? Seminars in nuclear medicine, Vol XXVIII: 247-267, 1998.

[Chawluk et al. 1987] Chawluk JB, Alavi A, Dann R, Hurtig HI, Bais S, Kushner MJ, Zimmerman RA, Reivich M: Positron emission tomography in aging and dementia: effect of cerebral atrophy. J Nuc Med, 28:431-7, 1987.

[Danias et al. 1999] Danias PG, Stuber M, Botnar RM, Kissinger KV, Edelman RR, and Manning WJ: Relationship between motion of coronary arteries and diaphragm during free breathing: lessons from real-time MR imaging. Am J Roentgenol, 172:1061-1065, 1999.

[Daube-Witherspoon et al. 2002] Daube-Witherspoon ME, Karp JS, Casey ME, DiFilippo FP, Hines H, Muehllehner G, Simcic V, Stearns CW, Adam LE, Kohlmeyer S, Sossi V: PET performance measurements using the NEMA NU 2-2001 standard. J Nucl Med, 43:1398-1409, 2002.

[Dawood et al. 2006] Dawood M, Lang N, Jiang X, Schäfers KP: Lung motion correction on respiratory gated 3-d PET/CT images. IEEE Trans Med Imaging, 25:476-485, 2006.

[Durand-Schaefer 2008] Durand-Schaefer N. Master Thesis, Kungliga Tekniska Högskolan, Stockholm, Sweden, May 2008.

[Erdi et al] Erdi YE, Nehmeh SA, Pan T, Pevsner A, Rosenzweig KE, Mageras G, Yorke ED, Schoder H, Hsiao W, Squire OD, Vernon P, Ashman JB, Mostafavi H, Larson SM, Humm JL: The CT motion quantitation of lung lesions and its impact on PET-measured SUVs. J Nucl Med, 45:1287-1292, 2004.

[Frouin et al. 2002] Frouin V, Comtat C, Reilhac A, and Grégoire M-C: Correction of partial-volume effect for PET striatal imaging: Fast implementation and study of robustness. J Nucl Med, 43:1715–1726, 2002.

[Geworski et al. 2000] Geworski L, Knoop BO, Levi de Cabrejas M, Knapp WH, Munz DL: Recovery correction for quantitation in emission tomography: feasibility study. Eur J Nucl Med, 27:161-169, 2000.

[Gould et al. 2007] Lance Gould K, Pan T, Loghin C, Johnson NP, Guha A, Sdringola S: Frequent diagnostic errors in cardiac PET/CT due to misregistration of CT attenuation and emission PET images: A definitive analysis of causes, consequences and corrections. J Nucl Med, 48: 1112-1121, 2007.

[Guivarc'h et al. 2004] Guivarc'h O, Turzo A, Visvikis D, Bizais Y: Synchronization of pulmonary scintigraphy by respiratory flow and by impedance plethysmography. Proc SPIE Med Imag, 5370:1166-1175, 2004.

[Hawkes et al. 2003] Hawkes DJ, Hill DL, Hallpike L, Bailey DL: coregistration of structural and functional images. In Valk P, Bailey DL Townsend DW, Maisey M

eds. Positron emission tomography: Basic science and clinical practise. New York, NY: Springer-Verlag, 181,198, 2003.

[Herscovitch et al.1986] Herscovitch P, Auchus AP, Gado M, Chi D, Raichle ME: Correction of positron emission tomography data for cerebral atrophy. J Cereb Blood Flow Metab, 6:120-124, 1986.

[Hickeson et al. 2002] Hickeson M, Yun M, Matthies A, Zhuang H, Adam LE, Lacorte L, Alavi A: Use of corrected standardized uptake value based on the lesion size on CT permits accurate characterization of lung nodules on FDG-PET. Eur J Nucl Med, 29:1639-1647, 2002.

[Hirvonen et al. 2003] Hirvonen J, Aalto S, Lumme V, Någren K, Kajander J, Vilkman H, Hagelberg N, OikonenV, Hietala J: Measurement of striatal and thalamic dopamine D2 receptor binding with 11C-raclopride. Nucl Med Comm, 24:1207-1214, 2003.

[Hoffman et al. 1979] Hoffman EJ, Huang SC and Phelps ME: Quantitation in positron emission computerised tomography 1. Effect of object size. J Comput Assist Tomogr, 3:299-308, 1979.

[Humm et al. 2003] Humm JL, Rosenfeld A, Del Guerra A: From PET detectors to PET scanners. Eur J Nucl Med Mol Imaging, 30:1574–97, 2003.

[Hutton et al. 2003] Hutton BF and Braun M: Software for image registration techniques. J Comput Assist Tomogr, 33:180-192, 2003.

[International Elec. 1998] International Electrotechnical Commission. EC Standard 61675-1: Radionuclide Imaging Devices – Characteristics and Test Conditions. Part I. Positron Emission Tomographs. Geneva, Switzerland: International Electrotechnical Commission, 1998.

[Karp et al. 1991] Karp JS, Daube-Witherspoon ME, Hoffman EJ, Lewellen TK, Links JM, Wong WH, Hichwa RD, Casey ME, Colsher JG, Hitchens RE, Muehllehner G, Stoub EW: Performance Standards on Positron Emission Tomography. J Nucl Med, 32:2343-2350, 1991.

[Karp 2002] Karp JS: Is LSO the future of PET? Against. Eur J Nucl Med Mol Imaging, 29:1525–1528, 2002.

[Kemp et al. 2006] Kemp BJ, Kim C, Williams JJ, Ganin A, Lowe VJ: NEMA NU 2-2001 performance measurements of an LYSO-based PET/CT system in 2D and 3D acquisition modes. J Nucl Med, 47:1960–7, 2006.

[Kim et al. 2005] Kim JH, Czernin J, Allen-Auerbach MS, Halpern BS, Fueger BJ, Hecht JR, Ratib O, Phelps ME, Weber WA: Comparison between ^{18}F-FDG PET, in-line PET/CT and software fusion for restaging of recurrent colorectal cancer. J Nucl Med, 46:587-595, 2005.

[Klein et al. 1997] Klein GJ, Reutter BW, Huesman RH: Non-rigid summing of gated PET via optical flow. IEEE Trans.Nucl. Sci., 44:1509-1512, 1997.

[Klein et al. 1998] Klein GJ, Reutter BW, Ho MH, Reed JH, Huesman RH: Real-time system for respiratory-cardiac gating in positron tomography. IEEE Trans Nucl Sci, 45:2139-2143, 1998.

[Labbé et al. 1996] Labbé C, Froment JC, Kennedy A, Ashburner J, Cinotti L: Positron Emission Tomography metabolic data corrected for cortical athropy using magnetic resonance imaging. Alzheimer disease and associated disorders. 10:141-170, 1996.

[Labbé et al. 1998] Labbé CC, Koepp M, Ashburner J, Spinks T, Richardson M, Duncan J, Cunningham V: Absolute PET quantitation with correction for partial volume effects within cerebral structures. In Carson RE, Daube-Whitherspoon ME eds. Quantitative Functional brain imaging with positron emission tomography. San Diego, CA: Academic Press, 59-66, 1998.

[Lamare et al. 2007] Lamare F, Cresson T, Savean J, Cheze Le Rest C, Reader AJ, Visvikis D: Respiratory motion correction for PET oncology application using affine transformation list mode data. Phys Med Biol, 52:121-140, 2007.

[Lamare et al. 2008] Lamare F, Teras M, Kokki T, Fayad H, Knuuti J, Visvikis D: Correction of respiratory motion in dual gated PET cardiac imaging. SNM Annual meeting, New Orleans, 2008. (abstract).

[Lammertsma et al. 1996] Lammertsma AA, Hume SP: Simplified Reference Tissue Model for PET Receptor Studies. Neuroimage, 4:153-158, 1996.

[Lang et al. 2006] Lang N, Dawood M, Büther F, Schober O, Schäfers M, Schäfers K: Organ movement reduction in PET/CT using dual-gated listmode acquisition. Z Med Phys, 16:93-100, 2006.

[Links et al. 1996] Links JM, Zubieta JM, Meltzer CC, Stumpf MJ, Frost JJ: Influence of spatially heterogeneous background activity on "Hot Object" quantitation in brain emission computed Tomography. J Comput Assist Tomogr, 20:680-687, 1996.

[Livieratos et al. 2006] Livieratos L, Rajappan K, Stegger L, Schafers K, Bailey DL and Camici PG: Respiratory gating of cardiac PET data in listmode acquisition. Eur J Nucl Med Mol Imaging, 33:584–588, 2006.

[Martinez-Möller et al. 2007b] Martinez-Möller A, Zikic D, Botnar RM, Bundschuh RA, Howe W, Ziegler SI, Navab N, Schwaiger M, Nekolla SG: Dual cardiac-respiratory gated PET: implementation and results from a feasibility study. Eur J Nucl Med Mol Imaging, 34:1447-1454, 2007.

[Mawlawi et al. 2004] Mawlawi O, Podoloff DA, Kohlmeyer S, Williams JJ, Stearns CW, Culp RF, Macapinlac H: Performance characteristics of a newly developed PET/CT scanner using NEMA standards in 2D and 3D modes. J Nucl Med, 45:1734-1742, 2004.

[Mazziotta et al. 1981] Mazziotta JC, Phelps ME, Plummer D and Kuhl D: Quantitation in positron emission tomography: 5. physical-anatomical factors. J Comput Assist Tomogr, 5:734-743, 1981.

[Meltzer et al. 1999] Meltzer CC, Kinahan PE, Greer PJ, Nichols TE, Comtat C, Cantwell MN, Lin MP, Price JC: Comparative evaluation of MR-based partial volume correction schemes for PET. J Nucl Med, 40:2053-2065, 1999.

[Mintun et al. 1984] Mintun MA, Raichle ME, Kilbourn MR, Wooten GF, Welch MJ: A quantitative model for the in vivo assessmet of drug binding sites with positron emission tomography. Ann Neur, 15:217-227, 1984.

[Moses et al. 1993] Moses W, Derenzo S: Empirical observation of resolution degradation in positron emission tomographs utilising block detectors [abstract]. J nucl Med 34(suppl):101P, 1993.

[Muehllehner et al. 1981] Muehllehner G, Wake RH, Sano R: Standards for performance of scintillation cameras. J Nucl Med, 22:72-77, 1981.

[Müller-Gärtner et al. 1992] Müller-Gärtner HW, Links JM, Prince JL, Bryan RN, McVeigh E, Leal JP, Davatzikos C, Frost JJ: Measurement of radiotracer concentration in brain gray matter using positron emission tomography: MRI-based correction for partial volume effects. J Cer Blood Flow and Met, 12:571-583, 1992.

[National elec. 1994] National Electrical Manufacturers Association. NEMA NU-2 Standards Publicaton NU-2-1994: "Performance measurements of positron emission tomography". Washington DC: National Electrical Manufacturers Association, 1994.

[National elec. 2001] National Electrical Manufacturers Association. NEMA NU-2 Standards Publicaton NU-2-2001: "Performance measurements of positron emission tomography". Rosslyn, VA: National Electrical Manufacturers Association, 2001.

[National elec. 2007] National Electrical Manufacturers Association. NEMA NU-2 Standards Publicaton NU-2-2007: "Performance measurements of positron emission tomographs". Rosslyn, VA: National Electrical Manufacturers Association, 2007.

[National elec. 2008] National Electrical Manufacturers Association. NEMA NU-4-2008:" Performance Measurements of Small Animal Positron Emission Tomographs", Draft 2008-01-24.

[Nehmeh et al. 2002a] Nehmeh SA, Erdi YE, Ling CC, Rosenzweig KE, Sguire OD, Braban LE, Ford E, Sidhu K, Mageras GS, Larson SM, Humm JL: Effect of respiratory gating on reducing lung motion artefacts in PET imaging of lung cancer. Med Phys, 29:366-371, 2002.

[Nehmeh et al. 2002b] Nehmeh SA, Erdi YE, Ling CC, Rosenzweig KE, Schoder H, Larson SM, Macapinlac HA, Squire OD and Humm JL: Effect of respiratory gating on quantifying PET images of lung cancer. J Nucl Med, 43:876–881, 2002.

[Nehmeh et al 2003] Nehmeh SA, Erdi Y, Rosenzweig KE, Schoder H, Larson SM, Squire OD, Humm JL: Reduction of respiratory motion artefacts in PET imaging of lung cancer by respiratory correlated dynamic PET: Methodology and comparison with respiratory gated PET. J Nucl Med, 44:1644-1648, 2003.

[Nehmeh et al. 2007] Nehmeh SA, Erdi YE, Meirelles GSP, Squire O, Larson SM, Humm JL, Schöder H: Deep-inspration breath-hold PET/CT of the thorax. J Nucl Med, 48:22-26, 2007.

[Nyquist 1928] Nyquist H: Certain topics in telegraph transmission theory, Trans. AIEE, 47:617-644, 1928

Reprint as classic paper in: *Proc. IEEE, Vol. 90, No. 2, Feb 2002*

[Paans] Paans A, Doctoral Thesis, Groningen University, The Netherlands, 1983.

[Pan et al. 2006] Pan T, Mawlawi O, Luo D, Liu HH, Chi Pm, Mar MV, Gladish G, Truong M, Erasmus Jr J, Liao Z, Macapinlac HA: Attenuation correction of PET cardiac data with low-dose average CT in PET/CT. Med Phys, 33, 3931-3938, 2006.

[Panin et al. 2006] Panin VY, Kehren F, Michel C, Casey M: Fully 3-D PET reconstruction with system matrix derived from point source measurements. IEEE Trans Med Imaging, 25:907-921, 2006.

[Paul et al. 2004] Paul AK and Nabi HA: Gated myocardial perfusion SPECT: Basic principles, technical aspects, and clinical applications. J Nucl Med Tech, 32:179-187, 2004.

[Quarantelli et al. 2004] Quatarelli M, Berkouk K, Prinster A, Landeau B, Svarer C, Balkay L, Alfano B, Brunetti A, Baron J-C, Salvatore M: Integrated software for the analysis of brain PET/SPECT studies with partial volume effect correction. J Nucl Med, 45:192-201, 2004.

[Rousset et al. 1998a] Rousset OG, Ma Y, Evans AC: Correction for partial volume effects in PET: principle and validation, J Nucl Med, 39(5):904-911, 1998.

[Rousset et al. 1998b] Rousset OG, Yilong MA, Wong DF, Evans AC: Pixel versus region based partial volume correction in PET. In Carson RE, Daube-Whitherspoon ME eds. Quantitative Functional brain imaging with positron emission tomography. San Diego, CA: Academic Press, 67-81, 1998.

[Rousset et al. 2000] Rousset OG, Deep P, Kuwabara H, Evans AC, Gjedde AH, Cumming P: Effect of partial volume correction on estimates of the influx and cerebral metabolism of 6-[18F]fluoro-L-dopa studied with PET in normal control and Parkinson's disease subjects. Synapse, 37:81–89, 2000.

[Sabins 1987] Sabins FF: Remote Sensing, Principles and Interpretation.W.H. Freeman and Company, New York, 1987.

[Schwartz et al. 2000] Schwarz AJ, Leach MO: Implications of respiratory motion for the quantification of 2D MR spectroscopic imaging data in the abdomen. Phys Med Biol, 45:2105-2116, 2000.

[Schelbert et al. 2003] Schelbert HR, Beanlands R, Bengel F, Knuuti J, DiCarli M, Machac J, Patterson R: PET myocardial perfusion and glucose metabolism imaging: Part 2-Guidelines for interpretation and reporting. J Nucl Cardiol, 10:557-571, 2003.

[Seppänen e al.. 2006] Seppänen MP, Komar G, Kotoneva E, Teräs M, Minn H: Comparison of 2D and 3D VUE Point reconstruction of PET images with different acquisition times in oncological patients [abstract]. Eur J Nucl Med Mol Imaging, 33 Suppl 2:137, 2006.

[Shannon 1949] Shannon CE: Communication in the presence of noise, Proc. Institute of Radio Engineers, 37:10-21, 1949. Reprint as classic paper in: Proc. IEEE, Vol. 86, No. 2, (Feb 1998).

[Sipilä et al.2007] Sipilä HT, Teräs M, Kokki T, Knuuti J: A moving heart phantom for dual gated cardiac PET/CT studies. in IEEE Nuclear Science Symposium Conference Record. Honolulu, Hawaii, 2007.

[Slifstein et al.2001] Slifstein M, Mawlawi O, Laruelle M: Partial volume effect correction: methodological considerations. In: Gjedde A, Hansen SB, Knudsen GM, Paulson OB, editors, Physiological Imaging of the Brain with PET, Academic Press: San Diego, CA; p. 65-71, 2001.

[Slomka et al. 2004] Slomka PJ, Nishina H, Berman DS, Kang X, Akincioglu C, Friedman JD, Hayes SW, Aladl UE, Germano G: "Motion-frozen" display and quantification of myocardial perfusion. J Nucl Med, 45:1128-1134, 2004.

[Soret et al.] Soret M, Bacharach SL, Buvat I: Partial-Volume effect in PET tumor imaging. J Nucl Med, 48:932-945, 2007.

[SPM2] http://www.fil.ion.ucl.ac.uk/spm/software/spm2/ (29.5.2008).

[Standards publ. 1980] Standards Publ. N0. NU1-1980. Performance measurements of scintillation cameras. Washington, DC, 1980.

[Strother et al. 1990] Strother SC, Casey ME and Hoffman EJ: Measuring PET scanner sensitivity: relating count-rates to image signal-to-noise ratios using noise equivalent counts. IEEE Trans Nucl Sci, NS-37: 783-788, 1990.

[Surti et al. 2007] Surti S, Kuhn A, Werner ME, Perkins AE, Kolthammer J, Karp JS: Performance of Philips Gemini TF PET/CT scanner with special consideration for its Time-of-Flight imaging capabilities. J Nucl Med, 48:471-480, 2007.

[Ter-Pogossian et al. 1982]. Ter-Pogossian MM, Bergmann SR, Sobel BE: Influence of cardiac and respiratory motion on tomographic reconstructions of the heart: implications for quantitative nuclear cardiology. J Comput Assist Tomogr, 6:1148-1155, 1982.

[Tohka et al. 2008] Tohka J, Reilhac A: Deconvolution-based partial volume correction in Raclopride-PET and Monte Carlo comparison to MR-based method. Neuroimage, 39:1570-1584, 2008.

[Townsend et al. 1998] Townsend DW, Isoardi RA and Bendriem B: in book The theory and practise of 3D PET. Edited by Bendriem B and Townsend DW, Kluwer Academic Press, Dordrecht, The Netherlands, 1998.

[Visvikis et al. 2006] Visvikis D, Lamare F, Bruyant P, Boussion N, Cheze Le Rest C: Respiratory motion in positron emission tomography or oncology applications: Problems and solutions. Nucl Instr Meth in Phys Research, Elsevier B.V. A 569 453-457, 2006.

[Wagner et al. 1998] Wagner Jr HN: A brief history of Positron Emission Tomography (PET). Seminars in Nuclear Medicine, XXVIII:213-220, 1998.

[Wang et al. 1995] Wang Y, Riederer SJ, and Ehman RL: Respiratory motion of the heart: kinematics and implications for the spatial resolution in coronary imaging. Magn Reson Med, 33:713-719, 1995.

[Wang et al. 1999] Wang Y, Vidan E, Bergman GW: Cardiac motion of coronary arteries: variability in the rest period and implications for coronary MR angiography. Radiology, 213:751-758, 1999.

[Wang et al 2007] Wang J, Byrne J, Franquiz J, McGoron A: Evaluation of amplitude-based sorting algorithm to reduce lung tumor blurring in PET images using 4D NCAT phantom. Comp Meth and Progr in Biomedicine, 87:112-122, 2007.

[Yang et al 2005] Yang Y, Rendig S, Siegel S, Newport DF, Cherry SR: Cardiac PET imaging in mice with simultaneous cardiac respiratory gating. Phys Med Biol, 50:2979-2989, 2005.

[Zaidi et al. 2004] Zaidi H and Sossi V: Correction for image degrading factors is essential for accurate quantification of brain function using PET. Med Phys, 31:423–426, 2004.